9-7-2017

# Protein-based Autofluorescent Hydrogel and Nano/Micro-Particles for Bio-imaging Applications

Xiaoyu Ma
*University of Connecticut - Storrs*, xiaoyu.ma@uconn.edu

# Protein-based Autofluorescent Hydrogel and Nano/Micro-Particles for Bio-imaging Applications

Xiaoyu Ma, PhD

University of Connecticut, 2017

Fluorescent polymeric materials such as hydrogels and polymeric particles have been attracting attention in many biomedical applications including bio-imaging, optical sensing, tissue engineering and therapy, due to their good biocompatibility, biodegradability, and advanced optical property. This PhD project aims at developing novel autofluorescent protein materials in different configurations with good biocompatibility and biodegradability for bio-imaging applications.

Early research focused on the development of autofluorescent protein hydrogels for *in vivo* bio-imaging application. Glutaraldehyde cross-linked Bovine Serum Albumin (BSA) hydrogel were facilely prepared. Various advanced techniques were employed to characterize the as-prepared material. SEM study clearly revealed its 3-dimentional pore structure, while UV-vis spectra studies, in conjunction with the fluorescence spectra studies including emission, excitation and synchronous scans, indicated that three classes of fluorescent compounds are presumably formed during the gelation process. The autofluorescent hydrogel exhibited high toughness according to the compression and tensile tests. Finally its biocompatibility and biodegradability were demonstrated through extensive *in vitro* and *in vivo* studies. More interestingly, the *in vivo* degradation of autofluorescent hydrogel can be non-invasively tracked using fluorescence images, which provided a convenient way to model *in vivo* biodegradation of the protein hydrogel from a new perspective. The degradation/diffusion trends predicted by the proposed mathematical model were in good agreement with the time-dependent fluorescence images of mice.

Based on the aforementioned autofluorescent concept for BSA system, BSA autofluorescent nanoparticles dispersion and spray-dried microspheres were further fabricated, respectively. Their physical, optical, and biocompatible properties were extensively characterized and evaluated using SEM, FTIR, UV-vis spectra, fluorescence spectra, *in vitro* cytotoxicity assay, *in vivo* histological study, and/or Dynamic Light Scattering. The as-synthesized green and red fluorescent nanoparticles dispersion and microspheres were both applied for cell imaging, ascribing to their unique size properties. Also, *in vivo* degradation processes of these nanoparticles and microspheres in mouse model were also tracked via non-invasive fluorescence imaging and concurrently interpreted by the proposed mathematical model.

To further study the degradation mechanism, *in vitro* degradation of the microspheres by proteinase K were recorded and tracked via Confocal Laser Scanning Microscopy (CLSM), which exhibited two degradation trends based on different concentrations of active enzyme. Microspheres exhibited the swelling of the micro-spherical matrix, accompanying with the decrease of the fluorescent intensity. This phenomena was ascribed to the relatively higher diffusing rate of the enzyme into microspheres matrix than that of the accompanying enzyme-based matrix degradation. A mathematical model was proposed to demonstrate the complexing of microsphere swelling, enzyme diffusion, and diffusion of the liberated fluorophores from enzyme-degraded BSA microspheres matrixes.

As another application of the developed autofluorescent protein materials, the as-synthesized autofluorescent BSA nanoparticles have been applied for sensitive heme/hemin detection, and the ultrasensitive sensing performance is ascribed to Photo-induced Electron Transfer (PET) as well as specific interaction between hemin and the fluorescent protein nanoparticles.

Overall, this dissertation expands the cutting edge in the design and synthesis of autofluorescent materials with good biocompatibility and biodegradability for various biomedical applications.

# Protein-based Autofluorescent Hydrogel and Nano/Micro-Particles for Bio-imaging Applications

Xiaoyu Ma

B.S. Northwest A&F University, **2012**

A Dissertation

Submitted in Partial Fulfillment of the

Requirements for the Degree of

Doctor of Philosophy

at the

University of Connecticut

2017

APPROVAL PAGE

Doctor of Philosophy Dissertation

Protein-based Autofluorescent Hydrogel and Nano/Micro-Particles for Bio-imaging Applications

Presented by

Xiaoyu Ma

Major Advisor_____
Dr. Yu Lei

Associate Advisor_____
Dr. Christian Brückner

Associate Advisor_____
Dr. Mu-Ping Nieh

Associate Advisor_____
Dr. Xiuling Lu

Associate Advisor_____
Dr. Tai-Hsi Fan

Associate Advisor_____
Dr. Guoan Zheng

University of Connecticut
2017

# Acknowledgements

First of all, I would like to express my sincere gratitude to my major advisor Prof. Yu Lei for his guidance throughout my graduate study. This work is impossible without his encouragement and support. Also, I wish to thank my advisory committee (Pro. Christian Bruckner, Pro. Mu-Ping Nieh, Pro. Xiuling Lu, Pro. Tai-Hsi Fan, and Pro. Guoan Zheng) for their valuable guidance, support, and feedback during my Ph.D. research.

In addition, for the excellent group and cross-departmental collaboration, I acknowledge my labmates, visiting scholars and students in collaboration labs such as Xiangcheng Sun, Jun Chen, Qiuchen Dong, Donghui Song, Jing Bao, Swayandipta Dey, Derek Hargrove, and Jiqin Li, etc..

Most of all, I would like to express my love to my parents, boyfriend and family for their support and care.

# Table of Contents

# Chapter 1

# Introduction

## *1.1 Background of fluorescent natural polymer or natural-synthetic hybrid polymer based hydrogels and particles for bio-imaging.*

Polymeric materials in different formats (e.g., hydrogels, micro- and nanoparticles) have been extensively investigated for various applications. For example, hydrogel networks, imbibing a large amount of water and maintaining three dimensional structures,[1, 2] have been widely investigated for biomedical applications ranging from tissue engineering and cell therapies to drug delivery.[2-4] A number of materials, including natural[5, 6] and synthetic polymers, have been utilized as the building blocks for hydrogel synthesis via chemical cross-linking (e.g., photopolymerization, chemical ligation, Michael addition, etc.) or physical cross-linking (e.g., hydrogen bonding, electrostatic interactions, π-π stacking, van der Waals interactions, etc.).[7] On the other hand, polymeric nano- and microspheres with unique size-dependent properties have also been proposed as a unique class of materials to be applied in a variety of divisions related to medical domains as the therapeutic agents can be easily entrapped in the nano- and microparticles and then delivered to the targeted sites.[8-11] Similar as hydrogel, those particles can also be fabricated through chemical or physical cross-linking via various manufacturing techniques, including spray-drying, [12] desolvation[13] and emulsification, [14].

In order to probe various fundamental processes related to life sciences (e.g., *in vitro* or *in vivo* reactions), it typically requires direct tools with high sensitivity and accuracy to non-invasively monitor or image. Fluorescence imaging techniques has been explored as one of the most suitable and popular methods for these purposes. [15, 16] Compared with other non-invasive

imaging techniques (such as Magnetic resonance imaging (MRI), Computed tomography (CT), Single-photon emission computed tomography (SPECT), and Position emission tomography (PET), fluorescence imaging is the most promising imaging modality, because of its high sensitivity, imaging speed, easy operation and relatively low cost. Consequently, a significant amount of efforts have been dedicated to the development of biocompatible polymeric materials with integrated fluorescent property along this research direction, not only because they are benign to tissues and able to greatly suppress the foreign body reaction, but also because fluorescent biocompatible polymeric materials can be non-invasively tracked through fluorescence imaging. To accomplish this goal, a variety of polymers and fluorophores have been entangled together through materials synthesis, rendering the diversity of the fluorescence-based polymeric materials for bio-imaging, tissue-engineering, and biosensors, etc..[17-19] Recently Liu et al. summarized the fabrication methods of fluorescent nanogels through the perspectives of chemical synthesis, *in situ* polymerization, core shell encapsulating, and self-assembling.[20] In order to improve the optical properties of fluorescent polymeric materials in bioimaging application, different types of fluorophores are either covalently or physically incorporated into polymer blocks. Meanwhile, many natural polymers have been widely employed as the building blocks in the synthesis of fluorescent polymeric materials, which possess inherent biocompatibility, biodegradability and significant cell or tissue affinity. In the past decade, we have witnessed that the integration of unique fluorescent property into polymeric materials for bioimaging application has been developing into an emerging research topic. In the introduction chapter of this thesis, I will start with brief presentation of the synthesis of fluorescent hydrogels and particles based on natural polymers or natural-synthetic hybrid

polymers as the building blocks, and followed with fluorescent hydrogels and particles in bio-imaging related applications.

## *1.2 Synthesis of natural polymer or natural-synthetic hybrid polymer based fluorescent hydrogels and particles*

### 1.2.1 Polysaccharides based fluorescent polymeric materials

Polysaccharides are well known hydrophilic polymers and thus appropriate for the construction of the fluorescent polymeric materials. The mostly utilized polysaccharides include alginate,[21] chitosan,[10] hyaluronic acid,[22] and dextran,[23] cellulose,[24] etc.. Through covalent or physical cross-linking, these polymer blocks either form 3D networks or serve as capping agents to enhance biocompatibility for biomedical applications. Polymer chains of the polysaccharides either consist of or are easily modified with diverse functional groups, such as carboxyl, amine, or hydroxyl groups, etc.. Thus, traditional covalent bonds can be formed to result in 3D polymer networks or polysaccharides-capping nanocomposites. Moreover, functionalized groups within polysaccharides chains could also induce electrostatic charges in certain pH circumstances, leading to self-assembled 3D polymer networks or polymer blocks capping nanocomposites through electrostatic interaction. Synthetic methods of a variety of polysaccharides based fluorescent polymeric materials are summarized below.

***Alginate-based fluorescent polymeric materials***

Alginate is a single chain polysaccharide comprising of various compositions, including1,4'-linked β-D-mannuronic acid (M) and α-L-guluornic acid (G) groups. Polymers with high contents of G moieties can bind with divalent cations through electrostatic interactions. Taking advantage of this principle, $Ca^{2+}$ is employed to cross-link with alginate and form hydrogels or microbeads by different researchers, and this moderate synthesis method allows frequent use of

fluorescent alginate bulk hydrogels or particles in a series of bio-imaging related applications. [21, 25] Dong. et al. reported that Polyethylene glycol (PEG) served as covalent cross-linker to anchor protoporphyrin on alginate-PEG copolymer. Following polymerization triggered by calcium ion, fluorescence alginate hybrid hydrogel was formed. [21] Besides bulk hydrogels, alginate-based fluorescent polymeric particles have also been extensively developed using water/oil emulsion systems. Cheng's group [26] prepared fluorescent alginate-chitosan microspheres with encapsulation of glucose oxidase and fluorescent staining of fluorescein isothiocyanate (FITC). In addition, solvent evaporation can help the formation of alginate based microspheres, as a reported hybrid drug delivery system composed of rifampicin-poly (lactic-co-glycolic acid) (PLGA) microspheres and $Ca^{2+}$ *in situ* polymerized alginate hydrogel.[27] Alginate-based fluorescent polymeric materials including hydrogels or particles always possess good biocompatibility and biodegradability, thus they are able to be utilized in a range of bio-imaging related applications which rely on their different size modalities.

***Chitosan-based fluorescent polymeric materials***

Chitosan with pKa around 6.2 is a copolymer composed of glucosamine and N-acetylglucosamine. It is positively charged in low pH solutions, while insoluble and uncharged at high pH or neutral conditions. Thus chitosan has been extensively applied in pH-related biomedical applications, such as pH-controlled drug release and delivery matrix [28] and mucoadhesive polymeric systems.[29] Furthermore, chitosan can enhance the permeability through unfolding epithelial tight junctions.[30, 31]

Chitosan based fluorescence hydrogels or particles are able to be cross-linked by traditional linker glutaraldehyde via Schiff base, due to the abundant amine groups in the polymer chains of chitosan. For example, Cabral et al. reported the formation of dextran-chitosan fluorescence

hydrogel via glutaraldehyde cross-linking. [23] Besides bulk hydrogel, chitosan based nanoparticles can be obtained via covalent conjugation. Recently Lin's group developed fluorescent PEG-chitosan-iron nanocomposite targeting on specific tumor cells via nonsolvent-aided coacervation procedure prior to covalent cross-linking.[32] Moreover, water/oil emulsion, as a widely employed technique for the synthesis of nano- and microparticles, was applied in the fabrication of covalently cross-linked particles. For example, Wei's group applied glutaraldehyde for covalent cross-link in membrane emulsification to form homogeneous autofluorescent chitosan microspheres. [10]

Besides covalent interactions, physical cross-linking was also widely employed for the development of chitosan-based polymeric materials. Ionic interactions, as the strongest physical force, were reported to drive the formation of chitosan-based material system in a study reported by Jheng et al. who presented the development of fluorescence nanoparticles via electrostatic interactions between polymer chitosan-*N*-arginine and near-infrared cyanine dye.[33] In another study, Sachdev et al. applied glycerol as ionic cross-linker for the formation of chitosan hydrogel particles, and chitosan- Polyethylenimine (PEI) carbon dots were integrated into the particles via non-covalent interaction to provide green fluorescence property.[34] Water/oil emulsion technique was also applied to the synthesis of particles based on physically cross-linked chitosan. As an example, Bazylinska's group entrapped DNA in the newly developed nanocapsules which were obtained by layer-by-layer adsorption of DNA and oppositely charged chitosan on the nanoemulsion core, while fluorophore IR-780 was loaded in the center and stabilized by the surfactant of gemini-type ammonium salt.[35] Taking advantage of forming chitosan-based polymeric materials through hydrogen bonding, Wang et al. fabricated PEG-chitosan carbon dots hybrid fluorescent nanogels by physically entangling PEG with chitosan chain via hydrogen

bonds first, followed by the polymerization of PEG non-linear macromonomers. At the same time, carbon dots, not only serving as optical contrast and enhancing the loading capacity of hydrophobic drug, but were also *in situ* physically immobilized in the polymerized gel through hydrogen bonding, resulting in better composite stability.[28]

Moreover, due to chitosan accessibility to chemical and physical cross-linking, some chitosan-based systems were fabricated using both covalent and ionic cross-linking in two-step double emulsions.[36] As a demonstration, Andrei et al. developed fluorescent chitosan-gelatin hybrid particles through a two-step cross-linking process with fluorophores covalently embedded in the particles via a condensation reaction between amine groups of chitosan and carboxyl groups of fluorescein.[37]

Furthermore, chitosan can also been utilized as biocompatible polymeric capping agents for the formation of metal nanoparticles.[38-40] Cheng et al. reported chitosan-assisted fabrication of multifunctional magnetic fluorescent nanocomposites through coating chitosan on $Fe_3O_4$-$SiO_2$ surface using glutaraldehyde as the cross-linker, followed by ester condensation reaction via 1-Ethyl-3-(3-dimethylaminopropyl)carbodiimide (EDC) and *N*-hydroxysuccinimide (NHS) to modify the surface with pyropheophorbide-a (PPA, serving as optical signal contrast).[41] Jalani's group also synthesized NIR to UV-vis-NIR upconverting nanoparticles coated with chitosan hydrogel layer, where at the same time fluorescent bovine serum albumin (FITC-BSA) were encapsulated in the gel layer to endow the fluorescent property to the nanocomposite.[38]

***Dextran based fluorescent polymeric materials***

Dextran is a hydrophilic polysaccharide, specifically composed of a large number of hydroxyl groups, by which many dextran derivatives have been developed for synthesis of hydrogels or particles.

Some dextran derivatives can covalently bind with synthetic polymers to form hybrid fluorescent hydrogels or particles. Several examples are presented as follows. Toman's group demonstrated the fabrication of fluorescent alkylglyceryl-dextran-grafted poly (lactic acid) nanoparticles, where the dextran was firstly treated with epoxide precursors of alkylglycerol, followed by the covalent conjugation onto poly (lactic acid), and at the same time Rhodamine B as the fluorescent marker was loaded.[42] Artzi et al. developed fluorescein labelled PEG-dextran (aldehyde functionalized) hybrid hydrogel via Schiff base reaction.[17] Besides covalent cross-linking, physical cross-linkers are also able to induce the synthesis of dextran based fluorescence polymeric materials. Recently Dai et al. reported a simple self-assembled dextran-based nanogels driven by hydrogen bond interactions between the hydroxyl groups of dextran and the carboxyl groups of poly (acrylic acid) chains, and the abundant carboxyl groups also allowed the reaction with amine groups for fluorescence modification.[43] Some dextran based fluorescent particles were also prepared via cross-linking in conjunction with water/oil emulsion procedure.[44]

***Hyaluronic acid based fluorescent polymeric materials***

Hyaluronic acid (HA), a linear polysaccharide with carboxyl functional groups and high molecular weight, is negatively charged at physiological pH. It can serve as the component of extracellular matrix and act on cell-cell interactions, cell-matrix adhesion and cell activations in human body.[45] Therefore, it is suitable for tissue-engineering applications because of its good physical properties and biocompatibility.[22]

Most researches rely on chemical cross-linking to synthesize HA-based polymeric materials. Due to the presence of carboxyl groups, hyaluronic acid can be functionalized on the surface of nanoparticles possessing primary amine groups via EDC/NHS conjugation chemistry, resulting in good biocompatibility.[40] Carboxyl groups within hyaluronic acid chains not only allow

direct chemical cross-linking, but also render the accessibility to graft other functional groups (e.g., thiol, aldehyde, maleimide, etc.) on hyaluronic acid. Thus, different types of fluorophores and other types of polymers integrated into HA-based fluorescent polymeric materials can be realized through diverse chemical cross-linking methods. Zhang et al. [22] reported a fluorescent HA-based hydrogel, in which HA was first functionalized by carbodiimide, followed by the fluorophores coupling via Michael addition reaction. The resulted fluorescent hydrogel was finally obtained via disulfide reaction. Besides bulk hydrogel, Wade et al. applied electrospinning to prepare fluorescent protease-degradable hyaluronic acid fibrous hydrogel thin films. As hyaluronic acid was modified with maleimide groups, thus enabling covalent bond with both thiolated fluorophores and degradable methacrylate peptide. Photo-polymerization of methacrylate resulted in hydrogel structure.[46] Ossipov's group also reported aldehyde and thiol functionalized hyaluronic acid for the synthesis of fluorescent networking/nanostructure for drug delivery, where those functionalization allowed the bioconjugation via thiol-disulfide exchange cross-linking, carbazone-linked poly (vinyl alcohol) prodrug of doxorubicin, and the attachment of hydrophobic optical contrast (pyrene) simultaneously.[47] In addition, according to the approach from Zhang's group, HA was converted to tetrabutylammonium salt (HA-TBA), allowing the formation of Cy5.5 conjugated hyaluronic acid nanoparticles with strong fluorescence.[48] Furthermore, the anionic property of hyaluronic acid could also be employed to complex with cationic polymers and form fluorescent polymeric materials if fluorophores were incorporated during the complexation.[49] Hyaluronic acid based fluorescent polymeric materials were mainly used in the modality of hydrogel for non-invasive degradation tracking or tissue engineering, ascribing to their good biocompatibility and biodegradability.

### 1.2.2 Protein Based Fluorescent Polymer Blocks

A variety of proteins, including collagen, gelatin and albumin, etc. possess interesting properties which favor their applications in the synthesis of biocompatible and biodegradable fluorescent polymeric material. Due to the presence of diverse functional groups in the protein molecules, chemical cross-linkers such as glutaraldehyde and EDC/NHS have been widely used to fabricate 3D protein networks. Moreover, physical cross-linking is another important method to prepare 3D protein networks through physical interaction of the various functional groups within protein/peptide chains. Synthesis of protein based hydrogel has progressed significantly in recent years, because of their great potential in various biomedical applications. Collagen and gelatin have been widely used in preparing hydrogels which are applied in tissue engineering and cell growth matrix, since they display many advantageous properties such as high tensile strength and good cellular interactions.[50, 51] Recombinant gelatins are able to be produced using genetically engineered yeast cells, thus resulting in precisely tailored polymer properties (e.g., molecular weights and isoelectric points). Hence, recombinant gelatins can be pre-designed according to the requirements for different applications, such as degradation times, swelling properties, etc..[7] Besides collagen and gelatin, low-cost bovine and human serum albumin (B/HSA) possesses high solubility in aqueous solution as well as good biocompatibility, thus rendering their extensive utilization in the fabrication of fluorescent hydrogels/particles for bio-imaging related applications.[52, 53] Similar to polysaccharides, proteins have also been extensively used as capping agents to enhance the biocompatibility of the nano- and microparticles for medical applications. Besides proteins, polypeptides or specific amino acids have also been utilized as the building blocks to construct biocompatible fluorescent polymeric materials.[54, 55]

***Covalently cross-linking to form protein based fluorescent polymeric materials***

Common cross-linkers such as glutaraldehyde, genipin, carbodiimide, etc., have been widely used in the fabrication of protein-based fluorescent polymer hydrogels/particles in the past decades. More recently, a few new approaches have been developed to harness the novel autofluorescence of proteins which was induced during the formation of hydrogels via cross-linking of amine groups within protein molecules. These autofluorescent polymeric materials possess more advantages compared with traditional fluorophores embedded hydrogel systems, as they can avoid leaking issue and minimize the cytotoxicity due to the use of fluorophores. Recently Hwang et al. reported the genipin cross-linked collagen forming autofluorecent hydrogels which was characterized in terms of one-photon fluorescence spectroscopy, second harmonic generation measurement, fluorescence and transmission electron microscopy.[50] They found that the as-synthesized hydrogel possessed autofluorescence with the emission maximum at 630 nm when excited at 590 nm. However, when they used 400 nm excitation light, an emission peak was observed at 462 nm. However, more fundamental investigation of photophysical properties is required, such as fluorescence emission/excitation scan, UV-vis spectra, in order to obtain a full vision of the concept for induced autofluorescence. Besides genipin, aldehyde also reacted with amino groups within proteins to obtain autofluorescent polymeric materials. Lyubovitsky's group prepared glyceraldehyde modified gelatin hydrogels which exhibited strong fluorescence with emission peak at 454 nm when excited at around 350 nm. They proposed that the autofluorescence originated from the formation of non-enzymatic glycation end-products during the cross-linking process.[51] Recently our group also applied glutaraldehyde as the cross-linker to form autofluorescent BSA hydrogels, which displayed unique green and red fluorescence under the appropriate excitation wavelengths.[52] Wang et al. also synthesized sericin hydrogel by glutaraldehyde cross-linking.[56] Similarly, the hydrogel

possessed blue, green and red photoluminescence. Furthermore, Yang's group introduced a method for the synthesis of fluorescent carbon dots using denatured BSA which can be treated as polypeptide. The denatured BSA was cross-linked using glutaraldehyde and then autoclaved with different time, thus resulting in the fluorescent BSA carbon dots.[57] As a comparison, when carbodiimide was employed as the cross-linker for the generation of the polymeric materials, there was no induced autofluorescence observed. Hence, these results might suggest that autofluorescence was mainly attributed to the n-π* transition of the newly formed C=N bond after cross-linking reactions. In addition, the bonds involving in the conjugation reaction also play an important role in generating autofluorescence, as only when the bonds of C=C, C=C and C=O are conjugated, their UV-vis absorption peaks would shift relevantly to a higher wavelength region, partially elucidating the origin of autofluorescence. Moreover, proteins possess primary, secondary and tertiary structures, which may also have significant influence on the synthesis of the fluorescent compounds. The fluorescence observed might be attributed to the synergistic effect of several amino acids in close proximity in cross-linked proteins, for example, similar to other green or red fluorescent proteins. Moreover, the charge surrounding the flurophores in cross-linked proteins is another potential factor to affect the fluorescence. More efforts are required in order to identify the chemical structure of such stable autofluorescent compounds.

Besides bulk hydrogels, traditional chemical cross-linkers have also been extensively employed for synthesis of protein-based fluorescent particles. Kumar's group cross-linked BSA and some protein-based enzymes using EDC and immobilized fluorescein in the protein nanoparticles at the same time, resulting in fluorescent nanoparticles.[53] Qin's group reported the synthesis of fluorescent BSA nanoparticles through application of desolvation technique to incorporate far-red fluorophores, followed by glutaraldehyde cross-linking.[16]

Moreover, hybrid protein-synthetic polymers have also attracted much attention for the synthesis of fluorescent hydrogels or particles, because covalent conjugation endows many advantages as the synthetic polymer can be functionalized with a series of chemical groups. Berdichevski et al. developed PEG-diacrylate (PEGDA) conjugated with denatured fibrinogen through Michael addition reaction, accompanying with covalent incorporation of fluorophore Cy 5.5 into fibrinogen peptide chains. The fluorescent hydrogel was finally generated via photopolymerization through diacrylate.[18] In addition, as protein is covalently conjugated with hydrophobic polymers, "surfactant" like structure could be obtained, thus allowing self-assembling with hydrophobic molecules (e.g., fluorophores) to form fluorescent "star" particles. Along this direction, Liu et al. reported the covalent conjugation between hydrophilic BSA and hydrophobic synthetic polymer Polycaprolactone (PCL) through maleimide-sulfhydryl reaction, in which fluorescent quantum dots were self-assembled in the hydrophobic cores.[58] Moreover, protein hybrid fluorescent nanoparticles can be prepared via the integration of water-in-oil emulsion and chemical cross-linking. Yoon's group developed human serum albumin (HSA)-PAA particles by conjugating HSA with amine functionalized monomer, followed by polymerization in emulsion and surface modification using F3-Cys peptide. An optical contrast (indocyanine green, ICG) were further incorporated through post-loading to endow the fluorescence to the HAS-PAA particles.[59]

***Physical cross-linking to form protein based fluorescent polymeric materials***

Proteins or polypeptides comprise a variety of functional groups, allowing the physical cross-linking through hydrogen bond, electric interactions, and/or π- π stacking, etc.. In addition, they also hold a variety of conformations, including α-helix, β-sheet and random coil, which lend themselves as building blocks or cross-linking units in the preparation of fluorescent

hydrogels/particles.[7] Recently Wang's group introduced Rhodamine B as a new capping group of self-assembling peptide, which not only provided the driving force for the formation of supramolecular nanofibrous hydrogel via hydrophobic and π-π stacking interactions, but also endowed the hydrogel with intrinsic fluorescence signal.[55] In addition, some specific amino acids can also be utilized for construction of fluorescent polymeric materials, ascribing to their functional groups and their unique conformations when they were conjugated together. As a pioneering research, Cui et al. reported a cysteine-Ag cluster hydrogel with intrinsic fluorescence as $Ag_3$ isomers formed during the polymerization process.[54] To form this unique cysteine-Ag cluster hydrogel, Ag-S bonds first enabled the formation of Cys-Ag3-Cys monomer, and then the self-assembling occurred due to the intermolecular hydrogen bond between carboxyl groups of adjacent monomers, which resulted in multimer with left-handed helix conformation, favored by a thermodynamic process. The hydrogel was finally generated as these "multimers" entangling with each other.

Electrostatic interactions, as the strongest physical cross-linking forces, are also widely applied in the preparation of layer-by-layer protein-based particles or protein-capped metal particles. Kalaska's group employed a layer-by-layer self-assembly method to synthesize protein-based microspheres using collagen and fibronectin.[60] Fabrication of these micro-particles involved the use of carboxyl-functionalized polystyrene particles as the template core, followed by coating of two layers of different polyelectrolytes through electrostatic interactions, where each layer was labeled with distinct fluorescent dye. Moreover, researchers employed protein as the capping agent of the nanocluster, such as quantum dots [61], silver, [62] gold [63] and copper[64] etc., resulting in improved biocompatibility, better solubility in aqueous solution and good cell internalization ability (due to the receptor-mediated cell uptake). In addition, Niu et al. reported a

proof-of-concept of up-conversion fluorescence-SERS dual tags nanoparticles with BSA capping, which aimed at rendering both biocompatibility and stability. The as-synthesized nanoparticles possessed with dual NIR fluorescence imaging and plasmonic SERS capabilities, allowing their use in cell and *in vivo* imaging. [65]

## *1.3 Fluorescent Natural Polymer Hydrogels/Particles for Bio-imaging*

In recent years, fluorescent nano/micro particles and bulk hydrogels have been extensively utilized in the area of molecular imaging, especially in living cells, tissues, and animal models, due to their unique size-dependent and photoluminescence properties serving as straightforward tracking signals. However, utilization of fluorescent particles/hydrogels for *in vivo* model either through subcutaneous or intravenous injection needs to address the challenge associated with light absorption of tissue and specific molecules in order to realize non-invasive imaging. As a result, fluorescence emission in the near infrared region is typically desirable. Regarding to cell imaging applications, it is more flexible with respect to the emission wavelength range of the fluorescent materials, as a shorter wavelength can be endurable and thus applicable to acquire the fluorescence images. Therefore, *in vivo* or cell fluorescence based imaging technique has been widely applied in monitoring or tracking the temporal or spatial phenomena in different scenarios.

### 1.3.1 *In vivo* bio-imaging

As for the *in vivo* fluorescence-based imaging, some pioneering studies demonstrated that the fluorescence can penetrate tissues to certain degree and thus is able to be used as an optical signal in imaging-based tracking or monitoring. Recently Wang et al. visualized glutaraldehyde cross-linked sericin hydrogel with red autofluorescence *in vivo*, paving the road for potential bio-imaging applications.[56] Moreover, fluorescent polymeric materials, with a shorter wavelength

emission but strong afterglow, have also be applied for *in vivo* imaging. For example, Wang et al. used cellulose-phosphor hybrid hydrogels with strong green fluorescence for *in vivo* imaging as the prepared fluorescent hydrogel was able to be captured both under the skin and in the stomach with or without excitation light, ascribing to their strong afterglow properties. [24] Recently, other imaging modalities (e.g., CT[66] or MRI [44]) were always used with fluorescence imaging together to improve *in vivo* imaging quality and enrich the information output. As an example, Niu et al. demonstrated a proof-of-concept dual-imaging method in which the BSA-coated nanoparticles were doped with fluorophores and Raman contrast agent simultaneously, and thus the fluorescence and Raman signals were able to be simultaneously monitored after the nanoparticles were subcutaneously injected into the rat.[65] Besides aforementioned general application, several specific applications of *in vivo* bio-imaging have also been reported, including specific tissue *in vivo* mapping, selectively tumor targeting, and tracking the *in vivo* degradation of the injected or implanted fluorescent materials, which will be discussed in details in the subsequent sections.

***Fluorescent polymeric materials for specific tissue mapping***

Nano/micro biocompatible particles possess unique size-dependent properties, thus it can be taken up by the cells through phagocytosis, providing an access to mapping of specific tissues. Recently, Dai et al. reported that the as-synthesized fluorescent dextran-based hybrid nanogels (FDNG) or nanoparticles could serve as the nanoprobes for the sentinel lymph node (SLN) mapping. In this study, BALB/c mouse model was applied for an *in vivo* test to demonstrate the mapping function of the fluorescent nanoprobes. Although the fluorescence imaging suggested the biocompatibility of FDNG with the functionality of SLN mapping, no mechanism was provided for the observed specific internalization of the as-prepared FDNG by SLN cells. [43]

Generally speaking, to achieve the goal of specific targeting and imaging, functionalization of the fluorescent polymeric materials with specific biological ligands is a widely adapted strategy. Bonnard et al. developed dextran-based injectable microparticles for targeting endothelial tissues. The microparticles consisting of both MRI contrast agent and fluorescence label were functionalized with fucoidan in order to mimic the anchor sites of *p*-selectin glycoprotein ligand-s (PSGL-1), one of the principal receptors supporting leukocyte adhesion. [44] The fluorescence imaging results indicated that the targeted microspheres exhibited both strong *in vitro* affinity with human activated platelets and the capacity to bind activated endothelial cells according to the *in vivo* study.[44]

***Fluorescent polymeric materials for tumor targeting***

Another attractive bio-imaging application using fluorescent polymeric materials is specific tumor-targeting, which could be used in cancer diagnosis. In order to accumulate the fluorescent polymeric materials within cancer tissues, a number of studies harnessed the enhanced permeability and retention (EPR) effect of the fluorescent polymeric nanoparticles by virtue of their small sizes. Qin et al. recently synthesized far-red/near-infrared fluorogen doped fluorescent BSA nanoparticles. The as-prepared fluorescent BSA nanoparticles were intravenously injected into the tumor-bearing mouse and an impressive tumor targeting capability was realized and attributed to both EPR effect and the lack of lymphatic drainage of the tumors [16] In addition, Wang et al. reported the use of diluted fluorescent supramolecular nanofibrous hydrogel for *in vivo* tumor targeting, in which the accumulation of the diluted nanofibrous hydrogels on tumor blood vessels were characterized through confocal imaging.[55] Furthermore, various specific ligands have been employed to target certain acceptors overexpressed on cells. Ding's group functionalized fluorescent BSA nanoparticles with

arginine-glycine-aspartic acid (RGD) to yield fluorescent probes for specific recognition of the cancer cells, which was demonstrated and validated via fluorescence imaging on a tumor-bearing mouse model.[67] To target the overexpressed folate receptors on cancer cells, folic acid and methotrexate can be used as selective targeting ligands, while gold nanoclusters are regarded as a class of promising materials for tumor imaging because of their low toxicity, intrinsic fluorescence and good accessibility to multifunctional groups for surface modification with diverse bioactive molecules. Recently Chen and co-workers demonstrated the highly specific targeting of folate receptor expressing tumor based on Au nanoparticles, which were surface-coated with BSA and folic acid. They studied the dynamic distribution of the as-prepared fluorescent nanoparticles in normal nude mice and tumor-bearing mice models according to the real-time fluorescence imaging and ex *in vivo* organs fluorescence images. The results suggested that fluorescent nanoparticles possessed high selectivity for tumor targeting and were mainly accumulated in the organ of liver and kidney for easy clearance from the body. [63] Besides folic acid, methotrexate (MTX) was also applied along this line, which not only served as a promising molecule for specific targeting of folate-overexpressing tumor cells, but also a chemotherapy drug. For example, in a study conducted by Lin et al., MTX modified chitosan nanocomposite showed specific targeting to HeLa cells and decreased their uptake in the liver after the intravenous injection into the mice, compared with the same nanocomposite without MTX functionalization.[32] In addition, glycol chitosan modified nanoparticles also displayed superior tumor-targeting ability.[68]

Bimodal imaging has also been used for monitoring the efficiency of the as-synthesized fluorescent polymeric materials in tumor targeting with both temporal and spatial resolution. In this case, two or more types of optical contrasts are incorporated in the polymeric building

blocks simultaneously, thus rendering the accessibility to different imaging modalities. As a demonstration, Sun et al.[66] reported an interesting tumor-targeting AuNP nanoprobe for dual CT/fluorescence imaging of cancer. In this study, glycol chitosan (GC) polymers modified surface showed excellent stability and tumor targeting ability.[69] Further functionalized of the nanoprobes with matrix metalloproteinase (MMP) active peptide enabled the enhancement of the tumor penetration by peptide degradation.[70] The as-prepared nanoprobes exhibited good tumor-targeting ability, manifesting by both *in vivo* CT and fluorescence imaging. [66] Besides CT/fluorescence, MRI/fluorescence bimodal imaging were also employed to track tumor targeting behavior. [71]

***Fluorescent polymeric materials for in vivo degradation tracking and monitoring of the injected biomaterials***

Biodegradable materials are in the leading edge of biomaterials as they serve as platforms for structural stabilization, void filling, drug delivery and tissue engineering and also reduce potential complications caused by permanent foreign objectives. [72-74] Thus, to track and monitor the degradation of biomaterials is of paramount importance as it provides solid ground to understand the degradation pattern of biomaterials *in vivo* and explore their other potential biomedical applications. Fluorescent hydrogel matrixes in different size configurations are typically employed for biodegradation study due to their size-dependent *in vivo* retention time. In general, two degradation mechanisms occur in *in vivo* condition: hydrolysis and enzymatic degradation. As for the enzymatic degradation, proteins, polysaccharides and hybrid synthetic-natural polymers have been applied as the polymeric materials for fluorescent hydrogel constructions, and *in vivo* degradation of the as-prepared fluorescent materials are tracked via

real-time fluorescence imaging.[18, 22] In other instances, hybrid synthetic-natural polymers are degraded via hydrolysis.[17]

In recent years, *in vivo* degradation studies of the fluorescent materials mostly rely on non-invasive real-time fluorescence imaging. Although more and more studies employ non-invasive fluorescence imaging to illustrate *in vivo* biodegradation properties of the as-synthesized materials, most of them rely on the fluorescence of additional fluorophores integrated in the materials. The rationale is on the basis of the fact that the change or decay of the recorded fluorescence represents the degradation of the injectable or implantable materials. This rationale is correct and reliable when the chemical fluorophores possess relatively high photo-stability, where fluorescence decay induced by photobleaching is negligible when compared with that resulted from the degradation of the materials. However, tissues not only absorb light, but also lead to light scattering. Therefore, subcutaneous injection or implantation of the materials is typically used to minimize light absorption and scattering, thus leading to more accurate results.

Most of the natural polymer based functional materials exhibit enzymatic degradation properties, as they are easily degraded by certain enzymes in human body. However, different cross-linking methods used in the formation of polymeric materials always affect the degradation process, especially in the temporal domain. Therefore, plenty efforts have been spent on the investigation of *in vivo* degradation of the synthesized natural polymer matrixes via non-invasive fluorescence imaging. Zhang et al. used fluorescent hyaluronic hydrogel for *in vivo* and *in vitro* enzymatic degradation study via non-invasive fluorescence imaging. As the similar degradation trend was obtained under both conditions, it suggested that these methods can be used as a predictive *in vitro* tissue engineering model.[22] Furthermore, an alginate hydrogel with covalently incorporated protoporphyrin as fluorophore, which could be enzymatically degraded within 3

weeks, was developed and utilized for the tracking purpose of *in vivo* degradation.[21] Not only do materials and cross-linking methods have an effect on *in vivo* degradation trends, the size configuration of the hydrogel matrix is also a significant factor. Thus, according to different requirements in medical application, *in vivo* degradation studies of hydrogel with different size were also investigated. Wade's group subcutaneously implanted (non) degradable peptide modified fluorescent HA fibrous hydrogel through electrospinning, and *in vivo* degradation of the implanted fluorescent hydrogel were tracked and compared through transdermal fluorescence imaging.[46]

Besides non-invasive fluorescence imaging based *in vivo* degradation studies, bimodal imaging has also attracted increasing attention, as more accurate signal can be acquired. Berdichevski et al. [18] developed PEG-fibrinogen fluorescence hydrogels in three configurations: *in-situ*, microspheres and plug, entangling with MRI contrast Gd and fluorescence label Cy5.5 for bimodal imaging in order to investigate and compare *in vivo* degradation performance of these hydrogels. Interestingly, the degradation trend of these synthesized fluorescent hydrogels was different from other studies, where the fluorescence intensity increased at the beginning and then decayed, indicating the release of the fluorophores along the dissociation of the materials and the resorption of small fluorescent molecules by tissues. This approach provides an elegant analysis for the enzymatic degradation, as well as the release and resorption process of the biodegradable fluorescent hydrogels.

*In vivo* degradation process of fluorescent polymeric materials is a very complicated process compared with its *in vitro* counterpart. Although a number of studies have been conducted to use non-invasive fluorescence imaging for tracking and monitoring *in vivo* degradation in real-time

format, only a very few investigations have proposed mathematical models to understand and depict the degradation process. Recently, there are two reports adapting a similar approach to model the *in vivo* degradation of fluorescent biomaterial and then to compare with the *in vitro* degradation process of the same material, thus providing the foundation for their further utilization in drug release, tissue-engineering and therapies, etc.. In one study, Artzi et al. [17] developed PEG-dextran hybrid fluorescent hydrogels as well as fluorophore labeled collagen sponge for *in vivo* hydrolytic and enzymatic degradation studies via non-invasive fluorescence imaging. The degradation trends were further fitted using a dual exponential decay model. Moreover, they found out the correlation of the hydrogel erosion rate between *in vitro* and *in vivo* degradation process, which could potentially enable the prediction of the *in vivo* erosion performance for the new materials formulations according to the *in vitro* results. In addition, collagen erosion experiment was also utilized to infer *in vivo* physiologic environment that can be mimicked under *in vitro* conditions. This approach can be considered as a promising method for many biomedical applications, including rapid *in vitro* screening of materials suitable for *in vivo* applications, the determination of drug release and material erosion from a drug-eluting scaffold, and material fate in tissue-engineering formulations. However, another study using PEG hydrogel with integrated Rhodamine B fluorophore supported linear *in vivo* decay trend, contradictory with the previous study.[75] In both studies, PEG functionalized with covalently doped fluorophores are utilized to prepare fluorescent hydrogels, and both fluorescence intensity decay and weight loss are combined to monitor the degradation process, yet adverse results are obtained. The disagreement may be attributed to a couple of factors. First, the real-time fluorescence intensity extracted from the real-time fluorescence imaging represented not only the release of the fluorophores induced by the material degradation, but also the photo-bleaching of

the doped fluorophores. Furthermore, simple exponential or linear fitting was applied to model the degradation process in these two studies, which might be too simple to represent the real situation. More accurate and meaningful models with the incorporation of physiological parameters should be developed. In our approach to address this issue, we synthesized autofluorescent BSA hydrogels in three sizes (bulk hydrogel, [52] microspheres[76] and nanoparticles[77]), all of which exhibited green and red fluorescence with excellent photo-stability, for *in vivo* degradation and modeling. The real-time fluorescence intensity data directly reflected the degradation of the hydrogels, which avoided the effect of photo-bleaching and leakage of fluorophores. Moreover, we proposed a delicate quasi-two dimensional diffusion model to interpret the degradation process. The model and the experimental results were in good agreement.

### 1.3.2 Cell imaging

Cell imaging has been a hot research topic in recent years, as it can be used to study the cell internalization capability of the fluorescent polymeric materials. Moreover, selective tumor targeting/imaging is an essential criterion for cancer therapy, thus another important application of *in vitro* cell imaging is to indicate selective targeting/delivery behavior of the synthesized material system. Confocal laser scanning microscopy is often applied for cell imaging study ascribing to the advantages of its z-stacking function, which allows to acquire images at different heights. Even though the requirement for the excitation/emission wavelengths of the fluorophores in cell imaging are not as strict as for *in vivo* imaging application, the as-prepared fluorescent polymeric materials should possess reasonably good photo-stability, as continuous laser scanning can potentially destroy the optical property of the fluorescent materials. Regarding the driving forces for cell internalization, there are two approaches widely used, including

electroporation by which the permeability of cell plasma membrane increases under the high electric field, leading to the penetration of the particles into the cells, [78] and cell endocytosis by either physically bound to or located in the vicinity of the plasma membrane. [79]

***Cell imaging for internalization studies***

Natural polymer based or modified particles are extensively used in the studies of cell imaging, because natural polymer can enhance the aqueous solubility of particles and also allow cell internalization of the particles simultaneously. Although most of the investigations are based on cell endocytosis, detailed mechanisms differ. In a recent study, Deshapriya et al. used fluorescein-labeled multiple protein nanoparticles for cell imaging applications and also proposed the internalization mechanism as follows: the presence of glucose oxidase facilitated the cell uptake, while the hydrogen peroxide acted as permeability enhancement of cell membrane.[53] Qin et al. also synthesized fluorescent BSA nanoparticles doped with relatively photo-stable fluorogen for *in vitro* cellular imaging study, in which BSA molecules were suggested to play an important role in the cell internalization through mediated endocytosis.[16] In addition, Yang's group recently used BSA-based fluorescent carbon dots conjugated with cell penetration peptide for dynamic tracking of its internalization on living cell membrane by taking the advantage of the superior optical stability of the BSA-based carbon dots.[57] Besides fluorescent particles, diluted fluorescent polypeptide-based self-assembled supramolecular hydrogels were also utilized for cellular uptake imaging and the results indicated that the as-prepared nanomaterials can be used for tracking as long as 7 passages.[55] Moreover, protein can be used to functionalize the surface of metal nanoparticles to endow good interactions with cell membrane for cell imaging applications. As a demonstration, Wang et al. reported the development of BSA-functionalized copper nanoparticles for cellular imaging using confocal

microscope.[64] Polysaccharides based or modified fluorescent polymeric materials in appropriate size configurations can also be easily internalized by cells. Wei et al. reported autofluorescent chitosan microspheres for cell imaging, where individual microspheres were optically visible. [10] Xia et al. also introduced a new type of core-shell fluorescent chitosan-based hybrid nanospheres with *in situ* formation of Au nanoparticles in the core for fluorescence intensity enhancement in cell imaging.[80] Moreover, Tzeng et al. compared electroporation and passive cell endocytosis using BSA-modified fluorescent nano-diamonds (FND). The results demonstrated that more BSA-modified FND can be internalized in comparison with rare (FND) taken up by cell via electroporation, corroborating that BSA played an important role in cell internalization of the fluorescent particles.[81]

With the need of enriching information output, dual-mode bio-imaging methods become more and more popular. For example, the aforementioned BSA nanoparticles were labeled with both fluorescent and surface enhanced Raman scattering dual tags for cell imaging, consisting of both fluorescence and Ramen signals. [65] Furthermore, two-photon fluorescence imaging has also been used in some studies to accomplish a similar goal, where fluorescent particles taken up by cells can be studied based on the excitation either at lower excitation wavelengths or longer ones, as illustrated in a study by Wang et al..[28]

Cell imaging can not only indicate the cell internalization of the particles or diluted supramolecular hydrogels, but also track their intracellular distribution. Recently Zhang et al. utilized fluorescent BSA nanoparticles for cellular imaging and also demonstrated their intracellular distribution. The exogenous nanoparticles were initially enclosed in endosomes and then accumulated in lysosomes. [82] In another study, Cui et al. tracked intracellular distribution

of diluted fluorescent cysteine-Ag cluster hydrogel via fluorescent imaging. The results suggested the good biocompatibility and lysosome targeting property of the diluted hydrogel. [54]

***Cell imaging for selective cell targeting studies***

To further achieve high efficiency and selectivity for specific cell imaging, surface modification strategies have been widely utilized to enhance the cell penetration and/or specific targeting. Recently fluorescent BSA nanoparticles with RGD surface modification was reported for highly selective tumor targeting which was validated through cellular imaging.[58, 67] Not only RGD peptides, other target-specific peptide (e.g., F3-Cys) has also been widely used by Yoon and coworkers to functionalize the cell imaging materials and thus achieve specific cell selectivity.[59] Besides target-specific peptides functionalization, folic acid was also selected as a tumor targeting ligand.[61, 63] In addition, hyaluronic acid is a component of extracellular matrices and regulates many biological processes such as the interaction with CD44 receptor, which was validated by cell imaging study from Ossipov's group.[47] Park's group also showed that hyaluronic acid based fluorescent nanoparticles with entrapment of near-infrared dyes exhibited specific CD44 gastric cancer marker targeting capability through the tumor cell imaging.[49]

***Cell imaging for evaluation of delivery and chemotherapy efficiency***

Natural polymer-based fluorescent particles as delivery systems allowing both real-time monitoring and prolonged release hold great promise due to their good biocompatibility, biodegradability and injectability. [83] Currently, growth factors or anticancer drugs are mainly doped in fluorescent protein particles for the purpose of cancer or tissue therapy. To develop a good delivery system, one essential consideration is the efficiency of intracellular membrane

traffic of the delivery system. Thus, cell imaging is an efficient method to monitor whether and how efficiently the drug matrix can be taken up by the cells.

Up to date, a number of research groups developed various fluorescent material systems for the delivery of chemical drugs, especially anti-cancer drugs, which was validated through bio-imaging study. Sachdev et al. doped anti-cancer drug (5-Fluorouracil) in chitosan nanogel embedded with green fluorescent carbon dots, for imaging-guided investigation of cancer cell apoptosis.[34] Also Gui et al. developed chitosan-coated fluorescence quantum dots, which proved to be a promising carrier for Doxorubicin in cancer treatment as the HepG2 cells exhibited bright fluorescence after exposure to such fluorescent nanoparticles.[39]

Besides its application in validating the delivery of the chemical drugs, cell imaging was also employed in studying *in vivo* or *in vitro* gene delivery, including pDNA, siRNA, shDNA. However, to fulfill the delivery of certain gene sequences, it is essential to overcome physiologic barriers in biological circulation system and to achieve selective targeting of specific tissues or cells, thus cell imaging along this research direction has been mainly focused on understanding and resolving those issues such as hepatic uptake of genetic materials, their interactions with plasma components and cell surface, genetic materials trafficking the plasma membrane, as well as their endosomal degradation and nuclear envelope.[84, 85] For example, Bazylinska et al. developed fluorescent nanocapsules as an efficient DNA delivery matrix, which was validated by cell internalization through confocal fluorescence images.[35] In addition, Dordelmann's group designed PLGA-chitosan based DNA delivery system with good transfection efficiency for epithelial cells, which was also confirmed through cell imaging test.[31] Moreover, as for the plasmid DNA sequence delivery, the access to nucleus is the pre-requisite for the success of such delivery system.[86] Recently Wang's group prepared HMGB1 (mediating nuclear importation),

PAMAM (inducing endosomal escape) and pDNA nanocomplex, which was further coated with Folic acid-PEG-chitosan for gene delivery. The fluorescence signal resulted from the expression of the delivered gene, and the delivery efficiency to nucleus were tracked via confocal fluorescence imaging. [87] Besides DNA, delivery of siRNA has also attracted increasing attention. EGFP-based self-assembled protein nanoparticles obtained by genetic engineering approach were utilized as vehicles to deliver siRNA into tumor cells, confirmed by the cell imaging. [88]

Besides the application in anti-cancer therapy, fluorescence-based cell imaging was also applied for studying the delivery matrixes in tissue therapy. As an example, synthetic fluorescent polymeric microparticles coated with layer-by-layer protein was used to target on sustainable release of bone morphogenic Protein-2 for bone tissue-engineering. Fluorescence imaging results indicated that intra- and extracellular targeting and drug releasing were accomplished using the biocompatible, non-toxic protein coated microparticles. [60]

On the other hand, as for the study of protein drug delivery, Monkare et al. developed a fluorescent hyaluronic acid based microneedles for intradermal delivery of the protein drugs, which enabled efficient penetration and rapid dissolution in the skin while preserving protein stability, via *ex vivo* confocal microscopy imaging studies. [89]

***Cell imaging for evaluation of delivery and phototherapy efficiency***

Besides delivering drugs for the purpose of cancer treatment, phototherapy technologies such as light-induced photodynamic (PDT) and photothermal (PTT) therapy have attracted much interests recently. They take advantages of the interactions between the specific band light and photosensitizer-carrying particles internalized by cells and thus achieve the cancer cell apoptosis or necrosis through the generation of reactive oxygen species or vibrational energy (heat).[90, 91]

Wen's group utilized rare earth ion Gd to assemble BSA into nanoparticles with encapsulated photosensitizer chlorin e6 (Ce6) for more efficient photodynamic therapy when compared to commercially used Gd-DTPA.[92] Song et al. fabricated polypyrrole nanoparticles with BSA as the stabilizing agent, which was pre-conjugated with photosensitizer Ce6, thus endowing both imaging and therapy functions.[91] The facilely obtained PPy@BSA-Ce6 nanoparticles served as not only PDT and PTT agents, but also fluorescence and MRI probe (after the labeling of contrast agent Gd). Consequently, a remarkably synergistic therapeutic effect on *in vitro* cancer cell experiment and *in vivo* tumor mice model was achieved through combined PDT and PTT treatment. Furthermore, Cheng's group applied magnetic nanocomposite composing of photosensitizer pyropheophorbide-a (PPA) coated fluorescent chitosan for photodynamic therapy, which was confirmed by cell imaging. After photodynamic therapy, the population of HeLa cancer cells significantly decreased when compared to the control experiment.[41] As another light-induced therapy agent, phthalocyanine (ZnPc) was used to modify the surface of chitosan nanoparticles for photodynamic and photothermal therapy. Cell internalization of nanoparticles was probed and confirmed by cell imaging which was also used to show the therapy efficiency via *in vivo* tumor size change before and after treatment measured at different time intervals. [93]

## *1.4 Motivation, and Objectives*

Nowadays, non-invasive bio-imaging techniques (including MRI, CT, PECT and PET) have been widely used for diagnosis and therapy relevant to medical applications. Molecular imaging would be the next direction of medical imaging, as it possesses both temporal and spatial resolution to track and record the arrangement and reactions of molecular or cellular processes. Due to its high sensitivity, rapid imaging speed, easy operation and relatively low cost, fluorescence based imaging technology has been employed as a promising molecular imaging

technique in both cell imaging and non-invasive *in vivo* imaging applications. Therefore, fluorescent materials based on natural polymer or hybrid synthetic-natural polymer with good biocompatibility and biodegradability have been extensively employed in fluorescence-based bio-imaging studies. Controlled degradation study is significant not only for sustained release fashion, but also for essential for tissue engineering. Thus the topic of my PhD thesis is bio-imaging assisted *in vivo* and *in vitro* degradation kinetics study of protein based hydrogels and particles.

There existed several issues in current fluorescence hydrogels and particles utilized for *in vivo* degradation tracking and monitoring. Firstly, most of the synthetic polymers are lacking of good biodegradability. Also, current investigations mainly engage the chemical fluorophores incorporated in the polymeric matrix, which could greatly increase the cytotoxicity of the synthesized materials, cause leaking problems of the fluorophores, and suffer from the potential photo-bleaching issue. All these issues might cause problems in *in vivo* biodegradation tracking and monitoring via non-invasive fluorescence imaging, since the fluorescence decay would entangle the degradability of the materials and photo-bleaching of the fluorophores at the same time. Moreover, *in vivo* degradation of the materials have been mainly studied via fluorescence decay imaging as aforementioned, there is no fundamental mathematical model proposed to describe the degradation of the injected materials. Even though some researches for *in vivo* degradation investigations have utilized either simple exponential or linear fitting model to match the extracted data, there is no delicate mathematical formula with meaningful parameters to completely depict the complicated *in vivo* degradation of injected degradable materials.

In our approach, we adopted Bovine Serum Albumin (BSA) as the natural polymer material, which is low-cost, biocompatible, biodegradable and high soluble in aqueous solution, and

glutaraldehyde as the efficient cross-linker, to prepare novel auto-fluorescence hydrogel and particles without any chemical fluorophores embedded. Prior to the *in vivo* or *in vitro* studies, a freeze-drying or spray-drying process was applied in order to remove all the glutaraldehyde residues to avoid its negative effect on the biocompatibility of as-prepared samples. A series of studies on cytotoxicity, histological analysis and *in vitro* digestion demonstrated that the as-prepared autofluorescnece hydrogels and particles possessed good biocompatibility and biodegradability. Besides the merits of novel autofluorescent materials themselves, mathematical models have also been proposed based on their *in vivo* degradation, where the extracted fluorescence intensity trends from the real-time fluorescence imaging were in good agreement of the proposed models. To further explore enzymatic degradation mechanism of single autofluorescent BSA matrix, degradation of single microspheres were tracked by CLSM as different concentrations of enzyme were applied. A mathematical model, complexing gel swelling, enzyme and fluorophores diffusion, was proposed to describe the enzymatic degradation mechanism.

**Reference**


1. Shen, W., Lammertink, R. G., Sakata, J. K., Kornfield, J. A. and Tirrell, D. A. (2005) Assembly of an artificial protein hydrogel through leucine zipper aggregation and disulfide bond formation. Macromolecules, **38,** 3909-3916.
2. Peppas, N. A., Hilt, J. Z., Khademhosseini, A. and Langer, R. (2006) Hydrogels in biology and medicine: from molecular principles to bionanotechnology. Advanced Materials, **18,** 1345-1360.
3. Drury, J. L. and Mooney, D. J. (2003) Hydrogels for tissue engineering: scaffold design variables and applications. Biomaterials, **24,** 4337-4351.
4. Lee, K. Y. and Mooney, D. J. (2001) Hydrogels for tissue engineering. Chemical Reviews, **101,** 1869-1880.
5. Chen, J., Dong, Q., Ma, X., Fan, T.-H. and Lei, Y. (2016) Repetitive Biomimetic Self-healing of $Ca^{2+}$-Induced Nanocomposite Protein Hydrogels. Scientific Reports, **6**, Artcile# 30804.
6. Chen, J., Ma, X., Dong, Q., Song, D., Hargrove, D., Vora, S. R., Ma, A. W., Lu, X. and Lei, Y. (2016) Self-healing of thermally-induced, biocompatible and biodegradable protein hydrogel. RSC Advances, **6,** 56183-56192.
7. Vermonden, T., Censi, R. and Hennink, W. E. (2012) Hydrogels for protein delivery. Chemical Reviews, **112,** 2853-2888.
8. Volodkin, D. V., von Klitzing, R. and Möhwald, H. (2010) Pure protein microspheres by calcium carbonate templating. Angewandte Chemie, **122,** 9444-9447.

9. Sivadas, N., O'Rourke, D., Tobin, A., Buckley, V., Ramtoola, Z., Kelly, J. G., Hickey, A. J. and Cryan, S.-A. (2008) A comparative study of a range of polymeric microspheres as potential carriers for the inhalation of proteins. International Journal of Pharmaceutics, **358,** 159-167.
10. Wei, W., Wang, L.-Y., Yuan, L., Wei, Q., Yang, X.-D., Su, Z.-G. and Ma, G.-H. (2007) Preparation and application of novel microspheres possessing autofluorescent properties. Advanced Functional Materials, **17,** 3153-3158.
11. Hanes, J., Chiba, M. and Langer, R. (1995) Polymer microspheres for vaccine delivery. ed. Springer.
12. Lee, S. H., Heng, D., Ng, W. K., Chan, H.-K. and Tan, R. B. (2011) Nano spray drying: a novel method for preparing protein nanoparticles for protein therapy. International Journal of Pharmaceutics, **403,** 192-200.
13. Gülseren, İ., Fang, Y. and Corredig, M. (2012) Whey protein nanoparticles prepared with desolvation with ethanol: Characterization, thermal stability and interfacial behavior. Food Hydrocolloids, **29,** 258-264.
14. Sundar, S., Kundu, J. and Kundu, S. C. (2010) Biopolymeric nanoparticles. Science and Technology of Advanced Materials, **11,** Article# 014104.
15. Lavis, L. D. and Raines, R. T. (2008) Bright ideas for chemical biology. ACS Chemical Biology, **3,** 142-155.
16. Qin, W., Ding, D., Liu, J., Yuan, W. Z., Hu, Y., Liu, B. and Tang, B. Z. (2012) Biocompatible Nanoparticles with Aggregation- Induced Emission Characteristics as Far- Red/Near- Infrared Fluorescent Bioprobes for In Vitro and In Vivo Imaging Applications. Advanced Functional Materials, **22,** 771-779.
17. Artzi, N., Oliva, N., Puron, C., Shitreet, S., Artzi, S., Bon Ramos, A., Groothuis, A., Sahagian, G. and Edelman, E. R. (2011) In vivo and in vitro tracking of erosion in biodegradable materials using non-invasive fluorescence imaging. Nature Materials, **10**, 704-709.
18. Berdichevski, A., Yameen, H. S., Dafni, H., Neeman, M. and Seliktar, D. (2015) Using bimodal MRI/fluorescence imaging to identify host angiogenic response to implants. Proceedings of the National Academy of Sciences, **112,** 5147-5152.
19. Shibata, H., Heo, Y. J., Okitsu, T., Matsunaga, Y., Kawanishi, T. and Takeuchi, S. (2010) Injectable hydrogel microbeads for fluorescence-based in vivo continuous glucose monitoring. Proceedings of the National Academy of Sciences, **107,** 17894-17898.
20. Liu, W., Zhang, W., Yu, X., Zhang, G. and Su, Z. (2016) Synthesis and biomedical applications of fluorescent nanogels. Polymer Chemistry, **7,** 5749-5762.
21 Dong, X., Wei, C., Liu, T. and Lv, F. (2015) Protoporphyrin incorporated alginate hydrogel: preparation, characterization and fluorescence imaging in vivo. RSC Advances, **5,** 96336-96344.
22. Zhang, Y., Rossi, F., Papa, S., Violatto, M. B., Bigini, P., Sorbona, M., Redaelli, F., Veglianese, P., Hilborn, J. and Ossipov, D. A. (2016) Non-invasive in vitro and in vivo monitoring of degradation of fluorescently labeled hyaluronan hydrogels for tissue engineering applications. Acta Biomaterialia, **30,** 188-198.
23. Cabral, J. D., McConnell, M. A., Fitzpatrick, C., Mros, S., Williams, G., Wormald, P. J., Moratti, S. C. and Hanton, L. R. (2015) Characterization of the in vivo host response to a bi- labeled chitosan- dextran based hydrogel for postsurgical adhesion prevention. Journal of Biomedical Materials Research Part A, **103,** 2611-2620.
24. Wang, Z., Fan, X., He, M., Chen, Z., Wang, Y., Ye, Q., Zhang, H. and Zhang, L. (2014) Construction of cellulose–phosphor hybrid hydrogels and their application for bioimaging. Journal of Materials Chemistry B, **2,** 7559-7566.
25. Cui, W., Wang, A., Zhao, J., Yang, X., Cai, P. and Li, J. (2016) Layer by layer assembly of albumin nanoparticles with selective recognition of tumor necrosis factor-related apoptosis-inducing ligand (TRAIL). Journal of Colloid and Interface Science, **465,** 11-17.
26. Cheng, J., Liu, Q., Shuhendler, A. J., Rauth, A. M. and Wu, X. Y. (2015) Optimizing the design and in vitro evaluation of bioreactive glucose oxidase-microspheres for enhanced cytotoxicity

against multidrug resistant breast cancer cells. Colloids and Surfaces B: Biointerfaces, **130,** 164-172.
27. Hu, C., Feng, H. and Zhu, C. (2012) Preparation and characterization of rifampicin-PLGA microspheres/sodium alginate in situ gel combination delivery system. Colloids and Surfaces B: Biointerfaces, **95,** 162-169.
28. Wang, H., Di, J., Sun, Y., Fu, J., Wei, Z., Matsui, H., del C Alonso, A. and Zhou, S. (2015) Biocompatible PEG- Chitosan@ Carbon Dots Hybrid Nanogels for Two- Photon Fluorescence Imaging, Near- Infrared Light/pH Dual- Responsive Drug Carrier, and Synergistic Therapy. Advanced Functional Materials, **25,** 5537-5547.
29. Luppi, B., Bigucci, F., Cerchiara, T. and Zecchi, V. (2010) Chitosan-based hydrogels for nasal drug delivery: from inserts to nanoparticles. Expert Opinion on Drug Delivery, **7,** 811-828.
30. Junginger, H. E. and Verhoef, J. C. (1998) Macromolecules as safe penetration enhancers for hydrophilic drugs—a fiction? Pharmaceutical Science & Technology Today, **1,** 370-376.
31. Dördelmann, G., Kozlova, D., Karczewski, S., Lizio, R., Knauer, S. and Epple, M. (2014) Calcium phosphate increases the encapsulation efficiency of hydrophilic drugs (proteins, nucleic acids) into poly (d, l-lactide-co-glycolide acid) nanoparticles for intracellular delivery. Journal of Materials Chemistry B, **2,** 7250-7259.
32. Lin, J., Li, Y., Li, Y., Wu, H., Yu, F., Zhou, S., Xie, L., Luo, F., Lin, C. and Hou, Z. (2015) Drug/dye-loaded, multifunctional PEG–chitosan–iron oxide nanocomposites for methotraxate synergistically self-targeted cancer therapy and dual model imaging. ACS Applied Materials & Interfaces, **7,** 11908-11920.
33. Jheng, P.-R., Lu, K.-Y., Yu, S.-H. and Mi, F.-L. (2015) Free DOX and chitosan-*N*-arginine conjugate stabilized indocyanine green nanoparticles for combined chemophotothermal therapy. Colloids and Surfaces B: Biointerfaces, **136,** 402-412.
34. Sachdev, A., Matai, I. and Gopinath, P. (2016) Carbon dots incorporated polymeric hydrogels as multifunctional platform for imaging and induction of apoptosis in lung cancer cells. Colloids and Surfaces B: Biointerfaces, **141,** 242-252.
35. Bazylińska, U. and Saczko, J. (2016) Nanoemulsion-templated polylelectrolyte multifunctional nanocapsules for DNA entrapment and bioimaging. Colloids and Surfaces B: Biointerfaces, **137,** 191-202.
36. Raber, A., Mittal, A., Schäfer, J., Bakowsky, U., Reichrath, J., Vogt, T., Schaefer, U., Hansen, S. and Lehr, C.-M. (2014) Quantification of nanoparticle uptake into hair follicles in pig ear and human forearm. Journal of Controlled Release, **179,** 25-32.
37. Andrei, G., Peptu, C. A., Popa, M., Desbrieres, J., Peptu, C., Gardikiotis, F., Costuleanu, M., Costin, D., Dupin, J. C. and Uhart, A. (2015) Formulation and evaluation of cefuroxim loaded submicron particles for ophthalmic delivery. International Journal of Pharmaceutics, **493,** 16-29.
38. Jalani, G., Naccache, R., Rosenzweig, D. H., Haglund, L., Vetrone, F. and Cerruti, M. (2016) Photocleavable hydrogel coated upconverting nanoparticles: a multifunctional theranostic platform for NIR imaging and on-demand macromolecular delivery. Journal of the American Chemical Society, **138**, 1078-1083.
39. Gui, R., Wang, Y. and Sun, J. (2014) Embedding fluorescent mesoporous silica nanoparticles into biocompatible nanogels for tumor cell imaging and thermo/pH-sensitive in vitro drug release. Colloids and Surfaces B: Biointerfaces, **116,** 518-525.
40. Salis, A., Fanti, M., Medda, L., Nairi, V., Cugia, F., Piludu, M., Sogos, V. and Monduzzi, M. (2016) Mesoporous Silica Nanoparticles Functionalized with Hyaluronic Acid and Chitosan Biopolymers. Effect of Functionalization on Cell Internalization. ACS Biomaterials Science & Engineering, **2,** 741-751.
41. Cheng, J., Tan, G., Li, W., Zhang, H., Wu, X., Wang, Z. and Jin, Y. (2016) Facile synthesis of chitosan assisted multifunctional magnetic Fe 3 O 4@ SiO 2@ CS@ pyropheophorbide-a fluorescent nanoparticles for photodynamic therapy. New Journal of Chemistry, **40,** 8522-8534.

42. Toman, P., Lien, C.-F., Ahmad, Z., Dietrich, S., Smith, J. R., An, Q., Molnár, É., Pilkington, G. J., Górecki, D. C. and Tsibouklis, J. (2015) Nanoparticles of alkylglyceryl-dextran-graft-poly (lactic acid) for drug delivery to the brain: Preparation and in vitro investigation. Acta Biomaterialia, **23,** 250-262.
43. Dai, T., Zhou, S., Yin, C., Li, S., Cao, W., Liu, W., Sun, K., Dou, H., Cao, Y. and Zhou, G. (2014) Dextran-based fluorescent nanoprobes for sentinel lymph node mapping. Biomaterials, **35,** 8227-8235.
44. Bonnard, T., Serfaty, J.-M., Journé, C., Noe, B. H. T., Arnaud, D., Louedec, L., Derkaoui, S. M., Letourneur, D., Chauvierre, C. and Le Visage, C. (2014) Leukocyte mimetic polysaccharide microparticles tracked in vivo on activated endothelium and in abdominal aortic aneurysm. Acta Biomaterialia, **10,** 3535-3545.
45. Menzel, E. and Farr, C. (1998) Hyaluronidase and its substrate hyaluronan: biochemistry, biological activities and therapeutic uses. Cancer Letters, **131,** 3-11.
46. Wade, R. J., Bassin, E. J., Rodell, C. B. and Burdick, J. A. (2015) Protease-degradable electrospun fibrous hydrogels. Nature Communications, **6**, Article#6639.
47. Ossipov, D., Kootala, S., Yi, Z., Yang, X. and Hilborn, J. n. (2013) Orthogonal chemoselective assembly of hyaluronic acid networks and nanogels for drug delivery. Macromolecules, **46,** 4105-4113.
48. Zhang, L., Gao, S., Zhang, F., Yang, K., Ma, Q. and Zhu, L. (2014) Activatable hyaluronic acid nanoparticle as a theranostic agent for optical/photoacoustic image-guided photothermal therapy. ACS Nano, **8,** 12250-12258.
49. Park, J., Ku, M., Kim, E., Park, Y., Hong, Y., Haam, S., Cheong, J.-H., Park, E. S., Suh, J.-S. and Huh, Y.-M. (2013) CD44-specific supramolecular hydrogels for fluorescence molecular imaging of stem-like gastric cancer cells. Integrative Biology, **5,** 669-672.
50. Hwang, Y.-J., Larsen, J., Krasieva, T. B. and Lyubovitsky, J. G. (2011) Effect of genipin crosslinking on the optical spectral properties and structures of collagen hydrogels. ACS Applied Materials & Interfaces, **3,** 2579-2584.
51. zur Nieden, N. I., Turgman, C. C., Lang, X., Larsen, J. M., Granelli, J., Hwang, Y.-J. and Lyubovitsky, J. G. (2015) Fluorescent hydrogels for embryoid body formation and osteogenic differentiation of embryonic stem cells. ACS Applied Materials & Interfaces, **7,** 10599-10605.
52. Ma, X., Sun, X., Hargrove, D., Chen, J., Song, D., Dong, Q., Lu, X., Fan, T.-H., Fu, Y. and Lei, Y. (2016) A Biocompatible and Biodegradable Protein Hydrogel with Green and Red Autofluorescence: Preparation, Characterization and In Vivo Biodegradation Tracking and Modeling. Scientific Reports, **6**, Article#19370.
53. Deshapriya, I. K., Stromer, B. S., Pattammattel, A., Kim, C. S., Iglesias-Bartolome, R., Gonzalez-Fajardo, L., Patel, V., Gutkind, J. S., Lu, X. and Kumar, C. V. (2015) Fluorescent, Bioactive Protein Nanoparticles (Prodots) for Rapid, Improved Cellular Uptake. Bioconjugate Chemistry, **26,** 396-404.
54. Cui, Y., Wang, Y. and Zhao, L. (2015) Cysteine–Ag Cluster Hydrogel Confirmed by Experimental and Numerical Studies. Small, **11,** 5118-5125.
55. Wang, H., Mao, D., Wang, Y., Wang, K., Yi, X., Kong, D., Yang, Z., Liu, Q. and Ding, D. (2015) Biocompatible fluorescent supramolecular nanofibrous hydrogel for long-term cell tracking and tumor imaging applications. Scientific Reports, **5**, Article#16680.
56. Wang, Z., Zhang, Y., Zhang, J., Huang, L., Liu, J., Li, Y., Zhang, G., Kundu, S. C. and Wang, L. (2014) Exploring natural silk protein sericin for regenerative medicine: an injectable, photoluminescent, cell-adhesive 3D hydrogel. Scientific Reports, **4**, Article#7064.
57. Yang, Q., Wei, L., Zheng, X. and Xiao, L. (2015) Single Particle Dynamic Imaging and Fe3+ Sensing with Bright Carbon Dots Derived from Bovine Serum Albumin Proteins. Scientific Reports, **5**, Article#17727.
58. Liu, Z., Chen, N., Dong, C., Li, W., Guo, W., Wang, H., Wang, S., Tan, J., Tu, Y. and Chang, J. (2015) Facile Construction of Near Infrared Fluorescence Nanoprobe with Amphiphilic Protein-

Polymer Bioconjugate for Targeted Cell Imaging. ACS Applied Materials & Interfaces, **7,** 18997-19005.
59. Yoon, H. K., Ray, A., Lee, Y.-E. K., Kim, G., Wang, X. and Kopelman, R. (2013) Polymer–protein hydrogel nanomatrix for stabilization of indocyanine green towards targeted fluorescence and photoacoustic bio-imaging. Journal of Materials Chemistry B, **1,** 5611-5619.
60. Omorphos, N. P., Kahn, L. and Kalaskar, D. M. (2015) Design of extracellular protein based particles for intra and extra-cellular targeting. Colloids and Surfaces B: Biointerfaces, **136,** 440-448.
61. Tang, Q., An, Y., Liu, D., Liu, P. and Zhang, D. (2014) Folate/NIR 797-conjugated albumin magnetic nanospheres: synthesis, characterisation, and in vitro and in vivo targeting evaluation. PloS One, **9,** e106483.
62. Gu, Y., Li, N., Gao, M., Wang, Z., Xiao, D., Li, Y., Jia, H. and He, H. (2015) Microwave-assisted synthesis of BSA-modified silver nanoparticles as a selective fluorescent probe for detection and cellular imaging of cadmium (II). Microchimica Acta, **182,** 1255-1261.
63. Chen, H., Li, S., Li, B., Ren, X., Li, S., Mahounga, D. M., Cui, S., Gu, Y. and Achilefu, S. (2012) Folate-modified gold nanoclusters as near-infrared fluorescent probes for tumor imaging and therapy. Nanoscale, **4,** 6050-6064.
64. Wang, C., Wang, C., Xu, L., Cheng, H., Lin, Q. and Zhang, C. (2014) Protein-directed synthesis of pH-responsive red fluorescent copper nanoclusters and their applications in cellular imaging and catalysis. Nanoscale, **6,** 1775-1781.
65. Niu, X., Chen, H., Wang, Y., Wang, W., Sun, X. and Chen, L. (2014) Upconversion fluorescence-SERS dual-mode tags for cellular and in vivo imaging. ACS Applied Materials & Interfaces, **6,** 5152-5160.
66. Sun, I. C., Eun, D. K., Koo, H., Ko, C. Y., Kim, H. S., Yi, D. K., Choi, K., Kwon, I. C., Kim, K. and Ahn, C. H. (2011) Tumor- Targeting Gold Particles for Dual Computed Tomography/Optical Cancer Imaging. Angewandte Chemie International Edition, **50,** 9348-9351.
67. Ding, D., Li, K., Qin, W., Zhan, R., Hu, Y., Liu, J., Tang, B. Z. and Liu, B. (2013) Conjugated Polymer Amplified Far- Red/Near- Infrared Fluorescence from Nanoparticles with Aggregation- Induced Emission Characteristics for Targeted In Vivo Imaging. Advanced Healthcare Materials, **2,** 500-507.
68. Lee, S. J., Koo, H., Lee, D.-E., Min, S., Lee, S., Chen, X., Choi, Y., Leary, J. F., Park, K. and Jeong, S. Y. (2011) Tumor-homing photosensitizer-conjugated glycol chitosan nanoparticles for synchronous photodynamic imaging and therapy based on cellular on/off system. Biomaterials, **32,** 4021-4029.
69. Kim, K., Kim, J. H., Park, H., Kim, Y.-S., Park, K., Nam, H., Lee, S., Park, J. H., Park, R.-W. and Kim, I.-S. (2010) Tumor-homing multifunctional nanoparticles for cancer theragnosis: simultaneous diagnosis, drug delivery, and therapeutic monitoring. Journal of Controlled Release, **146,** 219-227.
70. Wong, C., Stylianopoulos, T., Cui, J., Martin, J., Chauhan, V. P., Jiang, W., Popović, Z., Jain, R. K., Bawendi, M. G. and Fukumura, D. (2011) Multistage nanoparticle delivery system for deep penetration into tumor tissue. Proceedings of the National Academy of Sciences, **108,** 2426-2431.
71. Na, J. H., Lee, S., Koo, H., Han, H., Lee, K. E., Han, S. J., Choi, S. H., Kim, H., Lee, S. and Kwon, I. C. (2016) T 1-Weighted MR imaging of liver tumor by gadolinium-encapsulated glycol chitosan nanoparticles without non-specific toxicity in normal tissues. Nanoscale, **8,** 9736-9745.
72. Göpferich, A. (1996) Mechanisms of polymer degradation and erosion. Biomaterials, **17,** 103-114.
73. Lee, H., Cusick, R. A., Browne, F., Kim, T. H., Ma, P. X., Utsunomiya, H., Langer, R. and Vacanti, J. P. (2002) Local delivery of basic fibroblast growth factor increases both angiogenesis and engraftment of hepatocytes in tissue-engineered polymer devices1. Transplantation, **73,** 1589-1593.
74. Ifkovits, J. L. and Burdick, J. A. (2007) Review: photopolymerizable and degradable biomaterials for tissue engineering applications. Tissue Engineering, **13,** 2369-2385.

75. Wang, W., Liu, J., Li, C., Zhang, J., Liu, J., Dong, A. and Kong, D. (2014) Real-time and non-invasive fluorescence tracking of in vivo degradation of the thermosensitive PEGlyated polyester hydrogel. Journal of Materials Chemistry B, **2,** 4185-4192.
76. Ma, X., Hargrove, D., Dong, Q., Song, D., Chen, J., Wang, S., Lu, X., Cho, Y. K., Fan, T.-H. and Lei, Y. (2016) Novel green and red autofluorescent protein nanoparticles for cell imaging and in vivo biodegradation imaging and modeling. RSC Advances, **6,** 50091-50099.
77. Ma, X., Wang, T., Song, D., Hargrove, D., Dong, Q., Luo, Z., Chen, J., Lu, X., Luo, Y. and Fan, T.-H. (2016) Protein Microspheres with Unique Green and Red Autofluorescence for Noninvasively Tracking and Modeling Their in Vivo Biodegradation. ACS Biomaterials Science & Engineering, **2,** 954-962.
78. Tsong, T. Y. (1991) Electroporation of cell membranes. Biophysical journal, **60,** 297-306.
79. Marsh, M. and McMahon, H. (1999) The structural era of endocytosis. Science, **285,** 215-220.
80. Xia, B., Wang, X., He, F., Cui, Q. and Li, L. (2012) Self-assembly of conjugated polymer on hybrid nanospheres for cellular imaging applications. ACS Applied Materials & Interfaces, **4,** 6332-6337.
81. Tzeng, Y. K., Faklaris, O., Chang, B. M., Kuo, Y., Hsu, J. H. and Chang, H. C. (2011) Superresolution Imaging of Albumin- Conjugated Fluorescent Nanodiamonds in Cells by Stimulated Emission Depletion. Angewandte Chemie International Edition, **50,** 2262-2265.
82. Zhang, Y., Yue, X., Kim, B., Yao, S., Bondar, M. V. and Belfield, K. D. (2013) Bovine serum albumin nanoparticles with fluorogenic near-IR-emitting squaraine dyes. ACS Applied Materials & Interfaces, **5,** 8710-8717.
83. Sinha, V. and Trehan, A. (2003) Biodegradable microspheres for protein delivery. Journal of Controlled Release, **90,** 261-280.
84. Wagstaff, K. M. and Jans, D. A. (2007) Nucleocytoplasmic transport of DNA: enhancing non-viral gene transfer. Biochemical Journal, **406,** 185-202.
85. Khalil, I. A., Kogure, K., Akita, H. and Harashima, H. (2006) Uptake pathways and subsequent intracellular trafficking in nonviral gene delivery. Pharmacological Reviews, **58,** 32-45.
86. Lu, Y. and Low, P. S. (2012) Folate-mediated delivery of macromolecular anticancer therapeutic agents. Advanced Drug Delivery Reviews, **64,** 342-352.
87. Wang, M., Hu, H., Sun, Y., Qiu, L., Zhang, J., Guan, G., Zhao, X., Qiao, M., Cheng, L. and Cheng, L. (2013) A pH-sensitive gene delivery system based on folic acid-PEG-chitosan–PAMAM-plasmid DNA complexes for cancer cell targeting. Biomaterials, **34,** 10120-10132.
88. Guan, X., Hu, X., Cui, F., Li, Y., Jing, X. and Xie, Z. (2015) EGFP- Based Protein Nanoparticles with Cell- Penetrating Peptide for Efficient siRNA Delivery. Macromolecular Bioscience, **15,** 1484-1489.
89. Mönkäre, J., Nejadnik, M. R., Baccouche, K., Romeijn, S., Jiskoot, W. and Bouwstra, J. A. (2015) IgG-loaded hyaluronan-based dissolving microneedles for intradermal protein delivery. Journal of Controlled Release, **218,** 53-62.
90. Yao, J., Yang, M. and Duan, Y. (2014) Chemistry, biology, and medicine of fluorescent nanomaterials and related systems: New insights into biosensing, bioimaging, genomics, diagnostics, and therapy. Chemical Reviews, **114,** 6130-6178.
91. Song, X., Liang, C., Gong, H., Chen, Q., Wang, C. and Liu, Z. (2015) Photosensitizer-Conjugated Albumin− Polypyrrole Nanoparticles for Imaging- Guided In Vivo Photodynamic/Photothermal Therapy. Small, **11,** 3932-3941.
92. Wen, Y., Dong, H., Li, Y., Shen, A. and Li, Y. (2016) Nano-assembly of bovine serum albumin driven by rare-earth-ion (Gd) biomineralization for highly efficient photodynamic therapy and tumor imaging. Journal of Materials Chemistry B, **4,** 743-751.
93. Han, J., Xia, H., Wu, Y., Kong, S. N., Deivasigamani, A., Xu, R., Hui, K. M. and Kang, Y. (2016) Single-layer MoS 2 nanosheet grafted upconversion nanoparticles for near-infrared fluorescence imaging-guided deep tissue cancer phototherapy. Nanoscale, **8,** 7861-7865.

# Chapter 2

## A Biocompatible and Biodegradable Protein Hydrogel with Green and Red Autofluorescence: Preparation, Characterization and *In Vivo* Biodegradation Tracking and Modeling

**Abstract**

Because of its good biocompatibility and biodegradability, albumins such as bovine serum albumin (BSA) and human serum albumin (HSA) have found a wide range of biomedical applications. Herein, we report that glutaraldehyde cross-linked BSA (or HSA) forms a novel fluorescent biological hydrogel, exhibiting new green and red autofluorescence *in vitro* and *in vivo* without the use of any additional fluorescent labels. UV-vis spectra studies, in conjunction with the fluorescence spectra studies including emission, excitation and synchronous scans, indicated that three classes of fluorescent compounds are presumably formed during the gelation process. SEM, FITR and mechanical tests were further employed to investigate the morphology, the specific chemical structures and the mechanical strength of the as-prepared autofluorescent hydrogel, respectively. Its biocompatibility and biodegradability were also demonstrated through extensive *in vitro* and *in vivo* studies. More interestingly, the strong red autofluorescence of the as-prepared hydrogel allows for conveniently and non-invasively tracking and modeling its *in vivo* degradation based on the time-dependent fluorescent images of mice. A mathematical model was proposed and was in good agreement with the experimental results. The developed facile strategy to prepare novel biocompatible and biodegradable autofluorescent protein hydrogels could significantly expand the scope of protein hydrogels in biomedical applications.

## *2.1 Introduction*

Cross-linked hydrogel networks, imbibing a large volume of water and maintaining three dimensional structure,[1, 2] have been widely investigated for biomedical applications ranging from drug delivery to tissue engineering.[2-4] Many materials, including natural proteins and synthetic polymers, have been used to prepare hydrogels.[5] Among different hydrogels that have been reported, protein hydrogels are of great interest because there is only a slight frictional irritation upon their implantation in tissue, due to their softness and good biocompatibility.[6] In addition, protein hydrogels generally exhibit a highly porous structure, relatively good hydrophilicity, biodegradability, and also enhanced biocompatibility, which could greatly suppress the foreign body reaction for *in vivo* applications.[7] Nowadays, protein-based hydrogels containing collagen and gelatin are most widely synthesized using glutaraldehyde or water-soluble carbodiimides[8] as the cross-linkers. Beyond the aforementioned proteins and their based hydrogels, bovine serum albumin (BSA) and human serum albumin (HSA) and their based hydrogels have also found plenty of applications owing to its low cost, stability, unusual ligand-binding properties and high solubility.[9, 10] BSA (or HSA) has two tryptophan residues that are responsible for its intrinsic fluorescence (excitation/emission of 279 nm/348 nm), however, the excitation and emission in the UV range significantly diminish any *in vivo* application of using their intrinsic fluorescence. Glutaraldehyde (GA), a linear 5-carbon dialdehyde with a formula of $CH_2(CH_2CHO)_2$, is an apparent, colorless, pungent oily liquid that is soluble in all proportions in water and alcohol, as well as in organic solvents.[11] Glutaraldehyde is a widely used cross-linker because of its low cost, high reactivity, and good efficiency to react with the amine groups to generate thermal and chemical stable crosslinks compared with other aldehydes.[12] Although several functional groups in protein can react with

glutaraldehyde in aqueous solution,[11] including amine, thiol, imidazole, etc.,[13] GA possesses high reactivity with lysine residues (ϵ-amino groups).[11] Therefore, GA is predominantly reacted with the ϵ-amino groups of lysine in protein to form major intermolecular cross-linkages.[13] Although GA has been previously used in BSA nanoparticle preparation[14], there is no report on its use to prepare hydrogels with green and red autofluorescence.

In the past few decades, fluorescent hydrogel has attracted more and more research interests due to its practical application as a convenient tracer in biomedical engineering.[15, 16] Many fluorescence-based chemical, physical and biological hydrogels have been developed for glucose sensing[17, 18], insulin-sensing[19], temperature-responsive sensing[20], as well as for tracking *in vitro* and *in vivo* degradation of hydrogels.[15, 16] However, to synthesize those fluorescent hydrogels, fluorophores are either chemically or physically immobilized in the hydrogel matrix, endowing the fluorescence property to the hydrogels. Although different covalent conjugation and physical entrapment methods have been developed to anchor fluorophores, their applicability is greatly limited because of the complexity of synthetic routes, the potential leakage and photobleaching of fluorophores, the influence of fluorescent labels on the degradation pattern, as well as the concerns of biocompatibility and biodegradability of those fluorophores. Ideally, an autofluorescent protein hydrogel with a suitable excitation/emission wavelength is highly favorable in this regard.

In this study, we report a unique glutaraldehyde cross-linked albumin (BSA or HSA) hydrogel which exhibits strong green and red autofluorescence over a large excitation wavelength range. To the best of our knowledge, such unique green and red fluorescence of BSA (or HSA) hydrogel has not been reported in literature. The absorption and fluorescence properties of the as-prepared autofluorescent hydrogel were extensively investigated through UV-vis spectra and the

fluorescence spectra including emission, excitation and synchronous scans. After lyophilization to remove unreacted glutaraldehyde, Scanning Electron Microscopy (SEM) and Fourier Transform Infrared Spectroscopy (FTIR) were further employed to investigate the surface morphology and the specific chemical structures of the lyophilized hydrogel sample, respectively. The hydrogel also exhibited high toughness according to the compression and tensile tests. Finally its biocompatibility and biodegradability were demonstrated through extensive *in vitro* and *in vivo* studies. More interestingly, the *in vivo* degradation of autofluorescent hydrogel can be non-invasively tracked using fluorescence images, which provided a convenient way to model *in vivo* biodegradation of the protein hydrogel from a new perspective. The degradation/diffusion trends predicted by the proposed mathematical model were in good agreement with the time-dependent fluorescence images of mice. These results also indicate that the newly formed fluorophores in the autofluorescent BSA hydrogel are stable and not degraded after protein degradation until they are finally absorbed into circulation. An attempt to identify the chemical structures of newly formed fluorophores in proteinase K digested hydrogel sample using LC-MS turns out to be challenging due to the complexity of GA cross-linked BSA hydrogel. The developed facile strategy to prepare a unique autofluorescent protein hydrogel could significantly expand the scope of protein hydrogels in biomedical applications.

## *2.2 Experimental*

### 2.2.1 Cross-linked BSA or HSA Hydrogel

In this study, BSA and glutaraldehyde solution was mixed quickly with the final BSA and GA concentrations of 20% and 1%, respectively. After tens of seconds, autofluorescent BSA hydrogel was prepared. The gelation time was determined using an reported inverted tube method.[21] BSA concentration varying from 10%~30% is also able to be cross-linked by 1%

glutaraldehyde to form the unique autofluorescent hydrogel. In addition, human serum albumin (HSA) can be used to replace BSA and form autofluorescent hydrogel too.

### 2.2.2 Freeze-Dry BSA Hydrogel

The BSA hydrogel was prepared in a small tuber and hung using a stainless steel holder in order to freeze the hydrogel in liquid nitrogen. Then the freeze-dry flask containing the stainless steel holder was placed on a vacuum lyophilization equipment for an appropriate time to remove water in hydrogel. The time for lyophilization was determined by the volume of the hydrogel sample.

### 2.2.3 Characterization of the BSA hydrogel

In the UV-vis study, BSA hydrogel was prepared in a 3 mL cuvette, and the BSA solution was prepared in a quartz cuvette as a comparison. The UV-vis spectra were collected from 200 nm to 800 nm using a Varian Cary 50 Scan UV-Visible Spectrophotometer.

To obtain the fluorescent images, two sets of filters were employed, including Ex/Em=470 nm/530 nm and Ex/Em=595 nm/630 nm. The Excitation filter was placed in front of the LED light to excite the hydrogel with the specific wavelength and the Emission filter was attached on the camera to record the emission image of the BSA hydrogel.

Varian Cary Eclipse Fluorescence Spectrophotometer was used in the fluorescence spectra study. BSA hydrogel was prepared in a 3 mL cuvette. In the emission scan, excitation wavelength was set from 370 nm to 600 nm with a 10 nm increments in each scan and emission wavelength was set from a wavelength slightly above the excitation wavelength to 800 nm. In the excitation scan, emission wavelength was set at 510 nm, 550 nm, and 602 nm, respectively, and the excitation scanned from an appropriate wavelength to a wavelength slightly less than the emission

wavelength. The synchronous scan was conducted with the start wavelength of 400 nm, the stop wavelength of 700 nm and a Delta of 20 nm.

Surface morphology of the prepared hydrogel was studied using JEOL 6335 Field Emission Scanning Electron Microscope (FESEM) operated at an accelerating voltage of 10 kV and 12 μA. BSA hydrogel was prepared and flash-frozen in liquid nitrogen and lyophilized. Prior to imaging, the sample cross-sections were cut by razor blade and mounted on double-sided carbon tape stuck on SEM stubs. Further, the samples were sputtered coated with Au/Pd alloy for improved conductivity. Attenuated total reflectance (ATR) infrared spectra of dry BSA hydrogel and BSA powder were obtained with a Thermo Nicolet IR 560 system, using a Zn-Se ATR accessory (Thermo Electron Corporation, PA). Each sample was placed against the ATR element and the spectra were collected in the range of 500 - 4000 $cm^{-1}$ using 128 scans at a resolution of 4 $cm^{-1}$. After acquisition, the IR spectra were baseline corrected for carbon dioxide peak at approximately 2750 $cm^{-1}$.

Mechanical analysis of the hydrogel samples were performed on TA instruments Q800 under controlled force (compression and tensile mode). A pair of compression disc clamps of 15 mm was used on uniform hydrogel sample. Constant preload force of 0.01 N and ramp force of 0.5 N/min was applied up to 18 N at 37 °C.

### 2.2.4 *In vitro* cytotoxicity test

BSA hydrogel was prepared as the previous procedure and then 100 mg freeze-dried hydrogel was soaked in 5 mL (2%) Dulbecco's Modified Eagle Medium (DMEM) and incubate at 37 ℃ for 24 h. Concurrently seed 5,000 A549 cells per well to 96 well plate and incubate it overnight. Next, dilute the 2% hydrogel extract solution with DMEM and then treat the cell with 0, 0.2, 0.4, 0.6, 0.8, 1% hydrogel extract solution (3 wells for each sample) and keep one column with

DEME only as the blank. After 24 hours incubation, the samples were removed and replaced with the fresh medium (100 μL per well). Finally 10 μL of CCK-8 solution was loaded to each well and the absorption at 450 nm on a microplate reader was recorded after 1 hour incubation. The cell survival percentage was calculated with following equation:

$$Cell\ survival\ \% = (A_{sample} - A_{blank}) / (A_0 - A_{blank}) \times 100\%$$

### 2.2.5 *In vitro* enzymatic biodegradation test

*In vitro* degradation test was conducted in a small glass vial containing a 300 μL BSA hydrogel and 5 mL of PBS buffer (pH 7.4 10 mM) with a relative higher proteinase K concentration at 1 mg/mL. The optical pictures were recorded at different time intervals (0 h, 6 h, 18 h, 24 h, 36 h, and 42 h).

### 2.2.6 *In vivo* biodegradability and biocompatibility study

All studies were performed with a University of Connecticut Institutional Animal Care and Use Committee approved protocol and the methods were carried out in accordance with the approved guidelines. Freeze-dried sample was autoclaved first, and then soaked in the sterilized PBS buffer to absorb water and swell back to form hydrogel. Before injection of BSA hydrogel, the mouse was anesthetized using isoflurane and the implantation area was cleaned with an alcohol swab. Then the hydrogel prepared in advance was subcutaneously injected in two 7-month old Athymic Nude mice (Mouse 267 and Mouse 271) and a 2-month old Athymic Nude mice (Mouse 189) using an modified 18-gauge indwelling needle assembly. The whole needle assembly was then removed and the area was wiped again with an alcohol swab to clean the area before returning the mouse back to the cage. The area was then monitored for inflammation and fluorescent images continuously. After BSA hydrogel injection, the 7-month old Mouse 271 and

Mouse 267 were sacrified at 20 days and 2 months, respectively, while the 2-month old Mouse 189 was sacrificed at 27 days, to conduct the histology analysis.

## *2.3 Results and Discussions*

As reported, glutaraldehyde predominantly crosslinks ϵ-amino groups of lysine within BSA.[13] Since the concentration of BSA solution used in this study is very high, the intermolecular cross-linking process generates extensive 3D networks, thus forming a protein hydrogel. To investigate the gelation time, we employed a test tube inversion method reported in literature.[21] The time when the polymer solution stops flowing out of inverted tubes was recorded at 25 °C. Briefly, BSA was first dissolved in 0.01 M pH 7.4 PBS buffer solution and then glutaraldehyde was added into BSA solution as the cross-linker with the final concentration of 20% BSA and 1% GA. After adding glutaraldehyde, the clear dark yellow protein hydrogel which does not flow upon inversion, was obtained whitin 30-45 seconds (Figure 1a). Differential Scanning Calorimetry (DSC) and Thermogravimetric Analysis (TGA) techniques were employed to study the thermal properties (e.g., melting point and decompisiton temperature) of the cross-linked BSA hydrogel and the results (Figure S2) and discussion are presented in supplemental materials. The schematic representation of the GA cross-linked BSA hydrogel was presented in Figure 1b.

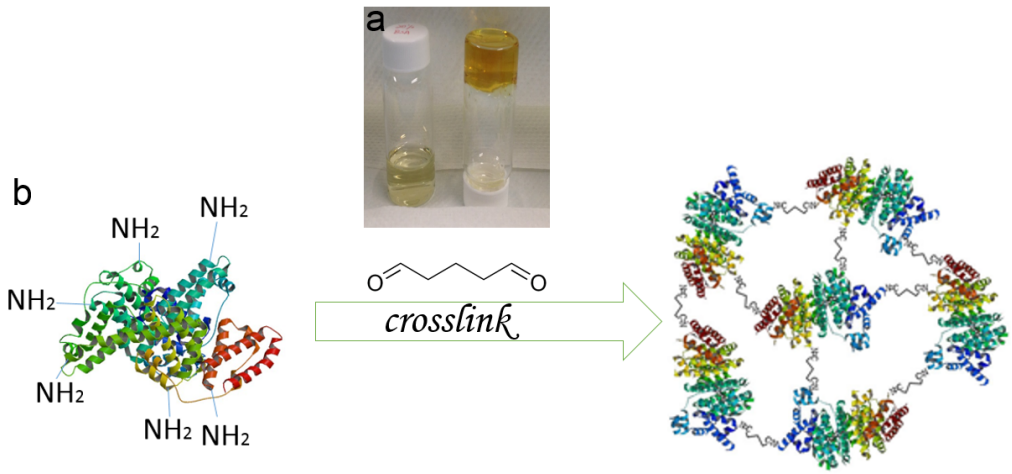

Figure 1. (a) The right vial contains BSA hydrogel after GA cross-linking, while the left vial contains 20% BSA solution as a comparison. (b) The schematic of GA-cross-linked BSA hydrogel (not in scale).

### 2.3.1 UV-vis study of cross-linked BSA hydrogel.

According to Figure 1, the cross-linking process by GA not only forms BSA hydrogel, but also probably produces new colorful compounds, endowing the obvious color difference between BSA hydrogel and BSA solution. Therefore, a UV-vis spectrum was employed as a useful probe for initial composition analysis. Spectral analysis shows that BSA in aqueous solution has a sharp absorption peak at λ=279 nm (Figure 2a), which is typical for BSA proteins. To investigate the newly formed colorful compounds in the cross-linked BSA hydrogel, UV-vis spectrum scanning from 300 nm to 800 nm was utilized (Figure 2b). Compared to the UV-vis spectrum of BSA solution, GA cross-linked BSA hydrogel showed three new broad peaks centered around 460 nm, 530 nm and 580 nm, respectively. This suggests that there might have three classes of compounds formed during BSA cross-linking by GA, which led to further investigation into the fluorescence properties of the GA cross-linked BSA hydrogel.

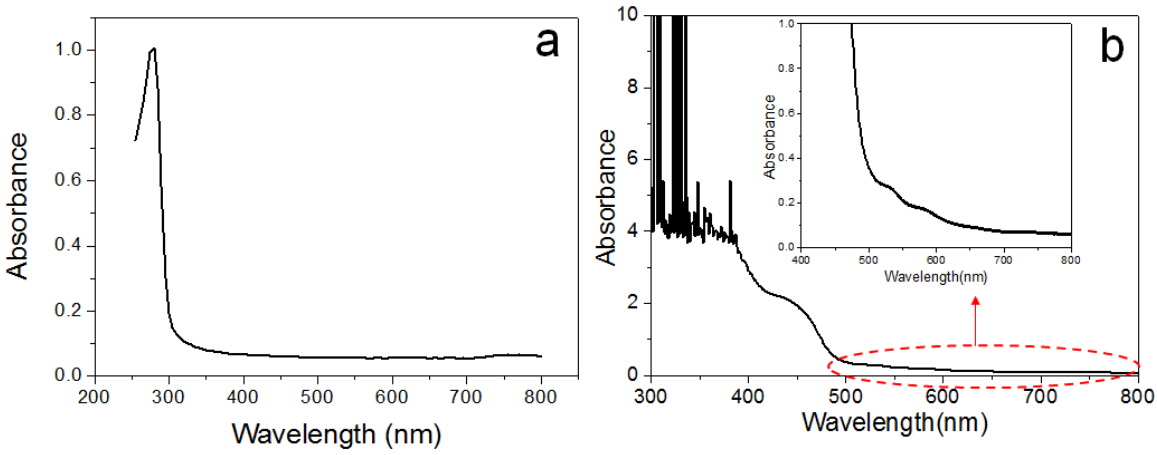


Figure 2. UV-vis spectra of BSA solution (a) and GA cross-linked BSA hydrogel (b), respectively

### 2.3.2 Fluorescent images of cross-linked BSA hydrogel.

BSA, a well-known protein fluorophore, has a strong emission at ~348 nm when it is excited at λ= 279 nm. However, according to the UV-vis spectrum of BSA hydrogel in Figure 2b, BSA hydrogel might exhibit fluorescence when excited in a broad wavelength range. To test the hypothesis, different optical filters (Ex=470 nm and Em=530 nm; Ex=595 nm and Em=630 nm) were first used to acquire fluorescent images of the cross-linked BSA hydrogel. Interestingly and unexpectedly, crosslinked BSA hydrogel exhibits strong green and red fluorescence, respectively (Figure 3). Under white light, the as-prepared BSA hydrogel is dark yellow color (Figure 3a). However, when BSA hydrogel was excited at a wavelength of λ=470 nm and λ= 595 nm, respectively, the BSA hydrogel exhibited a strong green fluorescence (Figure 3b) and red fluorescence (Figure 3c) when the images were collected using an optical bandpass filter with λ=530 nm and λ=630 nm, respectively. In conjunction with the results from UV-vis spectra, fluorescence images of BSA hydrogel suggested that there indeed have new classes of fluorescent molecules formed in the cross-linked BSA hydrogel. Besides BSA, human serum albumin (HSA) can also be cross-linked to show strong green and red autofluorescence (Figure 3d-e). For subsequent studies, only BSA cross-linked hydrogel is used due to its low cost compared to HSA.

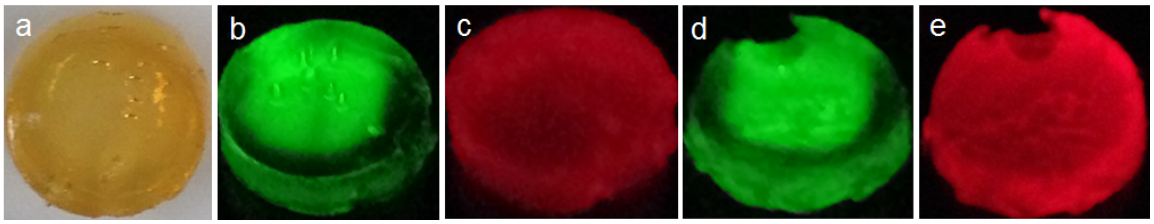


Figure 3**.** (a) BSA hydrogel under normal white light; (b) BSA hydrogel image (excited at 470 nm) is collected using a λ=530 nm optical filter; (c) BSA hydrogel image (excited at 595 nm) is collected using a λ=630 nm optical filter. (d) HSA hydrogel image (excited at 470 nm) is collected using a λ=530 nm optical filter. (e) HAS hydrogel image (excited at 595 nm) is collected using a λ= 630nm optical filter.

### 2.3.3 Fluorescence spectra study of cross-linked BSA hydrogel.

Emission spectra of BSA hydrogel is further recorded with a fluorometer. Total 20 individual emission spectra at sequential 10 nm increments of excitation wavelength were recorded. According to Figure 4 a and b, there existed obvious emission peaks in the green fluorescence wavelength range when it was excited at a wavelength between λ=370 nm and λ=530 nm. Moreover, it shows that the emission peak shifts slightly from λ=510 nm to λ=550 nm over the same excitation range. When excited at a wavelength between 520 nm and 590 nm, a broad emission peak centered around λ=602 nm appeared, which is attributed to the the observed red fluorescence of BSA and HSA hydrogels. Excitation scan was also conducted and the results (Figure 4c) suggest that the proper excitation wavelengths for the three emission peaks (510, 550 and 602 nm) are 478, 530, and 580 nm, respectively. Moreover, the synchronous scan in Figure 4d also shows distinct emission peaks which may correspond to three classes of fluorescent compounds in the cross-linked BSA hydrogel. These observations are not only in good agreement with the results suggested by UV-vis spectra in Figure 2, but also corroborate the strong green and red antofluorescence observed in Figure 3.

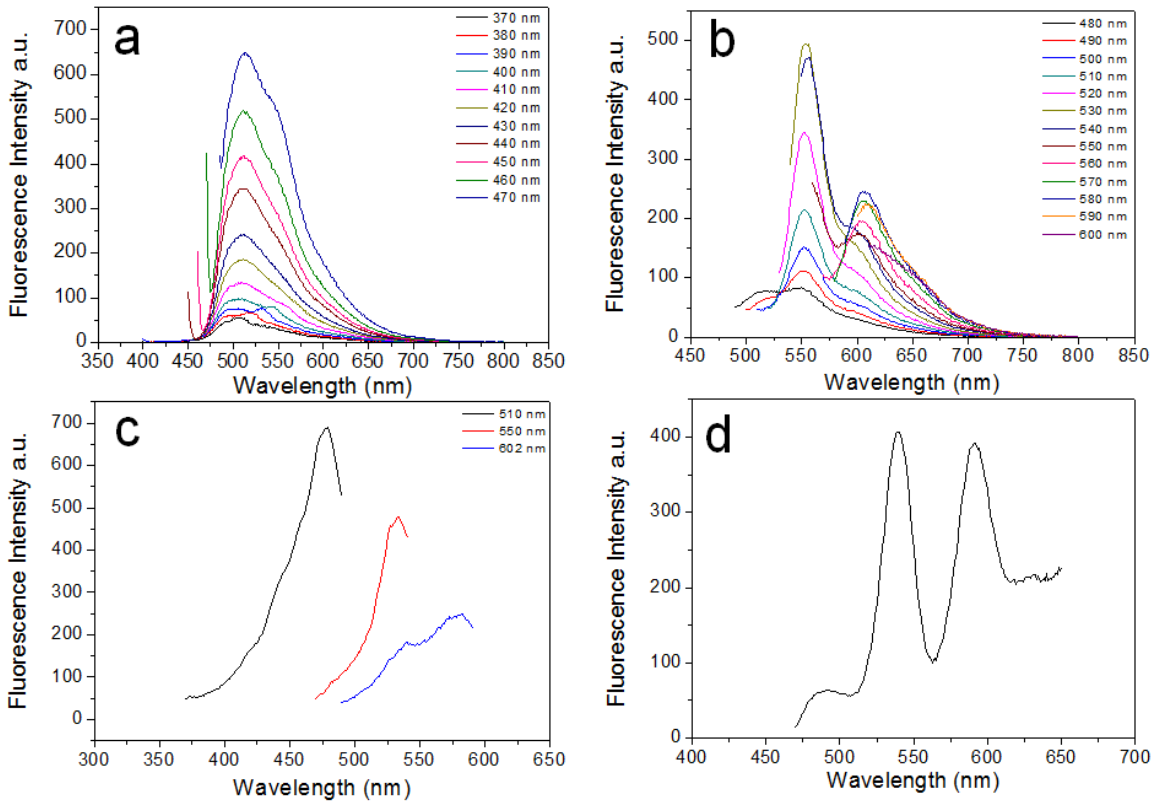


Figure 4. (a) and (b) Emission scans when excited between λ=370 nm and λ=600 nm, split into two figures for the sake of clear display. (c) Three Excitation scans with the Emission wavelength at λ=510 nm, 550 nm, 602 nm, respectively. (d) Synchronous scan.

### 2.3.4 SEM and FTIR characterization of cross-linked BSA hydrogel.

To characterize the morphology and specific functional groups of the cross-linked BSA hydrogel, SEM and FTIR were first employed. The cross-sectional interior structures of flash-frozen and lyophilized BSA hydrogels with different BSA concentrations (10%, 20% and 30%) are shown in Figure 5. All three BSA hydrogels exhibited a highly porous honeycomb-like structure with an irregular shape in which the three-dimensional, interconnected macropores represent water-filled areas, while the pore size features a BSA concentration-dependent property. In general, an increase in the concentration of BSA results in a smaller pore size, as expected. Specifically, the hydrogel with 10% BSA was characterized with an average pore size of 20 μm. The 20% BSA hydrogel exhibited a pore size of 10 μm, while the 30% BSA hydrogel exhibited a very dense

structure with an average pore size of 5 μm. For the FTIR study, a freeze-dried 20% BSA hydrogel sample and the native BSA powder were used. As shown in Figure 5d, both BSA powder and BSA hydrogel showed nearly the same FTIR spectrum with a fingerprint region at 1650 and 1530 $cm^{-1}$, representative for the BSA amide I and amide II bonds [22, 23], which suggests that the cross-linking process between -CHO in GA and -$NH_2$ in BSA may not form special functional groups except Schiff bond. However, one possibility we cannot rule out is that the formation of new chemical bonds (if any) could be too low to be detected in the FTIR spectrum due to the low sensitivity (5%) of the FTIR equipment.

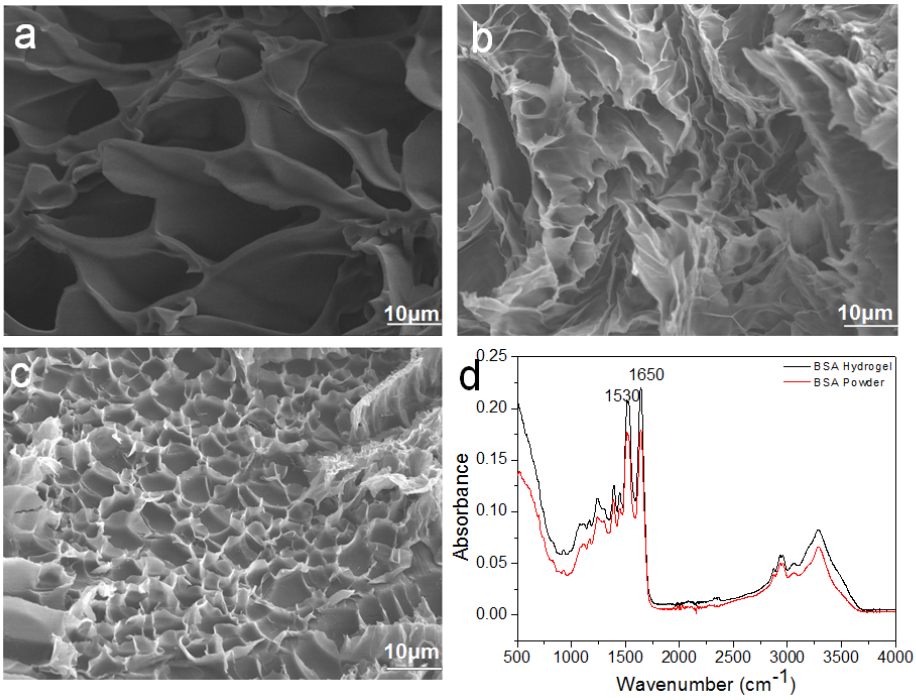


Figure 5. (a) The SEM image of 10% BSA hydrogel; (b) The SEM image of 20% BSA hydrogel; (c) The SEM image of 30% BSA hydrogel; (d) The FTIR spectra of BSA hydrogel and BSA powder, respectively.

### 2.3.5 Mechanical property studies of cross-linked BSA hydrogel.

As the mechanical integrity of a hydrogel is an important design specification for *in vitro* and *in vivo* applications, both compression and tensile tests have been widely used to examine the

mechanical properties of different types of hydrogels.[24] For *in vivo* applications, the hydrogel should be pliable enough to coexist with surrounding tissue but also possess enough structural integrity to withstand intraluminal and subcutaneous pressure from surrounding structures. Therefore, a compression analysis was first carried out (Figure 6a). To study the compressive performance of the BSA hydrogel, a constant preload force of 0.01 N and ramp force of 0.5 N/min up to 18 N at 37 °C was applied. The stress-strain characteristic of the BSA hydrogel displayed a typical trend for protein hydrogels. [25] The Young's modulus characterizes the pure elastic domain of a material where the deformation due to applied stress is reversible. However, the stress-strain curve for the BSA hydrogel investigated here is nonliner; hence a global Young's modulus of compression could not be determined. The experimental result also shows that the hydrogel has been pressed with dimensional changes under this force range and no breaking point of the hydrogels could be observed under pressures up to 18 N. A tensile mechanical measurement was also performed on the BSA hydrogel with a preload force of 0.01 N and ramp force of 0.05 N/min up to 18 N at 37 °C. Figure 6b shows a typical stress-strain curve of the hydrogel during a typical tensile test. [25] The hydrogel length can be elongated as much as 1.8 folds before rupture. Overall, the high molecular weight of BSA protein with extensive cross-linked covalent bonds through GA has led to a hydrogel with high mechanical strength. [25, 26]

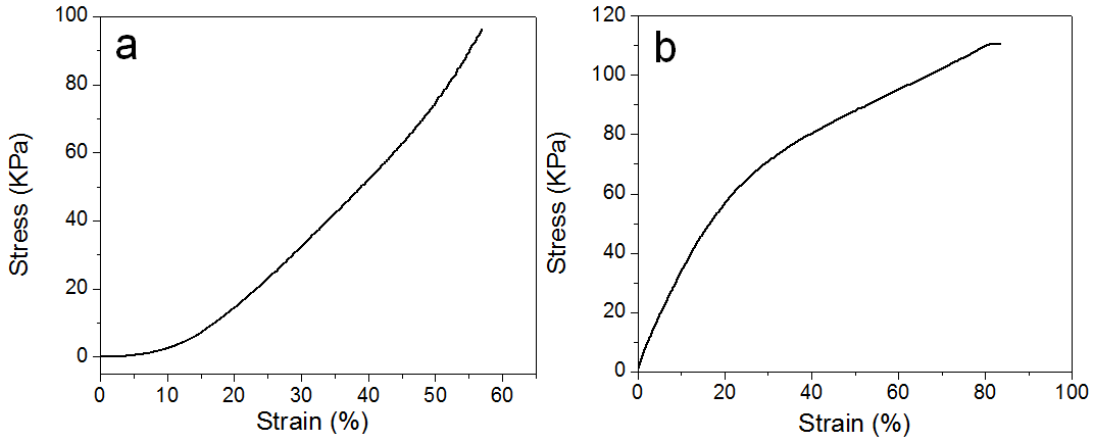


Figure 6. (a) Compression test and (b) Tensile test results.

### 2.3.6 Cytotoxicity and *in vitro* enzymatic degradation studies of cross-linked BSA hydrogel.

Injectable materials are advantageous in that they can be applied to tissue defects with irregular shapes and form tight interfaces with surrounding tissues. [27] As it is difficult to remove the unreacted residues after injection and curing, biocompatibility and biodegradability are two most important factors to evaluate the merits of hydrogels. Thus cytotoxicity was first conducted to evaluate *in vitro* biocompatibility of the BSA hydrogel using a cell-based indirect contact test. [27]

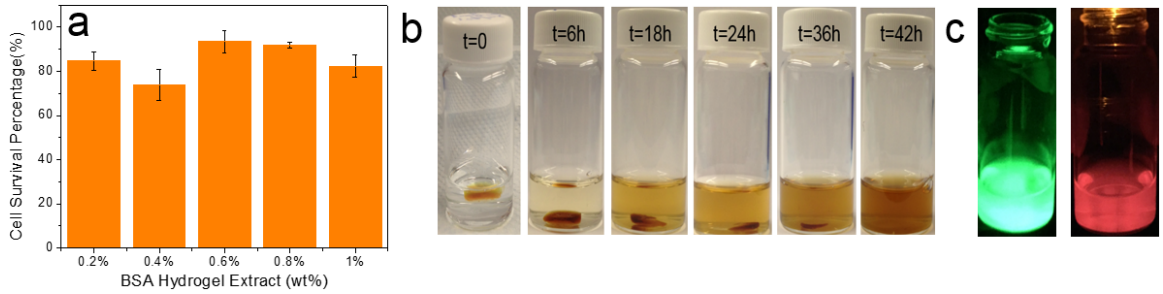


Figure 7**.** (a) Cell survival rate versus BSA hydrogel extract in cytotoxicity test; (b) BSA hydrogel digested by proteinase K; (c) Fluorescence images of the digested BSA hydrogel excited at a wavelength of λ=470 nm and λ= 595 nm and collected using a λ=530 nm optical filter and a λ= 630 nm optical filter, respectively.

Since glutaraldehyde has a certain level of cytotoxicity in the cells, the freeze-drying process was employed to eliminate the unreacted glutaraldehyde and the lyophilized BSA hydrogel was used. While there is some new fluorescent compounds formed during the cross-linking process**,** Figure

7a shows that more than 80% of the A549 cells remained alive after exposure to different concentrations of hydrogel extracts in media. These results indicate that the cross-linked BSA hydrogel and newly formed fluorescent compounds are relatively noncytotoxic, which provides solid ground for the latter *in vivo* biocompatibility test.

The *in vitro* biodegradability of the hydrogel was tested by adapting a similar proteinase K method reported by Zhao et al. [28] Proteinase K is a widely used enzyme for protein digestion, because it can hydrolyze the amine bonds and also break ester bonds. In order to track the color changes of the solution during the whole degradation process, the enzyme solution was not refreshed throughout the test. Considering the fact that the activity of the proteinase K gradually decreases over time, the proteinase K concentration used was 1 mg/mL. As shown in Figure 7b, the cross-linked BSA hydrogel was fully digested after a 42 h incubation at 37 °C. The color of the solution became brownish over time, which can be attributed to the release of the colorful fluorescent compounds accompanying the BSA hydrogel digestion. After the digestion, the solution also exhibited a strong green and red fluorescence (Figure 7 c), indicating that the fluorescent compounds are stable and cannot be damaged during the degradation process. Such a claim was also corroborated by subsequent *in vivo* tests.

### 2.3.7 *In vivo* biodegradability study and degradation/diffusion modeling of cross-linked BSA hydrogel.

Since *in vitro* biodegradability and biocompatibility studies showed promising results, *in vivo* experiments were carried out using mouse models. Nude mouse (no hair) is chosen in this study because it has no hair and is convenient to easily track the fluorescence image non-invasively.

The cross-linked BSA hydrogels were first subcutaneously injected into two 7-month old athymic Nude (nu/nu) mice using a modified indwelling needle assembly, [29] and the

corresponding fluorescence images at the injection site of the mice were *in-situ* tracked at different time points for 2 months using IVIS Lumina LT system and the corresponding results were presented in Figure 8, indicating that the cross-linked BSA hydrogel was completely digested *in vivo* in 2 months.

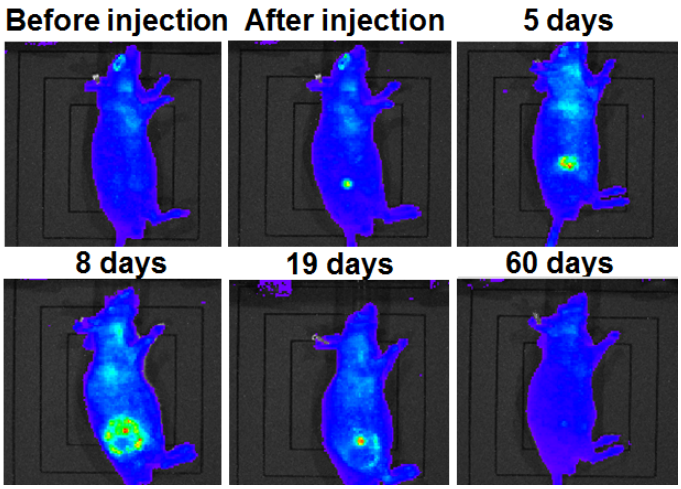


Figure 8. Fluorescence images of the 7-month old mouse with injected BSA hydrogel acquired at different time period.

Immediately after subcutaneous injection, strong fluorescence was also observed at the injection site when images were recorded at an emission of 595 nm with an excitation wavelength of 535 nm. Such non-invasive real-time fluorescence tracking allowed for the observation of the fluorescent BSA hydrogel's *in vivo* degradation process. A sequence of fluorescent images (Figure 8) shows the radiant fluorescence intensity corresponding to the transient distribution of the fluorophores released from the gel, which was subcutaneously injected. A strong and localized radiant fluorescence intensity was detected immediately after the injection, and the intensity decayed and the fluorescent area broadened. The fluorescence appears to be circularly symmetric with a few patchy spots within this region. The radiant fluorescence intensity remained detectable up to two months when the fluorophores were fully cleared from the injection site. The temporal correlation of the radiant fluorescence and the concentration of the

fluorophores can be established using the proposed physics-based model. In order to model the process, an axisymmetric, two-dimensional, and long-time Brownian diffusion of the fluorophores released from the injection point due to the degradation of autofluorescent hydrogel was assumed. The amount of injected hydrogel and the radiant fluorescent intensity were scaled by the maximum observable intensity for convenience. The fluorophore release was mimicked by a source term composed by a product of Weibull and complementary Heaviside functions. The Weibull function describes the growth and attenuation of the fluorescent signal from the hydrogel, while the complementary Heaviside step function determines the spatial domain of the gel. The source function can thus be expressed as

$$S(r,t) = S_1(t)\, f(r) = A\left[\frac{k}{\lambda}\left(\frac{t+T}{\lambda}\right)^{k-1} \cdot \exp\left(-\left(\frac{t+T}{\lambda}\right)^{k}\right)\right]\left[1.0 - H(r-R)\right], \qquad (1)$$

where $r$ is radial position, $t$ is time, $T$ is phase lag to match the initial condition, the constant $A$ adjusts the overall strength of the source, $k$ and $\lambda$ are the shape factor and scale parameter of the Weibull function, respectively, $R$ is the gel radius or the inner radius of injection needle, and $H$ is the Heaviside step function. The temporal ($S_1$) and spatial ($f$) contributions of the source term $S$ are shown in Figure 9. The Weibull function gives a flexible adjustment on the growth and decay of the radiant intensity due to the released fluorescent compound's diffusion, BSA hydrogel degradation, attenuation or absorption of the fluorophores, etc..

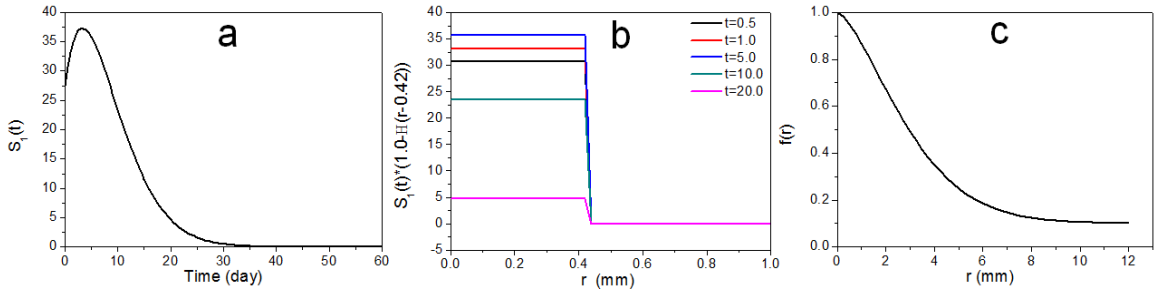

Figure 9**.** Empirical parameters applied to the mathematical model: (a) scaled strength $A$=500, shape factor $k$=1.5, scale parameter $\lambda$ = 10 day, and phase lag T = 1.5 day for the Weibull function, (b) source term $S(r,t)$, radius $R$ = 0.42 mm for a modified gauge-18 indwelling needle, (c) the fitted initial condition $c(r,0) = 0.1 + 0.8 \exp(-0.16r^{1.5})$.

Once the source term was determined, the transient species concentration correlated to the radiant intensity can be described by the diffusion equation:

$$\frac{\partial c(r,t)}{\partial t} = D\left(\frac{\partial^2 c}{\partial r^2} + \frac{1}{r}\frac{\partial c}{\partial r}\right) + S(r,t) \quad \text{for} \quad 0 \le r < \infty,\ t \ge 0, \tag{2}$$

where $D$ is an apparent constant diffusivity. We further assume that the initial condition can be formulated by an exponential function with an adjustable power (Figure 9 c):

$$c(r,0) = c_0 + c_1 \mathrm{e}^{-\alpha(r)} \quad \text{for} \quad 0 \le r < \infty, \tag{3}$$

where the constants $c_0$ and $c_1$ and the power function $\alpha(r)$ can be used to fit the observed initial radiant intensity. The corresponding boundary conditions are

$$\partial c / \partial r = 0 \quad \text{at} \quad r = 0; \quad c \to 0 \quad \text{as} \quad r \to \infty. \tag{4}$$

The above mathematical model has an analytical solution in an integral form, which can be derived by the Hankel transform of order zero, written as

$$\begin{aligned} c(r,t) = &\int_{\xi=0}^{\infty} \xi\, c(\xi,0) \left[\int_{\beta=0}^{\infty} \mathrm{e}^{-D\beta^2 t}\, \beta\, J_0(\beta r) J_0(\beta\xi)\, d\beta\right] d\xi \\ &+ \int_{\tau=0}^{t}\int_{\xi=0}^{\infty} \xi\, S(\xi,\tau) \left[\int_{\beta=0}^{\infty} \mathrm{e}^{-D\beta^2 (t-\tau)}\, \beta\, J_0(\beta r) J_0(\beta\xi)\, d\beta\right] d\xi\, d\tau \end{aligned}, \tag{5}$$

where $J_0$ is zeroth-order Bessel function, $\beta$ indicates continuous eigenvalues, and $\xi$ and $\tau$ are spatial and temporal dummy indices. The contributions of the initial condition and the source function are given by the first and second integrals. Figures 10a and 10b shows the comparison of experimental and theoretical results. The experimental data show characteristic diffusion time around 20 days, a diffusive length about 10 mm, and thus it is reasonable to assume the apparent

*in vivo* diffusivity as 4.32 $mm^2$/day, which is about 5% of the diffusivity of a small molecule in water (~$10^{-9}$ $m^2$/s). Several phenomenological parameters are involved in the initial condition and the source term that require further validation, however, apparent diffusivity *D* is the only empirical parameter in this physics-based model that simulates the transient release and redistribution of the fluorophores. Overall the calculated results are very consistent with the radiant fluorescence intensity observed (Figure 10). The time delay of the growth of the signal was due to the degradation of the hydrogel and the accompanying release of fluorescent compounds, and a further time shift of the peak values at various location is typical for a diffusive wave that propagates outward to a broader region. The calculation very well predicts the characteristic features of the underlying diffusive process. Quantitative consistency may be improved by further *in vitro* and *in vivo* experiments that can statistically validate the empirical parameters we have applied to this model.

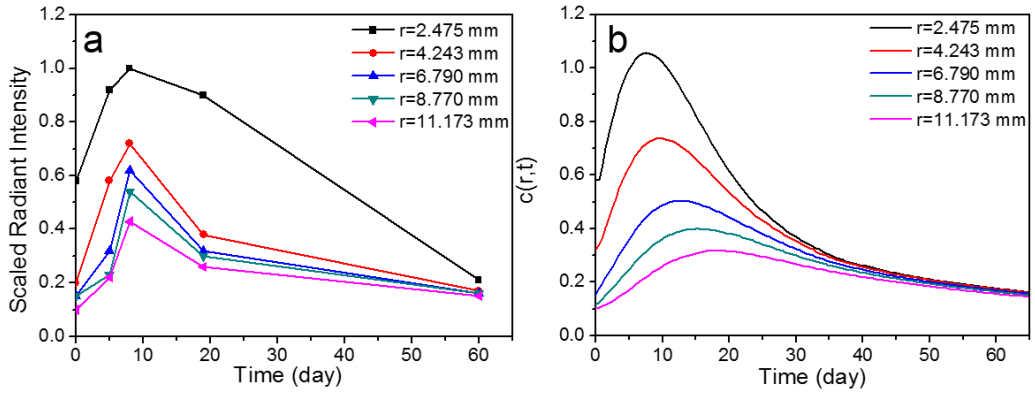


Figure 10**.** (a) Extracted radiant fluorescence intensity (doted points) versus time for five various locations at *r* = 2.475, 4.243, 6.790, 8.770, and 11.170 mm. (b) The calculated results on the transient distribution of apparent fluorophore concentration at the corresponding locations. The diffusivity *D* is approximately 4.32 $mm^2$/day.

As the age of mouse may also plays the role in the *in vivo* degradation of injected hydrogel as well as the removal of released fluorophores, similar experiment was carried out using a younger mouse (2-month old). As shown in Figure 11a, the younger mouse exhibits a similar degradation trend as the aged one, however, it is obvious that the degradation process is much faster than the

aged mice - From the third day post-injection, fluorescence intensity has begun to decline, and at the 27 days, the fluorescence signal disappears. Such difference can be attributed to the variance of metabolism efficiency in young and old mouse as expected. Figure 11b shows the fluorescence intensity change along with the degradation process, which initially increases and then diminishes. The histology study was also carried out for the young nude mouse with hydrogel injection and the corresponding result shows that all of tissues are normal and no inflammation appears, which is similar as the histology result of the old one discussed in the previous section.

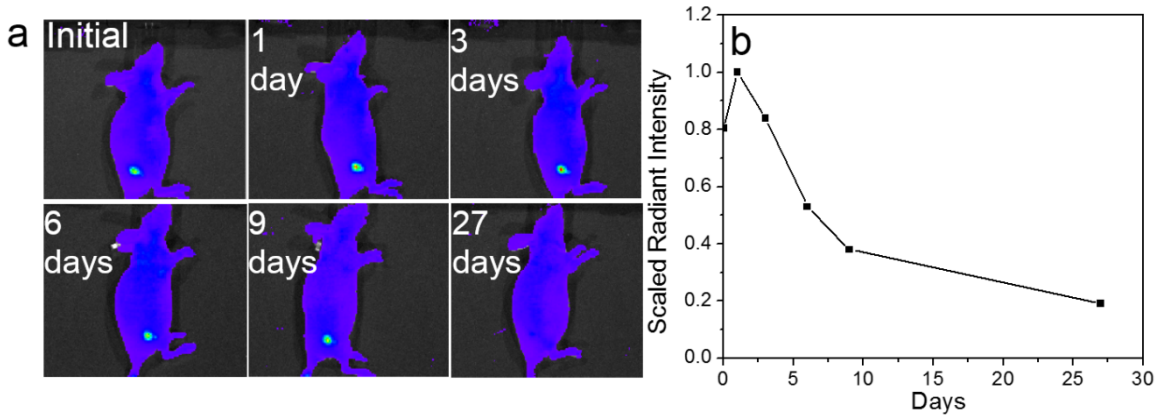


Figure 11**.** (a) Fluorescence images of the 2-month old mouse with injected BSA hydrogel acquired at different time period. (b) Extracted radiant fluorescence intensity (doted point) versus time.

These results implied that glutaraldehyde cross-linked protein hydrogel is a promising autofluorescent biodegradable material and can therefore serve as an excellent platform to investigate the *in vivo* degradation of biomaterials without using any fluorophore labels and to develop an appropriate mathematical model to understand and/or predict the degradation pattern of the implanted biomaterials.

### 2.3.8 *In vivo* biocompatibility study of cross-linked BSA hydrogel.

An *in vivo* biocompatibility study was also conducted. The tissues from mice were collected separately for histology analysis. For Mouse 271, the hydrogel was injected 20 days prior to

tissue collection and it was not fully degraded (the black arrow indicates the location of the BSA hydrogel residue in Figure 12b). In Figure 12, there was a mild hyperkeratosis on the surface of the epidermis that extended into a few hair follicles. A few hair follicles contained fragments of immature hair shafts. There was one focus of a few neutrophils with a few karyorrhectic nuclei and macrophages that had infiltrated into the subcutis. In the subcutaneous region, the injection area was surrounded by macrophages, some giant cells, and proliferating connective tissue infiltrated by a few neutrophils and eosinophils. The connective tissue was forming a capsule walling off the inflammation area. Up to 20 days, the autofluorescent BSA hydrogel was not fully digested and an inflammatory response was observed unsurprisingly due to the needle invasion, however, it could disappear after the hydrogel was fully digested, which was demonstrated in Mouse 267.

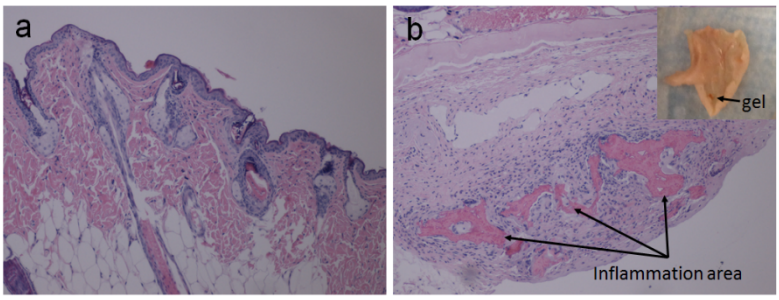


Figure 12**.** (a) skin tissue images in which hyperkeratosis was shown on the surface of epidermis(100×); (b) skin tissue focus on subcutaneous area. Inset shows the BSA hydrogel residue in th imjection site(40×) (20 days post injection).

Mouse 267, whose BSA hydrogel had been fully degraded in 2 months, was also subject to the histology study, as shown in Figure 13. For skin, there was a mild hyperkeratosis extending into a few hair follicles. Otherwise there were no significant lesions (Figure 13a). For pancreas, there is no significant lessions (Figure 13b). For liver, there were a few foci of accumulations of lymphocytes and plasma cells in portal areas surrounding bile ducts. Otherwise the liver had no significant lesions (Figure 13c). No significant lesions were observed in lymph nodes (Figure

13d). The tissues examined histologically were within normal limits in this mouse. This histology study further demonstrated *in vivo* biocompatibility of the as-developed autofluorescent BSA hydrogel.

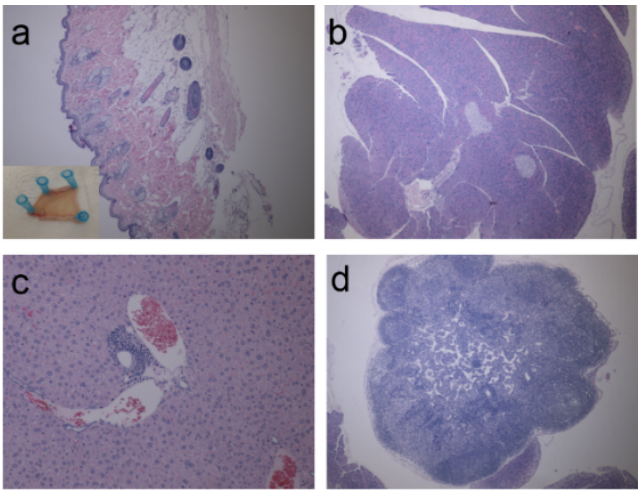


Figure 13**.** The histology study. (a) Skin tissue images (Inset shows the skin around the injection site) (40×); (b) Pancreas tissue image (40×); (c) Liver tissue images (100×); (d) Lymph node tissue images (40×).

## *2.4 Conclusion*

In our study, it has been demonstrated that glutaraldehyde cross-linked BSA hydrogel is highly biocompatible according to the *in vitro* cytotoxicity test and *in vivo* biocompatibility experiment. The BSA hydrogel exhibits strong green and red fluorescence *in vitro* and *in vivo* which can be excited over a wide range of wavelengths. According to the results from UV-vis and fluorescence spectra, it suggests that three classes of fluorescent compounds might be formed in BSA hydrogel after using GA as the cross-linker. In addition, the surface morphology of the BSA hydrogel exhibited a highly porous structure. The biodegradability and *in vivo* degradation of the BSA hydrogel was tracked and modeled without using any additional fluorophores, due to its unique autofluorescence, which broadens its suitability in a wide spectrum of biomedical applications. Since both the fluorescence of the cross-linked BSA hydrogel and the fluorescent compounds in the digested hydrogel solution are highly stable over months on the bench, the

identification of the newly formed fluorescent compounds in GA cross-linked BSA hydrogel became of particular interest. In this regard, LC-MS was further employed to analyze the proteinase K digested sample as trypsin could not fully digest the cross-linked BSA hydrogel. However, the LC-MS results (Figure S1) could not provide confirmative information due to the complexity and randomness of BSA cross-linking process with GA. Recently, there are few studies about autofluorescence generation in cell fixation and some peptides by glutaraldehyde [30] and autofluorescence of glutaraldehyde cross-linked chitosan nanoparticles [31]. The secondary amine and ethylenediamine in the molecule have been proposed to contribute to the fluorogenic mechanism. [30] Also, in glutaraldehyde solutions, α,β-unsaturated aldehyde polymer can be formed, which leads to the C=C double bond existed in the system, accompanied by the C=N double bonds from Schiff's base. Thus, it's highly possible that the fluorescence observed in the GA cross-linked BSA hydrogel are attributed to the electronic transitions such as π-π* transition of C=C bond and n-π* transition of C=N bond.[31] More complicatedly, the protein's secondary and/or tertiary structure may also have significant influence on the synthesis of the fluorescent compounds and the fluorescence observed might be attributed to the synergistic effect of several amino acids in close proximity, for example, similar to other green or red fluorescent proteins. Moreover, the charge surrounding the flurophores in BSA hydrogel is another potential factor to affect the fluorescence. More efforts are required in order to identify the chemical structure of such stable fluorescent compounds and thus create them using organic synthesis for other potential applications.

As the fluorescence technology represents one of the most promising non-invasive approaches to monitor physiological parameter changes and to track the *in vivo* degradation of biomaterials, the newly synthesized autofluorescent BSA hydrogel with high biocompatibility and

biodegradability exhibits high value in a variety of biomedical applications ranging from biosensing to drug delivery and tissue engineering. As for the *in vivo* biodegradation modeling, the fluorescence intensity first enhanced and then decayed along the time. Such observation might be explained as follows: the autofluorescence of the concentrated BSA hydrogel is initially self-quenched to certain degree due to the fact that the excitation photons are limited in a small area, and as it degrades, the fluorophores diffuse out along the time. Consequently, the increase of the fluorescence intensity was observed. The released fluorophores have the chance to diffuse out and reach other areas instead of immediate clearance by the immune response, which may be attributed to the lack of functional T-cell in nude mice. Over a course of couples of weeks, the released fluorophores gradually disappeared through circulation system. More studies are required in order to prove the biological meaning of the developed mathematical model.

This facile strategy to prepare unique autofluorescent BSA hydrogels will open a new venue to prepare novel biocompatible and biodegradable fluorescent protein hydrogels, which could significantly expand the scope of protein hydrogel in biomedical applications.

**Reference**


1. Shen, W., Lammertink, R. G., Sakata, J. K., Kornfield, J. A. and Tirrell, D. A. (2005) Assembly of an artificial protein hydrogel through leucine zipper aggregation and disulfide bond formation. Macromolecules, **38,** 3909-3916.
2. Peppas, N. A., Hilt, J. Z., Khademhosseini, A. and Langer, R. (2006) Hydrogels in biology and medicine: from molecular principles to bionanotechnology. ADVANCED MATERIALS-DEERFIELD BEACH THEN WEINHEIM-, **18,** 1345.
3. Drury, J. L. and Mooney, D. J. (2003) Hydrogels for tissue engineering: scaffold design variables and applications. Biomaterials, **24,** 4337-4351.
4. Lee, K. Y. and Mooney, D. J. (2001) Hydrogels for tissue engineering. Chemical reviews, **101,** 1869-1880.
5. Park, J. H. and Bae, Y. H. (2002) Hydrogels based on poly (ethylene oxide) and poly (tetramethylene oxide) or poly (dimethyl siloxane): synthesis, characterization, in vitro protein adsorption and platelet adhesion. Biomaterials, **23,** 1797-1808.
6. Graiver, D., Durall, R. and Okada, T. (1993) Surface morphology and friction coefficient of various types of Foley catheter. Biomaterials, **14,** 465-469.
7. Risbud, M. V. and Bhonde, R. R. (2000) Polyacrylamide-chitosan hydrogels: in vitro biocompatibility and sustained antibiotic release studies. Drug Delivery, **7,** 69-75.

8. Censi, R., Di Martino, P., Vermonden, T. and Hennink, W. E. (2012) Hydrogels for protein delivery in tissue engineering. Journal of Controlled Release, **161,** 680-692.
9. Sun, X., Ma, X., Kumar, C. V. and Lei, Y. (2014) Protein-based sensitive, selective and rapid fluorescence detection of picric acid in aqueous media. Analytical Methods, **6,** 8464-8468.
10. Matsushita, S., Isima, Y., Chuang, V. T. G., Watanabe, H., Tanase, S., Maruyama, T. and Otagiri, M. (2004) Functional analysis of recombinant human serum albumin domains for pharmaceutical applications. Pharmaceutical research, **21,** 1924-1932.
11. Migneault, I., Dartiguenave, C., Bertrand, M. J. and Waldron, K. C. (2004) Glutaraldehyde: behavior in aqueous solution, reaction with proteins, and application to enzyme crosslinking. Biotechniques, **37,** 790-806.
12. Nimni, M. E., Cheung, D., Strates, B., Kodama, M. and Sheikh, K. (1987) Chemically modified collagen: a natural biomaterial for tissue replacement. Journal of Biomedical Materials Research, **21,** 741-771.
13. Habeeb, A. and Hiramoto, R. (1968) Reaction of proteins with glutaraldehyde. Archives of biochemistry and biophysics, **126,** 16-26.
14. Jun, J. Y., Nguyen, H. H., Chun, H. S., Kang, B.-C. and Ko, S. (2011) Preparation of size-controlled bovine serum albumin (BSA) nanoparticles by a modified desolvation method. Food Chemistry, **127,** 1892-1898.
15. Artzi, N., Oliva, N., Puron, C., Shitreet, S., Artzi, S., Bon Ramos, A., Groothuis, A., Sahagian, G. and Edelman, E. R. (2011) In vivo and in vitro tracking of erosion in biodegradable materials using non-invasive fluorescence imaging. Nature materials, **10**.
16. Wang, W., Liu, J., Li, C., Zhang, J., Liu, J., Dong, A. and Kong, D. (2014) Real-time and non-invasive fluorescence tracking of in vivo degradation of the thermosensitive PEGlyated polyester hydrogel. Journal of Materials Chemistry B, **2,** 4185-4192.
17. Heo, Y. J., Shibata, H., Okitsu, T., Kawanishi, T. and Takeuchi, S. (2011) Long-term in vivo glucose monitoring using fluorescent hydrogel fibers. Proceedings of the National Academy of Sciences, **108,** 13399-13403.
18. Suri, J. T., Cordes, D. B., Cappuccio, F. E., Wessling, R. A. and Singaram, B. (2003) Continuous Glucose Sensing with a Fluorescent Thin- Film Hydrogel. Angewandte Chemie International Edition, **42,** 5857-5859.
19. HyeanáKim, B. (2006) An insulin-sensing sugar-based fluorescent hydrogel. Chemical communications**,** 1842-1844.
20. Gong, Y., Gao, M., Wang, D. and Möhwald, H. (2005) Incorporating fluorescent CdTe nanocrystals into a hydrogel via hydrogen bonding: toward fluorescent microspheres with temperature-responsive properties. Chemistry of materials, **17,** 2648-2653.
21. Wu, Y., Wang, L., Guo, B. and Ma, P. X. (2014) Injectable biodegradable hydrogels and microgels based on methacrylated poly (ethylene glycol)-co-poly (glycerol sebacate) multi-block copolymers: synthesis, characterization, and cell encapsulation. Journal of Materials Chemistry B, **2,** 3674-3685.
22. Lad, M. D., Birembaut, F., Matthew, J. M., Frazier, R. A. and Green, R. J. (2006) The adsorbed conformation of globular proteins at the air/water interface. Physical Chemistry Chemical Physics, **8,** 2179-2186.
23. Subia, B. and Kundu, S. (2013) Drug loading and release on tumor cells using silk fibroin–albumin nanoparticles as carriers. Nanotechnology, **24,** 035103.
24. Svensson, A., Nicklasson, E., Harrah, T., Panilaitis, B., Kaplan, D., Brittberg, M. and Gatenholm, P. (2005) Bacterial cellulose as a potential scaffold for tissue engineering of cartilage. Biomaterials, **26,** 419-431.
25. Dai, X., Zhang, Y., Gao, L., Bai, T., Wang, W., Cui, Y. and Liu, W. (2015) A Mechanically Strong, Highly Stable, Thermoplastic, and Self- Healable Supramolecular Polymer Hydrogel. Advanced Materials.

26. Sun, J.-Y., Zhao, X., Illeperuma, W. R., Chaudhuri, O., Oh, K. H., Mooney, D. J., Vlassak, J. J. and Suo, Z. (2012) Highly stretchable and tough hydrogels. Nature, **489,** 133-136.
27. Shin, H., Temenoff, J. S. and Mikos, A. G. (2003) In vitro cytotoxicity of unsaturated oligo [poly (ethylene glycol) fumarate] macromers and their cross-linked hydrogels. Biomacromolecules, **4,** 552-560.
28. Zhao, C., Zhuang, X., He, P., Xiao, C., He, C., Sun, J., Chen, X. and Jing, X. (2009) Synthesis of biodegradable thermo-and pH-responsive hydrogels for controlled drug release. Polymer, **50,** 4308-4316.
29. Shibata, H., Heo, Y. J., Okitsu, T., Matsunaga, Y., Kawanishi, T. and Takeuchi, S. (2010) Injectable hydrogel microbeads for fluorescence-based in vivo continuous glucose monitoring. Proceedings of the National Academy of Sciences, **107,** 17894-17898.
30. Lee, K., Choi, S., Yang, C., Wu, H.-C. and Yu, J. (2013) Autofluorescence generation and elimination: a lesson from glutaraldehyde. Chemical Communications, **49,** 3028-3030.
31. Wei, W., Wang, L.-Y., Yuan, L., Wei, Q., Yang, X.-D., Su, Z.-G. and Ma, G.-H. (2007) Preparation and application of novel microspheres possessing autofluorescent properties. Advanced Functional Materials, **17,** 3153.

## *Supplement Materials*

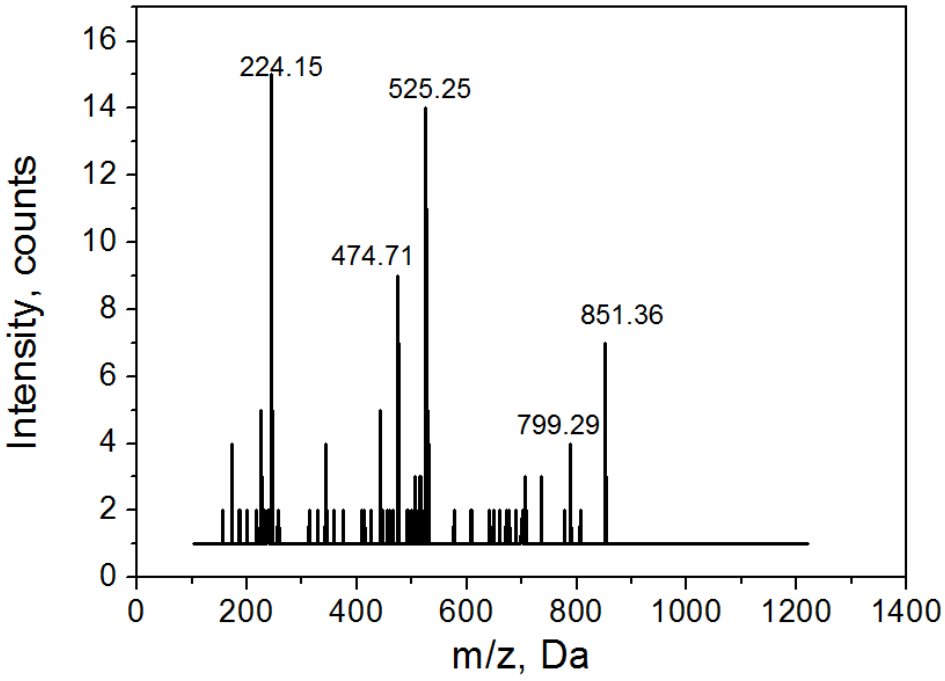


Figure S1: LC-MS result for GA cross-linked BSA hydrogel digested by Proteinase K.

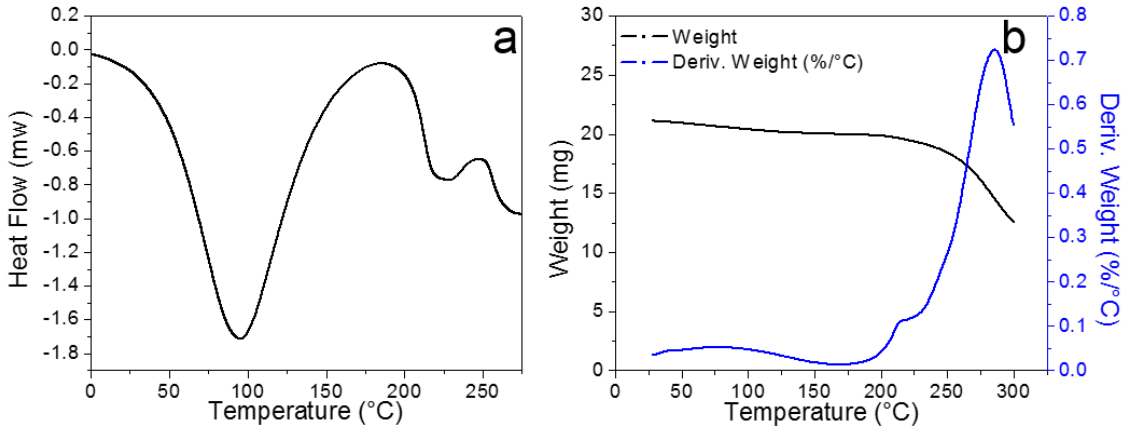


Figure S2: Thermal stability results. (a) DSC thermogram of the cross-linked BSA hydrogel; (b) TGA result of the cross-linked BSA hydrogel

Differential Scanning Calorimetry (DSC) and Thermogravimetric Analysis (TGA) techniques were employed to study the thermal properties of the cross-linked BSA hydrogel. Unlike BSA particle whose melting point is ~68 °C, the DSC data of the as-prepared cross-linked BSA hydrogel shows a big peak centered at ~95 °C (Fig. S2a), which can be attributed to the fact that chemical crosslinking of BSA increases the melting point of the hydrogel. TGA study indicates that the as-prepared hydrogel starts to decompose from ~180 °C (Fig. S2b).

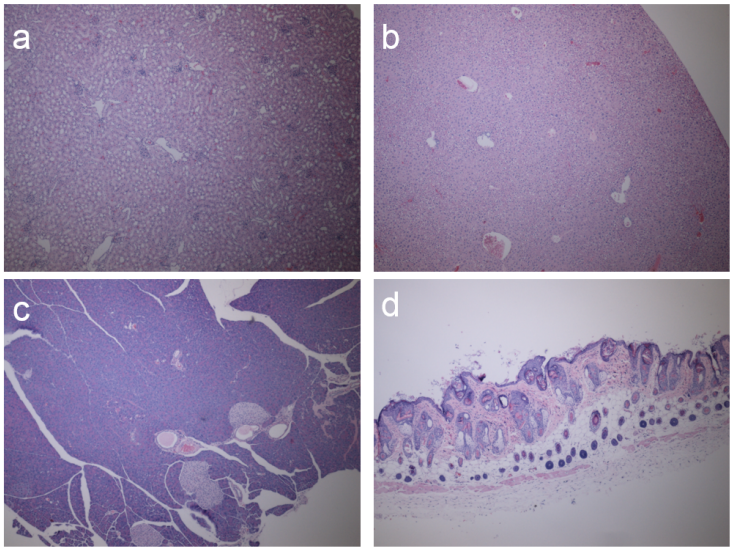


Figure S3| Histology study. (a) Kidney tissue images (40×); (b) Liver tissue image (40×); (c) Pancreas tissue image (40×); (d) Skin tissue image (40×).

# Chapter 3

## Novel Green and Red Autofluorescent Protein Nanoparticles for Cell Imaging and *in vivo* Biodegradation Imaging and Modeling

**Abstract**

Albumins are widely used in bioengineering due to their low-cost, good biocompatibility, and biodegradability. Herein we report that glutaraldehyde cross-linked bovine serum albumin (BSA) forms a suspension of novel fluorescent nanoparticles with an average size of ~40 nm, exhibiting strong green/red autofluorescence. UV-vis spectra, in conjunction with fluorescence emission spectra, suggest that three classes of fluorescent compounds presumably formed. The size distribution and surface morphology of the autofluorescent BSA nanoparticles were characterized using various advanced techniques. The application of the autofluorescent BSA nanoparticles was first demonstrated for cell bio-imaging using 293FT human kidney cell line. Its good biocompatibility and low cytotoxicity were further validated by *in vitro* cytotoxicity assay and *in vivo* histological study. The strong red autofluorescence of the BSA nanoparticles was further exploited in the realization of convenient and non-invasive tracking/modeling of its *in vivo* degradation based on real-time fluorescence imaging. A mathematical model is proposed and in good agreement with the experimental results. This study indicates that the as-prepared functional, biocompatible and biodegradable autofluorescent protein nanoparticles are suitable for a range of biomedical applications.

## *3.1 Introduction*

Nanomaterials, standing in the leading edge of nanotechnology, have been attracting strong interest in many biomedical applications ranging from drug delivery, [1] biosensing,[2] to bioimaging[3] due to their superior size-dependent properties.[4] To probe various fundamental processes related to life sciences (e.g., *in vitro* and *in vivo* reactions), it typically requires direct tools with high sensitivity and accuracy to monitor or image. Photoluminescence or fluorescence techniques have been explored as one of the most suitable and popular methods for these purposes. [5, 6] Moreover, fluorescence based detection is one of the highly sensitive and selective sensing technologies.[4] As a result, various nanoparticles conjugated with a range of fluorescent dyes have resulted in a group of novel functional materials known as fluorescent nanoparticles. Up to date, many functional nanomaterials including quantum dots,[7] noble metal nanoparticles,[8] and silicon nanomaterials[9] have been extensively reported and used in various fields such as cell imaging, *in vivo* imaging and biosensing.[10, 11] However, they are either toxic or possess poor biocompatibility and biodegradability, and thus are not suitable for biomedical applications directly. To overcome those limitations, the strategies such as using biocompatible surface coating or modifications have been widely employed to address the toxicity and biocompatibility issues, but only partial success has been achieved. Therefore, there is an urgent need to develop novel function nanomaterials with good biocompatibility and biodegradability, low intrinsic toxicity as well as the capability of emitting fluorescence at proper wavelength window, suitable for a wide spectrum of biomedical applications. In this regard, protein nanoparticles have stood out as an excellent candidate. In the past decade, protein-based nanoparticles have been widely synthesized through various methods such as spray-drying, [12] desolvation[13] and emulsification,[14] and then labeled with a range of fluorophores to

overcome the aforementioned limitations faced by other inorganic/organic nanoparticles. However, to synthesize those fluorescent protein-based nanoparticles, fluorophores are either chemically or physically immobilized in the protein nanoparticles matrix, which highly restricts their applicability due to the complex synthetic routes, potential leakage and photobleaching of the fluorophores, as well as the biocompatibility/biodegradability of fluorescent labels and their potential influence on the degradation pattern. Hence, developing autofluorescent protein nanoparticles with desirable excitation/emission wavelength are urgently demanded.

It is well known that autofluorescence is generated during tissue and cell fixation using glutaraldehyde (GA). Glutaraldehyde, a linear 5-carbon dialdehyde with a formula of $CH_2(CH_2CHO)_2$, is a widely used cross-linker, exhibiting apparent, colorless, pungent properties, as well as soluble in all proportions in water and alcohol and in organic solvents.[15] The advantages of GA include its low cost and high reactivity and efficiency to react with the amine groups to generate thermal and chemical stable cross-linkages compared with other aldehydes.[16] Besides, GA can also react with several other functional groups in protein, such as thiol, imidazole, etc., but most reactive group is lysine residues (ϵ-amino groups).[15] Recently, it has been reported that some well-designed polypeptides, after GA crosslinking, could become autofluorescence, and the secondary amine and ethylenediamine in the molecule were responsible for the generation of fluorescence.[17] Moreover, GA cross-linked chitosan can also form autofluorescent nanoparticles, whose fluorescence is presumably attributed to the electronic transitions such as π-π* transition of C=C bond and n-π* transition of C=N bond.[18] These observations motivate us to explore the feasibility of generating autofluorecent BSA nanoparticles through a simple GA cross-linking process, since BSA possesses all necessary structures/bonds favorable for electronic transitions such as π-π* and n-π* transition. Both

bovine serum albumin (BSA) and human serum albumin (HSA) exhibit intrinsic autofluorescence (excitation/emission at 279 nm/348 nm), ascribing to the two tryptophan residues. However, such short excitation and emission wavelength substantially restrict any *in vivo* biomedical applications based on its intrinsic fluorescence. Therefore, the synthesis of autofluorescent BSA nanoparticles with a longer excitation/emission wavelength is highly demanded, but remains an unmet challenge.

Besides the fluorescence functionality, the size of nanoparticles is another predominant factor governing their applications in biological systems. [19] Particles smaller than 10 nm can be easily cleared by kidney, [20] and up to 30 nm is subjected to a nucleus uptake. Also, particles with size ranging from 100 to 200 nm can be entrapped by lymph nodes, [21] while particles larger than 200 nm would be accumulated in the spleens or taken up by phagocytic cells. In general, particles with size smaller than 100 nm are suitable for cell uptake and imaging, as well as for drug delivery.

In this research, BSA nanoparticles have been synthesized and well characterized. Their biomedical applications have also been firstly demonstrated. All these features corroborate that the functional, biocompatible, and biodegradable autofluorescent protein nanoparticles synthesized through the developed facile strategy could open a door for a broad spectrum of biomedical applications.

## *3.2 Experimental*

### 3.2.1 Materials

Bovine serum albumin, glutaraldehyde, and hemin were purchased from Sigma. $KH_2PO_4$, $Na_2HPO_4$, and NaCl were acquired from Fisher Scientific to prepare of 10 mM pH 7.4 PBS buffer saline. Dulbecco's Modified Eagle Medium (DMEM), CCK-8, and Fetal Bovine Serum (FBS) were purchased from Gibco. Membrane Matrix were purchased from Corning Matrigel (50-fold dilution using DMEM to generate 1×matrigel). Dialysis membrane was purchased from Spectrum Labs. 293 FT and A549 cell lines were purchased from Thermo Fisher Scientific and Sigma, respectively. Athymic nude mice (2 months old) were purchased from Harlan Sprague Dawley Inc.

### 3.2.2 Fabrication of BSA autofluorescent nanoparticles

150 mg/L BSA solution in 10 mM pH 7.4 PBS buffer saline was prepared first as stock solution. The glutaraldehyde/n-butanol dispersion solution was prepared as follows: 50% glutaraldehyde was diluted ten-fold using 10 mM pH 7.4 PBS buffer and then mixed with n-butanol at a volume ratio of 19 to 1. Then 1 mL 150 mg/mL BSA solution was added dropwise, in about 8 minutes, into 20 mL glutaraldehyde/n-butanol dispersion solution under high dispersing speed using IKA Disperser and thus resulted in the formation of BSA nanoparticles suspension. The as-prepared BSA nanoparticle suspension was then stored in the refrigerator at 4 °C overnight. Before any biomedical applications, a dialysis membrane with a cutoff molecular weight of 20 KDa was employed to remove any glutaraldehyde residue. Briefly, 6 mL BSA nanoparticle suspension was loaded in the dialysis membrane tube and then dialyzed against 2 L 10 mM pH 7.4 PBS buffer under magnetic stirring. The PBS buffer was replaced several times to ensure the removal of

glutaraldehyde. Subsequently, dialyzed BSA autofluorescent nanoparticle suspension was subject to sterilization at 121□ for 20 minutes. The final BSA nanoparticles exhibiting both green and red fluorescence properties are ready for use.

### 3.2.3 Characterization

In the UV-visible spectra study, BSA nanoparticle suspension was loaded in a 3 mL quartz cuvette. The UV-vis spectra were collected using a Varian Cary 50 Scan UV-visible Spectrophotometer. 10 mM pH 7.4 PBS buffer was used as control. To study the photophysical properties, the emission fluorescence spectra of BSA nanoparticle suspension were measured using Varian Cary Eclipse Fluorescence Spectrophotometer under different excitation wavelengths.

BSA nanoparticle suspension before dialysis was employed to investigate the size distribution using Dynamic Light Scattering (DLS) at a fixed angle of 90 degree at room temperature. Surface morphology of the prepared nanoparticles was studied using JEOL 6335 Field Emission Scanning Electron Microscopy (FESEM) operating at an accelerating voltage of 10 KV and 12 μA. Pure DI water was used for dialysis to remove the salt in the SEM sample preparation. Prior to imaging, samples were sonicated, loaded, and fixed on a stub using a double-sided carbon tape for drying. Further, the samples were sputtered coated with Au/Pd alloy for 45 s in vacuum at a current intensity of 10 mA for a better contrast.

### 3.2.4 Cell imaging

293 FT human kidney cells were seeded at the density of ~20,000 cells per well on a 24-well plate coated with 1×matrigel, cultured in 37 °C incubator overnight with D 10 media (DMEM containing 10% FBS). Then, cells were transferred into the 8-well chamber coated with 1×matrigel and waited 3 hours until the cells were adhered to the bottom. After that, the medium

was removed and the adherent cells were washed twice with fresh DMEM. The BSA nanoparticle suspension diluting with FBS-free DMEM at a final concentration of 2.5 mg/mL was added to the chamber, while a well without any BSA nanoparticle suspension was used as control. After 4 hours of incubation at 37 °C, the cells were washed several times with DMEM and then fresh DMEM was added into the chamber. The cells in the 8-wells chamber were subsequently imaged using Nikon A1R Spectral Confocal Microscope. The fluorescence signals from the autofluorescent BSA nanoparticles were collected upon excitation at 488 and 560 nm, with acquiring filter at 510 and 615 nm, respectively. After selecting the height ranges to focus on the cells, Z-stacking function was performed and three height locations were captured to demonstrate the uptake of BSA nanoparticles by the cells.

### 3.2.5 Cytotoxicity of BSA nanoparticles

CCK-8 assay was employed to evaluate the cytotoxicity of the BSA nanoparticles against A549 cancer cells. Briefly, A549 cells were seeded in 96-well plates at a density of 5000 cells per well and incubated at 37 °C overnight. Then, the cells were exposed to 0, 0.3, 0.6, 1.25, and 2.5 mg/ml nanoparticle suspension diluted by FBS-free DMEM (5 wells for each samples) and one column was kept with only FBS-free DMEM as the blank. After 24 hours culture in the 37 °C incubator, the samples were removed, washed several times, and replaced with fresh medium (100 μL per well). Finally, 10 μL of CCK-8 solution was loaded to each well and the absorption at 450 nm on a microplate reader was recorded after 1 hour incubation. The cell viability percentage was calculated based on the following equation:

Cell survival $\%=(A_{sample}-A_{blank})/(A_0-A_{blank})\times 100\%$

### 3.2.6 *In vivo* time-dependent imaging, biodegradation and biocompatibility test

All studies were conformed to the University of Connecticut (UConn) Institutional Animal Care and Use Committee approved protocol and the methods were carried out in accordance with the approved guidelines. Each of the three Athymic nude mice was subcutaneously injected 100 μL BSA nanoparticles suspension at a concentration of 3.75 mg/mL using a gauge 27 needle after the mice were anesthetized using isoflurane and cleaned by alcohol swab at the injection spot. The time-dependent image was non-invasively captured using an IVIS Lumina LT system with a central wavelength of 535 nm as the excitation source and acquiring emission central wavelength at 595 nm. After the BSA nanoparticles were fully degraded, they were sacrificed for histological analysis.

## *3.3 Results and Discussion*

BSA exhibits intrinsic autofluorescence (excitation/emission at 279 nm/348 nm), ascribing to the two tryptophan residues. However, nanoparticles formed by GA cross-linked albumin (BSA or HSA) and sterilized at 121 °C for 20 min exhibit unique green and red autofluorescence, which can be excited in a wide range of wavelength. Autofluorescent BSA nanoparticles were synthesized by a simple procedure outlined in Figure 1. Droplets of BSA solution were first added into glutaraldehyde/n-butanol aqueous solution under high-speed dispersion to form nanoparticles. According to our observation, the as-prepared BSA nanoparticles at this stage only showed strong green fluorescence but insignificant red fluorescence (Figure S1). Surprisingly, after the as-prepared BSA nanoparticles were autoclaved for sterilization, the green fluorescence was enhanced, accompanying with the appearance of the red fluorescence (Figure 1). As shown, the as-prepared BSA nanoparticles possess strong green and red fluorescence when different optical filters ($E_x/E_m$=470/530 nm and $E_x/E_m$ =595/630 nm) were used to acquire their fluorescent images, indicating the formation of a new class of autofluorescent protein

nanoparticles. Such unique property of BSA nanoparticles could have a wide spectrum of biomedical applications, thus leading us to further investigate the photophysical and biological properties of this new class of protein nanoparticles. . As a control, the same procedure (dispersion followed by autoclave) was repeated without using GA cross-linker, only big pieces of denatured BSA aggregation were produced which did not possess such autofluorescence (Figure. S2), indicating the important roles of GA crosslinking and autoclave in the preparation of the unique green and red autofluorescent BSA nanoparticles.

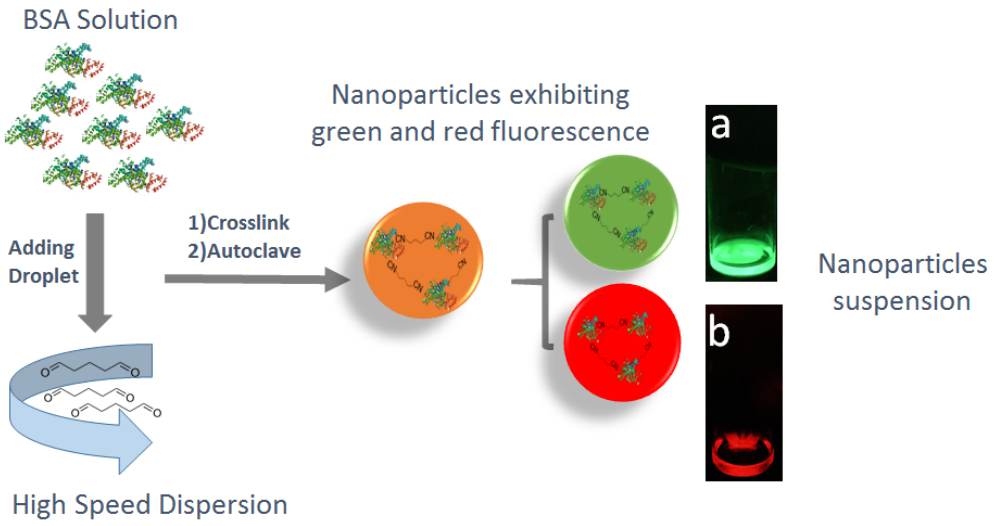


Figure 1. Scheme of the synthetic route for autofluorescent BSA nanoparticles and the corresponding green and red autofluorescence images.

### 3.3.1 Characterization of the BSA nanoparticle suspension

UV-visible spectroscopy was further carried out for initial composition analysis. Pristine BSA solution is well-known to have an absorption peak at 279 nm (data not shown). To investigate the newly formed fluorophores, UV-visible spectrum was first obtained for the sample and the corresponding results were presented in Figure 2a. The black trace is the scan of the PBS buffer

between 350 nm and 650 nm as a control, while the red trace is the scan of BSA nanoparticle suspension. The inset of Figure 2a shows an enlarged region for the UV-vis spectrum (500~650 nm) of BSA nanoparticles. Unlike the UV-vis spectrum of pristine BSA solution (data not shown), there are three obvious broad shoulder peaks in the spectrum of BSA nanoparticles, which center at ~450 nm, 540 nm, and 580 nm, respectively, and a small shoulder peak at 400 nm. In conjunction with the fluorescence images obtained in Figure 1, these results suggest that there may be new fluorescent components formed during the fabrication process, and thus a systematical investigation on the fluorescence properties of autofluorescent BSA nanoparticles was conducted.

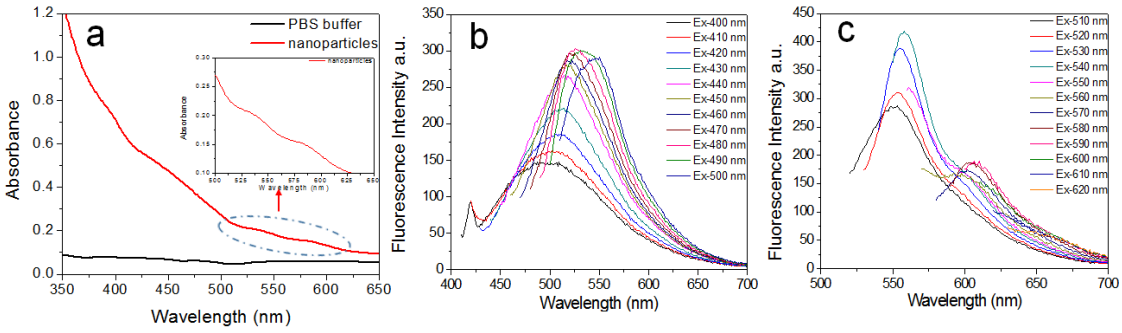


Figure 2**.** a) UV-visible spectra of the as-prepared BSA nanoparticle suspension and the PBS buffer (control), respectively. Inset shows the enlarged UV-vis spectrum of BSA nanoparticle suspension in the range of 500 to 650 nm; b) and c) Fluorescence emission scans of the as-prepared BSA nanoparticle suspension at the excitation wavelength ranging from 400 to 620 nm.

According to the results suggested by UV-visible spectra, fluorescence emission spectra of the as-synthesized BSA nanoparticle suspension were recorded in the range of 10 nm longer than excitation wavelength to 700 nm and shown in Figure 2b and c, which consists of totally 23 individual emission spectra with 10 nm increment of excitation from 400 to 620 nm. A prominent emission peak in the green fluorescence wavelength range was observed when it was excited at a wavelength between 400-540 nm, accompanying with the peak shifts slightly from

500 nm to 560 nm. While excited at a wavelength between 550 nm and 590 nm, a broad emission peak centered at ~602 nm shows up and accounts for the observed red fluorescence of BSA nanoparticles. According to Figure 2b and c, it is obvious that the proper excitation wavelengths for green, yellow, and red fluorescence are around 480 nm, 530 nm and 580 nm, respectively, in good agreement with the conclusion drawn from the UV-visible spectra of the as-prepared BSA nanoparticles. The fluorescence spectra of BSA nanoparticles are also consistent with the strong green and red fluorescent images observed in Figure 1. Fluorescence imaging, UV-visible spectra, and Fluorescence spectra have demonstrated that new fluorophores (green, red) are formed in the fabrication process. However, it is very challenging to determine the structure of the newly formed fluorophores because the BSA nanoparticles are cross-linked by GA and the cross-linking points in BSA are random and not controllable, as well as the possible condensation reaction resulted during the autoclave process. The potential contributors for the observed fluorescence can be referred to literature report, [17] in which precisely controlled reaction condition was adapted. It is generally believed that the amine groups in the molecule could contribute to the fluorogenic mechanism. Especially in this reference, Histone, rich in lysine and arginine, yields green emitter in neutral solution. When it is existed as polypeptide, yellow and red emitter shows up. BSA protein is a more complicated “polypeptide” in 3D configuration, thus it is highly possible that the similar mechanism is applicable to our case. However, in this reference paper, the accurate structure responsible for the fluorescence is still unknown, even just using very simple polypeptide and under well-controlled reaction conditions. In our case, BSA protein possesses much more complicated 3-D structure, and thus the accurate structure of formed fluorophores could not be easily resolved. Moreover, GA cross-linked chitosan has also been reported to form autofluorescent chitosan nanoparticles, whose

fluorescence is presumably attributed to the electronic transitions such as π-π* transition of C=C bond and n-π* transition of C=N bond, [18] which might also be applicable to our case. GA-crosslinking of BSA could results in new C=N bond formation, thus synergizing with the C=C bonds from tryptophan, tyrosine, phenylalanine and histidine in BSA to realize necessary electronic transitions. In addition, autoclave for sterilization at an elevated temperature could result in condensation reaction between carboxylic group and amine group in BSA nanoparticles to form C=N bond (n-π* transition), which could also potentially attributed to the observed enhanced green fluorescence and the appearance of red fluorescence. Although the actual structures of the newly formed fluorophores could not be resolved in this study, the as-prepared autofluorescent BSA nanoparticles possesses excellent multi-functionality and its wide biomedical applications in cell imaging, *in vivo* tracking/modeling and biosensing will be demonstrated in subsequent sections.

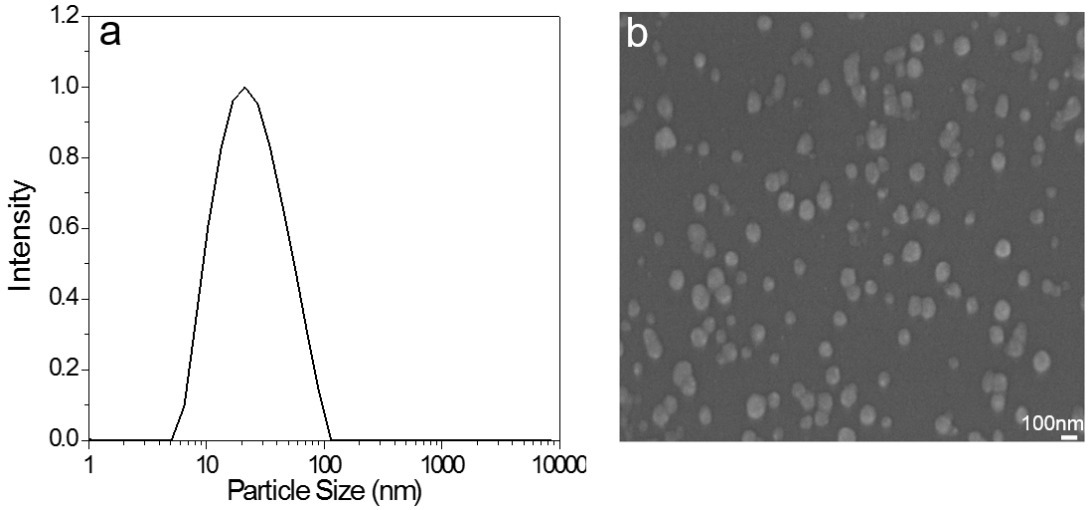


Figure 3. a) The DLS analysis of the autofluorescent BSA nanoparticles; and b) A representative SEM image of the autofluorescent BSA nanoparticles after dialysis to remove the salts (scale bar = 100 nm). It is observed that some particles are relatively unstable in water sample (after dialysis) compared with in PBS buffer and thus have aggregated, unavoidably resulting in a larger size of BSA nanoparticles observed under the SEM image.

To investigate the size distribution and surface morphology of the BSA nanoparticles, both DLS and SEM characterization were carried out (Figure 3). DLS data (Figure 3a) show the size distribution of the BSA nanoparticles in PBS buffer solution, indicating an average size of ~40 nm and a broad size distribution with polydispersity index (PDI) of ~0.2. Figure 3b shows a typical SEM image of the BSA nanoparticles, indicating that the as-prepared particles roughly have a spherical shape. When preparing the sample for SEM, BSA nanoparticles suspended in PBS buffer was first dialyzed against pure DI water to remove any salt. It is observed that some particles are relatively unstable in water sample compared with in PBS buffer and thus have aggregated, avoidably resulting in a slightly larger size under the SEM image. Details of the preparation for SEM sample were described in the Experimental Section.

Nanoparticles with an average diameter of tens of nanometers have been reported to possess good ability of penetration into cells. [22] Autofluorescent BSA nanoparticles with an average size around 40 nm serve as nano-carrier matrix in following *in vitro* and *in vivo* imaging experiments, which may have numerous potential applications. Therefore, the applications of the as-prepared BSA nanoparticles are demonstrated in cell imaging and *in vivo* imaging/modeling, respectively.

### 3.3.2 Cellular imaging study using the autofluorescent BSA nanoparticles

Cellular imaging based on autofluorescent BSA nanoparticles was conducted by confocal fluorescence microscopy. 293FT human kidney cells attached on the bottom of the well were used as the targets. After incubation with 2.5 mg/mL the as-prepared autofluorescnet BSA nanoparticle suspension at 37 ℃ for 4 hr, DMEM medium was used to wash away the remaining nanoparticles untaken by the cells. Since the BSA nanoparticles exhibited both green and red fluorescence, the target cells were imaged by the confocal with excitation wavelength at ~488

and ~560 nm, respectively, and the fluorescence signals were collected at GFP wavelength (~510 nm) and Texas Red wavelength (~615 nm), respectively. Figure 4a-c shows the merged cell image (Figure 4a) by overlaying transmission light image with the confocal green (Figure 4b) and red fluorescence (Figure 4c) images, respectively, from which one can see intense but non-uniform green and red fluorescent signal in the cytoplasm of the cells. As a control, the optical and fluorescence images of cells without BSA nanoparticles were presented in Figure S3.

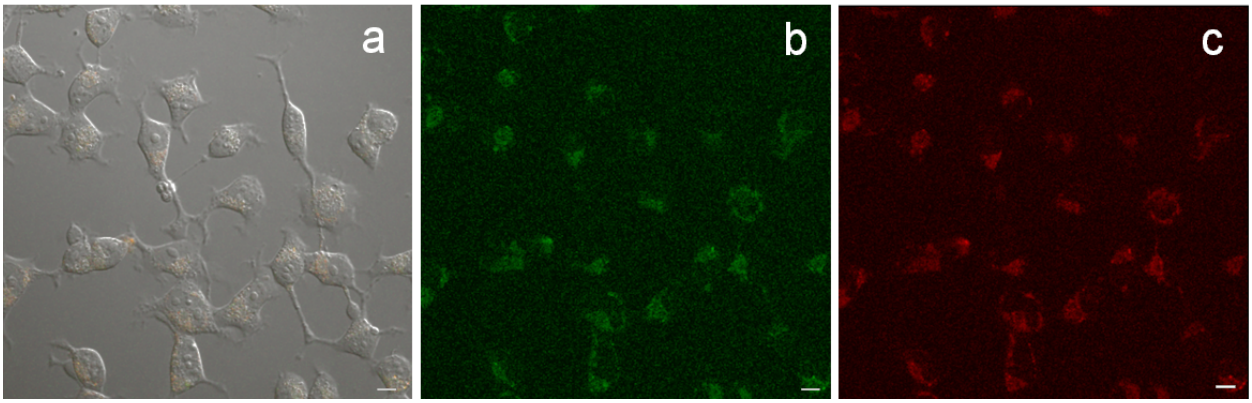


Figure 4**.** Cell images with a 10 μm scale bar. a) The merged image by overlaying transmission light cell image with green and red fluorescence confocal images; b) The green fluorescence image acquired at the GFP wavelength (~ 510 nm) using a 488 nm excitation laser; and c) The red fluorescence image acquired at the Texas Red wavelength (~ 615 nm) using a 560 nm excitation laser.

Z-stacking analysis was further conducted to verify the internalization of the autofluorescent BSA nanoparticles in the cellular cytoplasm. After confirming the cell focusing ranges from the bottom to top, focal plane images were captured at 3 μm (Figure S4a-c), 7 μm (Figure S4d-f), and 15 μm (Figure S4g-i) from the bottom. Relatively weak fluorescence was found at focal plane near the bottom (3 μm from the bottom) as well as focal plane near the top (15 μm from the bottom), respectively. As shown in Figure S4b, c, h, i, there is nearly no detectable green or red fluorescence signal, and the merged images (Figure S4a and g) are also in good agreement with the corresponding confocal images, corroborating the claim that no autofluorescent nanoparticles existed on the surface of the cell. Moreover, relatively intense green and red

fluorescence signal was observed when we focused at the middle height of the cell (Figure S4e and f), which was further approved by the obvious small fluorescent dots in the merged image (Figure S4d). In conjunction with the confocal intersectional fluorescent images (Figure S5), these results strongly suggest the intracellular uptake of autofluorescent BSA nanoparticles by the cells. It is known that the design of drug carrier matrix or bioimaging probe is very important for *in vivo* tests of complex biological systems. Cell penetration ability of the nanomaterials is typically attributed to membrane trafficking, [4] therefore, the interaction between membrane and BSA in autofluorescent nanoparticles might play an important role in trafficking BSA nanoparticles into cells. This observation is also in agreement with the literature report that proteins (such as BSA) doped fluorescent nanoparticles can be easily taken by the cell.[6] This result indicates that autofluorescent BSA nanoparticles with an average size of ~40 nm could be a promising drug nanocarrier matrix or bioprobe for cellular imaging.

### 3.3.3 *In vitro* cytotoxicity, *in vivo* time-dependent imaging/modeling, biodegradation and biocompatibility test

As a potential drug carrier matrix or bioimaging probe for *in vivo* application, the nanomaterial itself should exhibit good biocompatibility or low cytotoxicity.[23, 24] Therefore, cell viability study based on a traditional CCK-8 colorimetric cytotoxicity assay was conducted to evaluate the biocompatibility of autofluorescent BSA nanoparticles. As the glutaraldehyde has a certain level of cytotoxicity in the cells, a dialysis process using 10 mM pH 7.4 PBS buffer has been employed to remove unreacted GA. Figure 18 shows cell viability after incubation for 24 hr with different concentrations of the autofluorescent BSA nanoparticles (0.47, 0.94, 1.875, and 3.75 mg/mL). Statistically, 100% of the cells appear alive. This result indicates good

biocompatibility/low cytotoxicity of the as-synthesized autofluorescent nanomaterials, thus providing solid ground for the later *in vivo* applications.

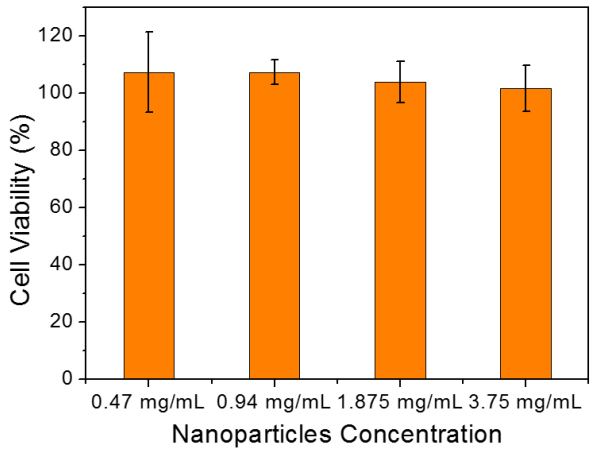


Figure 5. Viability of the A549 cancer cells after incubation with autofluorescent BSA nanoparticles at various concentrations of 0.47, 0.94, 1.875, and 3.75 mg/mL for 24 hrs, respectively.

Since the protein nanoparticles exhibit good autofluorescent properties, an *in vivo* biodegradation study was carried out based on non-invasive fluorescence imaging at different time intervals after its *in vivo* injection. Specifically, 100 μL of BSA nanoparticles suspension at a concentration of 3.75 mg/mL was subcutaneously injected into athymic nude (nu/nu) mice using a gauge 27 needle, and the corresponding fluorescence images at the injection site of the mouse were *in situ*, non-invasively tracked over a time course of 18 days (or 432 hours) using an IVIS Lumina LT system (Figure 6). The results indicate that the injected autofluorescent nanoparticles could be fully degraded within 18 days.

Interestingly, strong fluorescence was observed at the injection site when images were collected at an emission of 595 nm with an excitation wavelength of 535 nm. Non-invasive, time-dependent fluorescence images allow for conveniently tracking of biodegradation and diffusion of injected autofluorescent nanoparticles at different time intervals. As shown in Figure 6,

immediately after the subcutaneous injection, the BSA nanoparticle liquid dispersion is released from the injection point (the center of the circular pattern), thus resulting in strong and localized radiant fluorescence intensity. The fluorescence intensity at the center of the injection site gradually diminished, accompanied by gradual broadening of fluorescent area, which was corroborated by images taken at 2 hrs and 6 hrs post injection. Such phenomenon might be ascribed to the diffusion of autofluorescent BSA nanoparticles. After the initial expansion, the fluorescence area became smaller and the fluorescence intensity decayed between 6 to 144 hrs post-injection until the whole area was prevailed by background intensity, shown by the image at 216 hrs post injection. This data can be attributed to the gradual degradation of the autofluorescent nanoparticles along with absorption into systemic circulation.

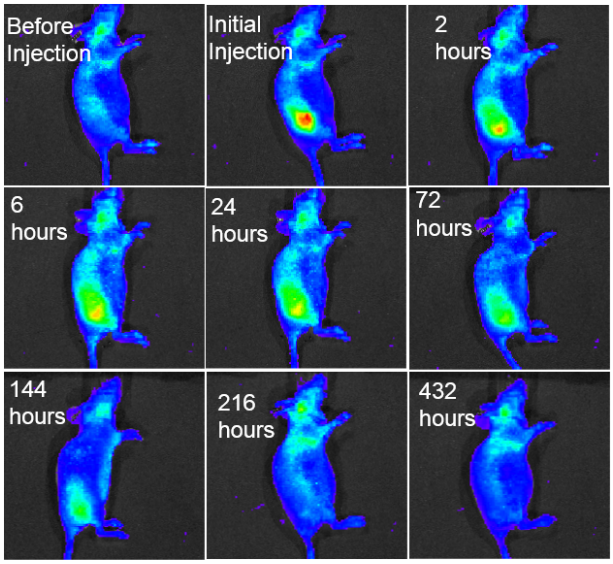


Figure 6**.** Fluorescence images acquired at different times for the mouse injected with autofluorescent nanoparticle suspension.

The temporal and spatial correlations of the radiant intensity and the concentration of fluorophores can be simulated and physically understood by the diffusion/degradation process. To simplify the mathematical model one can assume that the fluorescent pattern is axisymmetric and quasi-two dimensional for the long-time Brownian diffusion of fluorophores. The liquid

dispersion is released from the injection point at the center point of the circular pattern. The radiant intensity is scaled by the maximum intensity recorded for convenience and is correlated to the fluorophore concentration, which can be described by the linear transient diffusion equation:

$$\frac{\partial c(r,t)}{\partial t} = D_{\text{eff}} \nabla^2 c - S(c) \qquad \text{for} \qquad 0 \le r < b, \quad t \ge 0, \qquad (1)$$

where c is local concentration, r is radial coordinate in an unbounded domain, t is time, $D_{\text{eff}}$ is an effective diffusivity of nanoparticles in solution, $S(c)$ represents the assumed linear concentration-dependent attenuation of the fluorescence intensity. As the fluorophores were degraded, digested and finally cleared through blood circulating for 180 to 200 hrs based on the modelling data, the remaining background intensity is no longer uniform. It is reasonable to apply an exponential decaying function (Figure S6a) to describe the transient effective diffusivity to accommodate this effect, expressed as

$D_{\text{eff}}(t) = D_0\, g(t)$, where the correction factor is $g(t) = A_1 \exp\left(-\alpha_1 t^{\beta_1}\right) + B_1$. (2)

Note that $A_1 + B_1 = 1$, $D_0$ indicates the diffusivity in the relatively free diffusion limit not far away from the initial stage where the correction factor $g(t) \to 1$, and $\alpha_1$ and $\beta_1$ are adjustable powers to reduce the effective diffusivity, presumably due to absorption or deep penetration into the tissue.

Combining Eqs. (1) and (2), expanding the axisymmetric equation, and considering a first-order absorption kinetics we obtain

$$\frac{\partial c(r,t)}{\partial t} = D_0 g(t)\left(\frac{\partial^2 c}{\partial r^2} + \frac{1}{r}\frac{\partial c}{\partial r}\right) - \lambda c \quad ,(3)$$

and the corresponding boundary conditions are

$$\partial c / \partial r = 0 \quad \text{at} \quad r = 0; \quad \partial c / \partial r = 0 \quad \text{as} \quad r \to \infty. \qquad (4)$$

Ideally the initial condition can be formulated by an impulse source term. However, to accommodate a small time delay from the injection process to the first measurement, the following exponential function is used to match the initial condition (Figure S6b):

$$c(r,0) = A_2 \exp\left(-\alpha_2 r^{\beta_2}\right) + B_2 \quad \text{for} \quad 0 \le r < b. \quad (5)$$

Both exponential decaying functions in equations (2) and (5) provide a flexible adjustment of the diffusive process including the attenuation of radiant signals. Once the parameters are adjusted, the transient distribution of the fluorophores is solely governed by the diffusion equation and imposed boundary conditions without further fitting to the experimental data. The physics-based semi-empirical model is numerically solved by the standard RK4 time integration method and finite difference scheme.

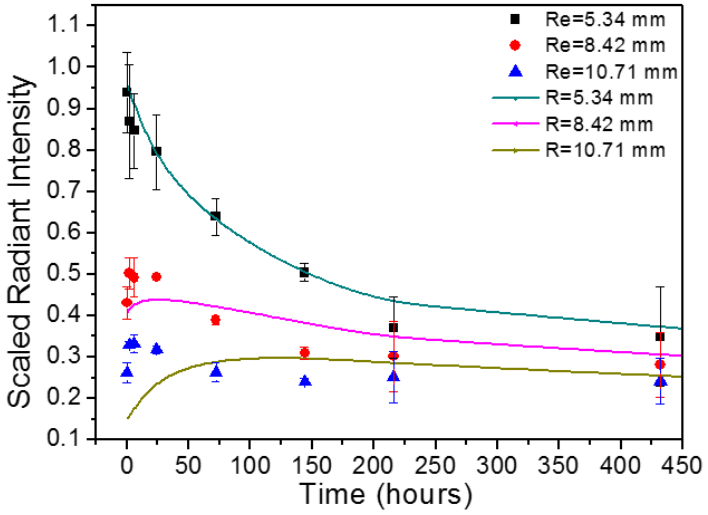

Figure 7**.** Scaled radiant intensity versus time at three locations, $r$ = 5.34, 8.42, and 10.71 mm. Data points with error bars are experimental results, and the the solid lines present modeling results at the corresponding locations.

Figure 7 shows the comparison of experimental and theoretical results. The experimental data have a characteristic time scale about 100 hrs and a diffusive length about 3 to 4 mm, and thus it is reasonable to guess the initial diffusivity $D_0$ around 0.11 mm$^2$/hr, about 3% of the diffusivity of small molecules in water (~$10^{-9}$ m$^2$/s). Because there is no obvious spatial confinement on the diffusive mass flux around the physical domain, a vanishing far-field boundary condition at infinity is assumed. The initial condition is approximated by the beginning measurement, and the effective diffusivity is empirical in this model that describes the fluorophore transport process. Overall the phenomenological modeling result agrees reasonably well with experimental data. The remaining background intensity after 200 hrs implies that the degraded nanoparticles have been absorbed into the tissue and have much less diffusivity than their initial value. Furthermore, the concentration-dependent absorption has little influence on the diffusion process in this case, and thus is presented by a small sink term with $\lambda$ set to $5\times10^{-4}$ hr$^{-1}$. The transient profile at $r$ = 10.71 mm is slightly off from the experimental data, perhaps owing to the simplification of axisymmetric pattern in a relatively large and bounded domain, in which the configuration is more three-dimensional during the later stage of the diffusive process. Small overshoots appeared at early stage of the transient profiles for $r$ = 5.34 mm and $r$ = 8.42 mm are reasonable. It is due to the propagation of diffusive wave that passes through these corresponding locations.

After the nanoparticles degraded and fully digested and cleared by blood circulatory system, *in vivo* biocompatibility study was performed through histological analysis and the corresponding results were presented in Figure S7. For skin around the injection spot (Figure S7), the skin has a moderate to marked hyperkeratosis on the epidermis and extending down into the hair follicles

with hyperplasia of the epidermis. There are numerous hair follicles present with some containing fragments of hair shafts. There is no evidence of inflammation in the dermis or subcutaneous tissues. Also there is no inflammation evidence presented in pancreas (Figure S7b), liver (Figure S7c), and kidney (Figure S7d). This histology study further demonstrates the good *in vivo* biocompatibility of the as-prepared autofluorescent BSA nanoparticles.

## *3.4 Conclusion*

In summary, BSA nanoparticles with green and red autofluorescence have been facilely fabricated and further characterized using various advanced techniques. According to UV-vis spectra and fluorescence emission spectra, the fluorogenic origin of autofluorescent BSA nanoparticles has been discussed and proposed to the best of our knowledge. The biocompatibility and biodegradability of the as-prepared autofluorescent BSA nanoparticles were also demonstrated through extensive *in vitro* and *in vivo* studies based on the cytotoxicity test on the A549 cancer cells and tissue histological analysis, respectively. Its application for cell imaging was validated using 293FT human kidney cell line. The autofluorescent BSA nanoparticles were further exploited in non-invasive, *in vivo* degradation tracking based on real-time fluorescence imaging. A mathematic model was proposed for the first time to describe the degradation of the autofluorescent BSA nanoparticle with good agreement with the experimental data. This study indicates that the as-prepared functional, biocompatible and biodegradable autofluorescent protein nanoparticles are suitable for a range of biomedical applications.

**Reference**


1. Kumar, A., Chen, F., Mozhi, A., Zhang, X., Zhao, Y., Xue, X., Hao, Y., Zhang, X., Wang, P. C. and Liang, X.-J. (2013) Innovative pharmaceutical development based on unique properties of nanoscale delivery formulation. Nanoscale*,* **5,** 8307-8325.
2. Slowing, I. I., Trewyn, B. G., Giri, S. and Lin, V. Y. (2007) Mesoporous silica nanoparticles for drug delivery and biosensing applications. Advanced Functional Materials*,* **17,** 1225-1236.

3. Alkilany, A. M., Nagaria, P. K., Hexel, C. R., Shaw, T. J., Murphy, C. J. and Wyatt, M. D. (2009) Cellular uptake and cytotoxicity of gold nanorods: molecular origin of cytotoxicity and surface effects. Small, **5,** 701-708.
4. Yao, J., Yang, M. and Duan, Y. (2014) Chemistry, biology, and medicine of fluorescent nanomaterials and related systems: New insights into biosensing, bioimaging, genomics, diagnostics, and therapy. Chemical reviews, **114,** 6130-6178.
5. Lavis, L. D. and Raines, R. T. (2008) Bright ideas for chemical biology. ACS chemical biology, **3,** 142-155.
6. Qin, W., Ding, D., Liu, J., Yuan, W. Z., Hu, Y., Liu, B. and Tang, B. Z. (2012) Biocompatible Nanoparticles with Aggregation- Induced Emission Characteristics as Far- Red/Near- Infrared Fluorescent Bioprobes for In Vitro and In Vivo Imaging Applications. Advanced Functional Materials, **22,** 771-779.
7. Chan, W. C. and Nie, S. (1998) Quantum dot bioconjugates for ultrasensitive nonisotopic detection. Science, **281,** 2016-2018.
8. Skrabalak, S. E., Chen, J., Sun, Y., Lu, X., Au, L., Cobley, C. M. and Xia, Y. (2008) Gold nanocages: synthesis, properties, and applications. Accounts of chemical research, **41,** 1587-1595.
9. Sharma, P., Brown, S., Walter, G., Santra, S. and Moudgil, B. (2006) Nanoparticles for bioimaging. Advances in colloid and interface science, **123,** 471-485.
10. Qian, X., Peng, X.-H., Ansari, D. O., Yin-Goen, Q., Chen, G. Z., Shin, D. M., Yang, L., Young, A. N., Wang, M. D. and Nie, S. (2008) In vivo tumor targeting and spectroscopic detection with surface-enhanced Raman nanoparticle tags. Nature biotechnology, **26,** 83-90.
11. Nakamura, M., Shono, M. and Ishimura, K. (2007) Synthesis, characterization, and biological applications of multifluorescent silica nanoparticles. Analytical chemistry, **79,** 6507-6514.
12. Lee, S. H., Heng, D., Ng, W. K., Chan, H.-K. and Tan, R. B. (2011) Nano spray drying: a novel method for preparing protein nanoparticles for protein therapy. International journal of pharmaceutics, **403,** 192-200.
13. Gülseren, İ., Fang, Y. and Corredig, M. (2012) Zinc incorporation capacity of whey protein nanoparticles prepared with desolvation with ethanol. Food chemistry, **135,** 770-774.
14. Sundar, S., Kundu, J. and Kundu, S. C. (2010) Biopolymeric nanoparticles. Science and Technology of Advanced Materials, **11,** 014104.
15. Migneault, I., Dartiguenave, C., Bertrand, M. J. and Waldron, K. C. (2004) Glutaraldehyde: behavior in aqueous solution, reaction with proteins, and application to enzyme crosslinking. Biotechniques, **37,** 790-806.
16. Nimni, M. E., Cheung, D., Strates, B., Kodama, M. and Sheikh, K. (1987) Chemically modified collagen: a natural biomaterial for tissue replacement. Journal of Biomedical Materials Research, **21,** 741-771.
17. Lee, K., Choi, S., Yang, C., Wu, H.-C. and Yu, J. (2013) Autofluorescence generation and elimination: a lesson from glutaraldehyde. Chemical Communications, **49,** 3028-3030.
18. Wei, W., Wang, L.-Y., Yuan, L., Wei, Q., Yang, X.-D., Su, Z.-G. and Ma, G.-H. (2007) Preparation and application of novel microspheres possessing autofluorescent properties. Advanced Functional Materials, **17,** 3153.
19. Elzoghby, A. O., Samy, W. M. and Elgindy, N. A. (2012) Albumin-based nanoparticles as potential controlled release drug delivery systems. Journal of Controlled Release, **157,** 168-182.
20. Subia, B. and Kundu, S. (2013) Drug loading and release on tumor cells using silk fibroin–albumin nanoparticles as carriers. Nanotechnology, **24,** 035103.
21. de la Fuente, J. M. and Berry, C. C. (2005) Tat peptide as an efficient molecule to translocate gold nanoparticles into the cell nucleus. Bioconjugate chemistry, **16,** 1176-1180.
22. Tong, R., Chiang, H. H. and Kohane, D. S. (2013) Photoswitchable nanoparticles for in vivo cancer chemotherapy. Proceedings of the National Academy of Sciences, **110,** 19048-19053.
23. Lewinski, N., Colvin, V. and Drezek, R. (2008) Cytotoxicity of nanoparticles. Small, **4,** 26-49.

24. Ding, D., Li, K., Qin, W., Zhan, R., Hu, Y., Liu, J., Tang, B. Z. and Liu, B. (2013) Conjugated Polymer Amplified Far- Red/Near- Infrared Fluorescence from Nanoparticles with Aggregation- Induced Emission Characteristics for Targeted In Vivo Imaging. Advanced healthcare materials, **2,** 500-507.

## *Supplementary Materials*

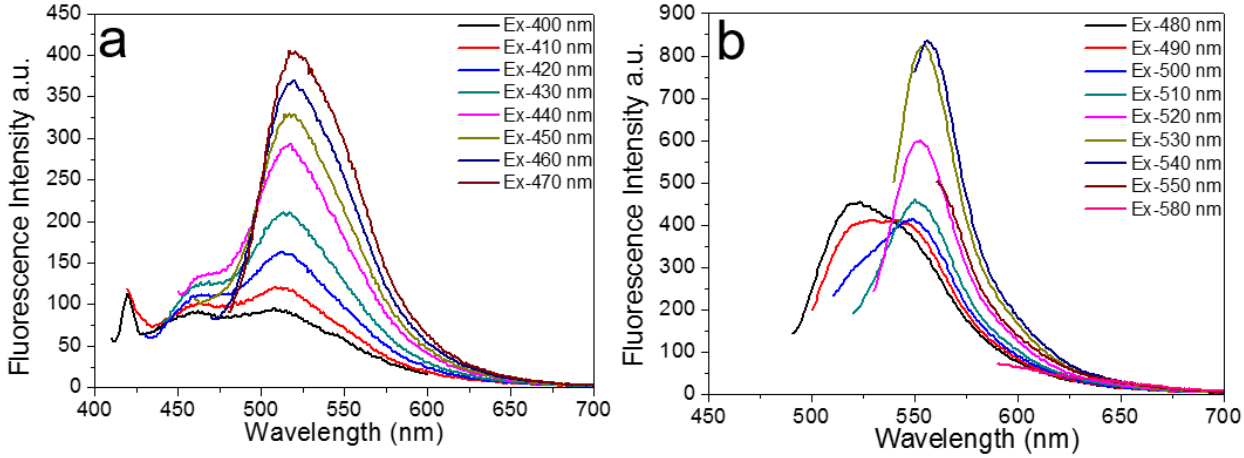


Figure S1. Fluorescence emission scan of the glutaraldehyde cross-linked BSA nanoparticles without autoclave treatment.

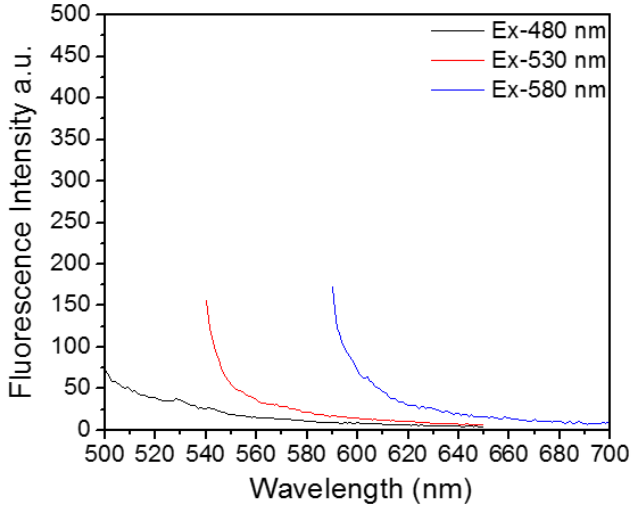


Figure S2. Fluorescence emission spectra of the BSA aggregation dispersion.

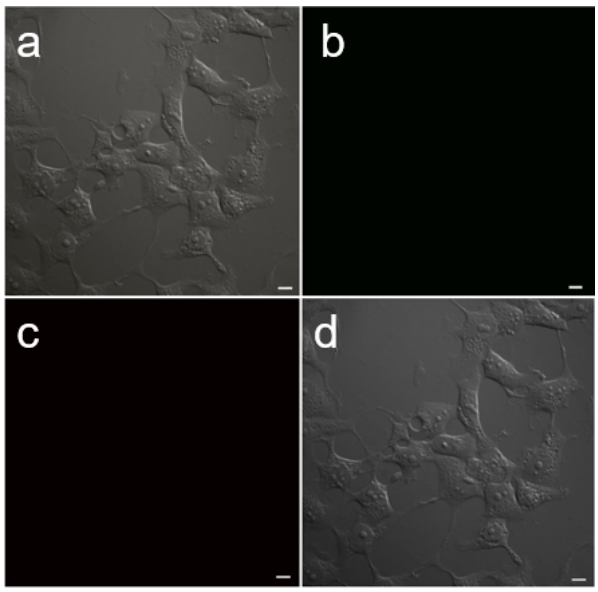


Figure S3. Control cell images (293FT cells without exposure to autofluorescent BSA nanoparticles). Scale bar = 10 µm. a) The merged image by overlaying transmission light cell image with green and red fluorescence confocal images; b) The green fluorescence image acquiring at the GFP wavelength range (~510 nm) with a 488 nm excitation laser; c) The red fluorescence image acquiring at the Texas red wavelength range (~615 nm) with a 560 nm excitation laser; and d) The cell image under a transmission light.

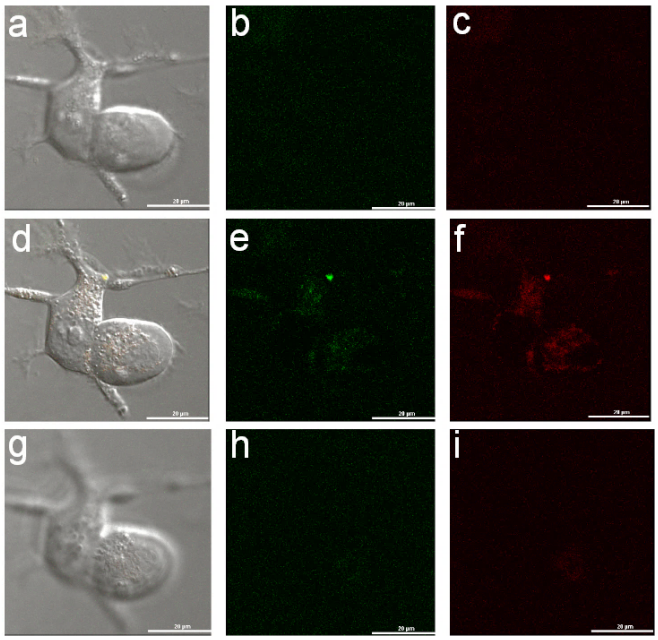


Figure S4. Z-stacking of the confocal images focusing on one single cell at different focal planes. Scale bar = 20 µm. a) The merged image by overlaying the transmission light, green, and red fluorescence images at a height of 3 µm from the bottom; b and c) The green and red fluorescent image at a height of 3 µm from the bottom, respectively; d) the merged image by overlaying the transmission light, green, and red fluorescence images at a height of 7 µm from the bottom; e and f) The green and red fluorescent image at a height of 7 µm from the bottom, respectively; g) the

merged image by overlaying the transmission light, green, and red fluorescence images at a height of 15 μm from the bottom; h and i) The green and red fluorescent image at a height of 15 μm from the bottom, respectively.

Cross-sectional confocal image of the cell was obtained to observe the inner cytoplasm fluorescence. As the corresponding result presented in Figure S5, the obvious green and red fluorescence signal comparing with the background signal also indicates the uptake of autofluorescent nanoparticles by the cell.

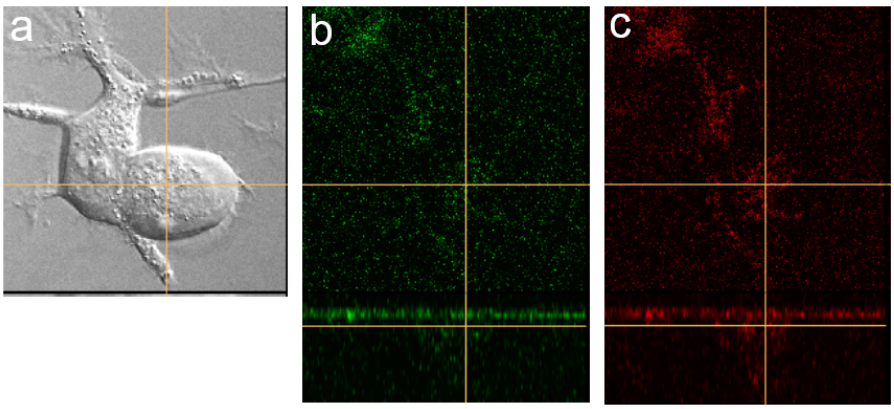


Figure S5. Confocal slice images indicate the intersection fluorescence. a is the cell image under transmission light, and the intersection of the yellow line was used for confocal slice images to observe the inner cytoplasm fluorescence, while in b) and c), the bottom intersection of the yellow line presents the green and red fluorescence of the cutting section of the intersection shown in a.

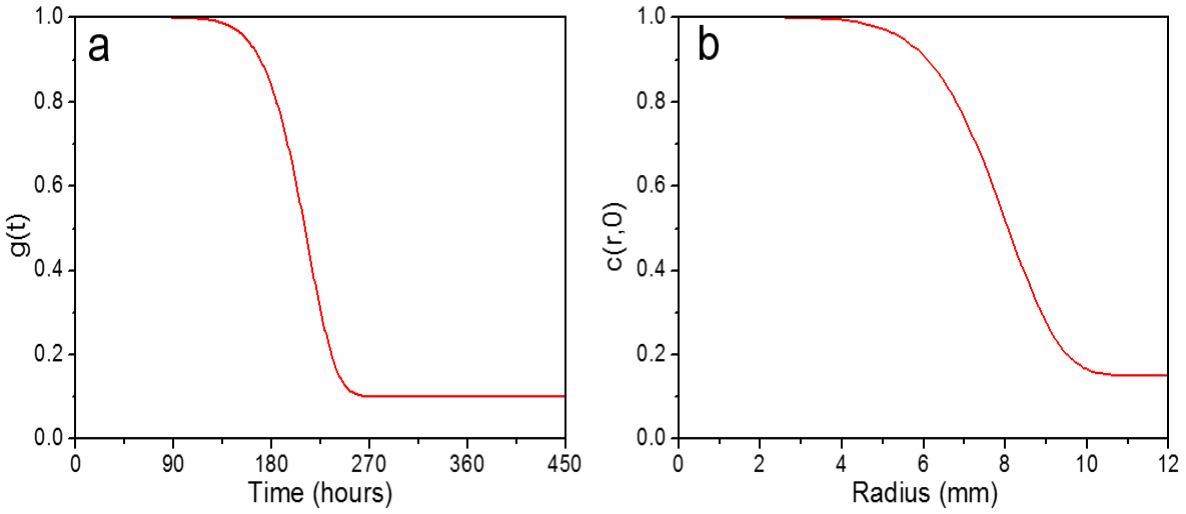


Figure S6. a) Temporal effective diffusivity represented by the correction factor: $g(t) = D_{eff}(t)/D_0 = 0.1 + 0.9 \exp(-10^{-21} t^9)$; and b) initial condition fitted by an exponential function: $c(r, 0) = 0.15 + 0.85 \exp(-10^{-6.4} r^7)$.

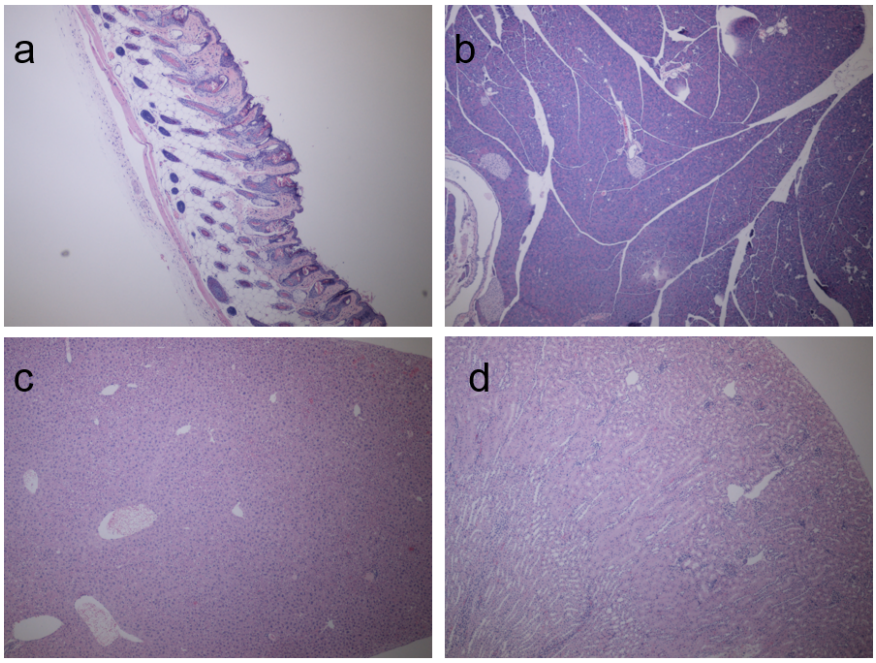


Figure S7. The results of the histology study. a) A skin tissue image (40×); b) A pancreas tissue image (40×); c) A liver tissue image (40×); and d) A kidney tissue image (40×).

# Chapter 4

# Protein Microspheres with Unique Green and Red Autofluorescence for Non-invasively Tracking and Modelling Their *In Vivo* Biodegradation

**Abstract**

Spray-dried bovine serum albumin (BSA) microspheres were prepared through a facile and low-cost route including a high-speed dispersion in cross-linking solution followed by spray drying. Interestingly the as-prepared BSA microspheres possess unique blue-green, green, green-yellow, and red fluorescence when excited by specific wavelengths of laser or LED light. The studies of UV-visible reflectance spectra and fluorescence emission spectra indicated that four classes of fluorescent compounds are presumably formed during the fabrication processes. The formation and the potential contributors for the unique autofluorescence were also discussed and proposed though the exact structures of the fluorophores formed remains elusive due to the complexity of the protein system. The study of the effect of spray-drying conditions on the morphology of spray-dried samples suggested that temperature at 100 ℃ or above with an appropriate pumping rate yields microspheres with smooth and spherical surface morphology according to the FESEM images. FTIR was further employed to characterize the formation of the functional groups in the as-prepared autofluorescent microspheres. Good *in vitro* and *in vivo* biocompatibility has been demonstrated by the cytotoxicity test on the A549 cancer cells and tissue histological analysis, respectively. Potential applications of the autofluorescent BSA microspheres were first demonstrated as a novel tracer for convenient tracking/modelling of the biodegradation of injected autofluorescent BSA microspheres in mouse model based on non-invasive, time-dependent fluorescence images of the mice, in which experimental data are in good agreement with the proposed diffusive model. All these studies indicate that the as-developed protein

microspheres exhibiting good biocompatibility, biodegradability, and unique autofluorescence, can significantly broaden biomedical applications of protein fluorescent particles.

## *4.1 Introduction*

Polymeric nano- and microspheres have been raised as a unique class of materials to be applied in a variety of divisions related to medical domains, including drug delivery matrix, biological tracers, medical diagnostics, personal care, etc.[1-4] Natural polymers such as polysaccharides (e.g., chitosan[5] and alginate[6]) and proteins (e.g., casein[7]), have been attracting great attention in biomedical applications, ranging from the drug delivery and cell imaging to biosensors.[8] These are mainly driven by their good *in vivo* biocompatibility.[9] To understand various fundamental processes in life sciences, direct tools used for monitoring and tracking are highly demanded. As for *in vivo* applications, microspheres can be employed for the investigation of regional blood flow in organs such as lungs, or tracking the new blood cells, which is significant for the cancer study and microvascular continuity.[10] Thus, radiolabelled microspheres have often been used *in vivo* since a gamma-scintigraphy camera is able to track the distribution of such microspheres in the body.[11] However, the toxicity and instability of the labelled microspheres always induces false signals, significantly diminishing the reliability of the results. Fluorescence has turned out to be as an excellent substitute of radiolabels. [3, 12] To synthesize fluorescent microspheres, chemical fluorophores such as fluorescein[2] have been encapsulated in the microsphere system through physically doping or covalent bonding. However, in addition to potential leakage and photobleaching of those entrapped fluorescent molecules, their biocompatibility and biodegradability are also questionable, and thus their applications are limited. Therefore, there is an urgent need to develop novel autofluorescent protein microspheres without the use of fluorophore labels, capable of exhibiting good biocompatibility and biodegradability, as well as desirable excitation/emission fluorescence wavelengths for convenient *in vivo* tracking.

Herein, we report the synthesis of protein microspheres with unique autofluorescent through a facile, low-cost and scalable route including a high-speed dispersion of bovine serum albumin (BSA) in glutaraldehyde crosslinking solution followed by a spray drying process (Scheme 1). Because of its high efficiency in large scale manufacturing, spray-drying technology is extremely attractive to serve as a rapid, convenient, and precision process for powder preparation which have been employed in various aspects, including suspensions drying, micronizing/crystallizing/encapsulation of active species for food and drug applications,[13, 14] and synthesis of other materials[15] (e.g., silica,[16] carbon nanotubes,[17] and organic crystals[18-20]). On the other hand, BSA, a widely used protein due to its low cost, stability, good solubility and unusual ligand-binding properties, presents intrinsic fluorescence with the emission wavelength at 348 nm when excited at 279 nm, which is ascribed to the tryptophan residues in the protein.[21] However, the excitation/emission wavelengths of the protein in the UV range are an enormous barrier for *in vivo* biomedical applications due to its irreversible damage to the living tissues. Glutaraldehyde (GA), a linear 5-carbon dialdehyde with apparent, colourless, pungent properties, is an efficient cross-linker to react with the amine groups forming thermal and chemical stable Schiff base comparing with other aldehyde, [22] which was used as the cross-linker to generate the unique autofluorescence in cross-linked BSA in this study. After spraying drying, GA residue can be removed from the final product, thus eliminating its potential negative effect on any biomedical applications. To characterize the as-prepared samples, various advanced techniques were employed including Field Emission Scanning Electron Microscopy (FESEM), Fourier transform infrared spectroscopy (FTIR), UV-visible reflectance spectra, fluorescence emission spectra, and confocal laser scanning microscopy. The fluorogenic mechanism was discussed and proposed to the best of our knowledge. Moreover, *in vitro* and *in*

*vivo* biocompatibility of the as-prepared sample was systematically evaluated based on the cytotoxicity test on the A549 cancer cells and tissue histological analysis, respectively. The red fluoresce of the as-prepared microspheres were further applied for convenient tracking of the biodegradation of autofluorescent BSA microspheres injected into mouse model, according to non-invasive, time-dependent fluorescence images of the mice. A mathematical model was proposed which is in good agreement with the experimental data. These studies indicate that the as-prepared protein microspheres with unique autofluorescence hold great promise in a variety of biomedical applications.

## *4.2 Experimental*

### 4.2.1 Materials

Bovine serum albumin (lyophilized powder) was obtained from Sigma Aldrich. Glutaraldehyde solution (50%, in DI water) and formaldehyde (37%, in DI water) were bought from Acros Organics. Dulbecco's Modified Eagle Medium (DMEM), CCK-8, and fetal bovine serum (FBS) were purchased from Gibco. All other chemicals were of analytical grade. PBS buffer saline (10 mM pH 7.4) was prepared using sodium phosphate dibasic, potassium phosphate monobasic, sodium chloride in DI water. A549 cancer cell line was obtained from Sigma Aldrich. Athymic nude mice (2 months old) were purchased from Harlan Sprague Dawley Inc.

### 4.2.2 Fabrication of Autofluorescent BSA Microspheres

BSA powder was dissolved in 10 mM pH 7.4 PBS buffer at a final concentration of 150 mg/mL. 50% glutaraldehyde solution was diluted 10-fold with PBS buffer with a final volume of 20 mL, and then 1 mL n-butanol was added and well mixed as glutaraldehyde dispersion. 1 mL of 150 mg/mL BSA solution was concurrently added dropwise into the dispersion under high speed dispersion (IKA disperser with setting at "5") to prepare 21 mL glutaraldehyde/BSA dispersion.

As a result, transparent cross-linked BSA suspension was formed as the precursor for spray-drying. Spray-drying was then performed using a spray drier (Büchi Nano Spray Dryer B-90) with fixed temperatures at 100 ℃ and 120 ℃, and airflow rate at 120 L/min and pressure at 30-40 hPa, with feeding rates setting of "2" and "3", respectively. The as prepared precursor suspension was diluted two times prior to spray-drying. The light brown powder was obtained as the final product for further application.

### 4.2.3 Characterization

Surface morphology of the as-prepared autofluorescent microspheres was investigated using JEOL 6335 FESEM with an operating acceleration voltage at 10 kV and a current of 12 μA. Prior to SEM imaging, thin layers of three different microsphere powders (two for spray temperature at 120 ℃ with pump rate setting at "2" and "3" respectively, and one for spray temperature at 100 ℃ with pump rate setting at "2") were attached on three different stubs with a copper tape. In addition, the samples were sputtered coated with Au/Pd alloy for 50 seconds in a vacuum with a current of 10 mA. FTIR spectra were collected on Nicolet 560 Fourier spectrometer using a Diamond ATR accessory. The spectra were collected in the range of 500 – 4000 $cm^{-1}$ using 32 scans. Before acquisition, the IR spectra were baseline corrected for carbon dioxide peak around 2750 $cm^{-1}$. UV-visible spectra were collected from 250 nm to 650 nm using a Shimadzu UV-2450 UV-vis spectrophotometer. For each test, samples were diluted by $BaSO_4$ at the mass ratio of 1:5, and the holder with $BaSO_4$ powder was scanned at the same time as the baseline. Prior to the acquisition, the mixed powders were compressed in order to have a smooth surface. The as-prepared BSA microsphere powder was also compressed to form a thin disk for the investigation of photophysical properties. Fluorescence emission spectra were collected by Fluorescence Spectroscope (Horiba Fluorolog III) using a solid sample holder. It was excited at

30 individual wavelengths at 10 nm sequential increments from 290 to 580 nm, with the emission captured from a wavelength slightly above excitation wavelength. In addition, Confocal Microscopy (Nikon A1R Spectral) was applied to image the individual autofluorescent microspheres. Prior to imaging, autofluorescent microspheres were suspended in DI water with a concentration of 10 mg/mL. Then the suspension was sonicated for 10 minutes, followed by dilution as follows: 10 μL sample suspension mixed with 90 μL 70% ethanol and 900 μL DI water. Finally, 20 μL diluted suspension was loaded on the cover slip. After it is fully dried, 15 μL mounting media (90% glycerol) was loaded and a glass slide was covered on the cover slip. The autofluorescent microsphere images were collected using excitation wavelengths at 488 and 560 nm and an acquisition long pass filter of 510 and 615 nm, respectively.

**4.2.4 Cytotoxicity study of autofluorescent microspheres**

A549 cancer cell were applied to evaluate the cytotoxicity/ biocompatibility of the autofluorescent microspheres using CCK-8 assay. Briefly, A549 cells were seeded in a 96-well plate with the density of around 5000 cells per well and incubated at 37 ℃ in the DMEM containing FBS. Then the cells were exposed to 0, 0.01%, 0.05%, 0.1%, 0.5%, 1% autofluorescent BSA microspheres powder suspended in FBS-free DMEM (5 wells for each sample) and keep one column with no cells as the blank. After 24-hour incubation at 37 °C, the samples were removed and washed several times with PBS buffer, and replaced by fresh DMEM containing FBS medium (100 μL per well). After that, 10 μL of CCK-8 solution was added into each well. Finally, after 1 hour of cultivation in incubator at 37 °C, the absorption at wavelength of 450 nm was recorded on a microplate reader. The cell viability percentage was calculated using following formula:

$$\text{Cell Viability } \% = \frac{A_{\text{sample}} - A_{\text{blank}}}{A_0 - A_{\text{blank}}} \times 100\% , \qquad (1)$$

where $A_{sample}$ is the absorbance of the samples at wavelength of 450 nm, $A_{blank}$ is the absorbance of the well with no cells, $A_0$ is the absorbance of the well with no microsphere exposure against the cells.

### 4.2.5 *In vivo* time-dependent imaging, biodegradation and biocompatibility test

All studies were performed according to the University of Connecticut Institutional Animal Care and Use Committee approved protocol and the methods were carried out in accordance with the approved guidelines. Prior to subcutaneously injection of 100 μL 1 wt% autofluorescent BSA microspheres suspension in PBS using a gauge-27 syringe needle, Athymic nude mice were anesthetized using isoflurane and the injection site was cleaned using several pieces of alcohol swab. Then the mice were non-invasively monitored for time-dependent fluorescent imaging. The image was collected and recorded by IVIS Lumia LT system with the excitation source wavelength at the centre of 535 nm and capture emission central wavelength at 595 nm. A mathematical model was built to fit the experimental data and illustrate the biodegradation process. After the autofluorescent microspheres were fully degraded and digested through blood circulate system, the mice were sacrificed to investigate *in vivo* biocompatibility of the materials. The skin of the injection spot, liver, kidney, and pancreas were soaked in 10% formaldehyde and sent to Connecticut Veterinary Medical Diagnostic Laboratory for histological analysis.

## *4.3 Results and Discussions*

### 4.3.1 Morphology of the autofluorescent BSA microspheres

SEM images (Figure 1) show the surface morphology of the microspheres fabricated under different spray-drying conditions, illustrating the size distribution ranging from 1 to 3 μm. Figures 21a and 21b show the microspheres fabricated under spray temperature 120 °C and airflow rate at 120 L/min, with feeding rate set to “2” and ‘3”, respectively, while Figure 1c

presents the microspheres obtained after spray-drying at temperature 100 °C and pump rate at "2". The spray-drying pump has not been set at a low rate of "1" because of the low spraying efficiency. The surface of the microspheres appears smooth and spherical in both cases shown in Figure 1a and 1c, but corrugated in case 1b. The irregular and corrugated particles observed in the SEM images (Figure 1) may come from the dried salt composed in the precursor suspension because PBS buffer was used for sample preparation. Considering the difference of operating conditions in Figure 1a and 1b, the corrugated and rough surface of the microspheres shown in 1b may be partly attributed to the higher sample feeding rate, leading to less drying/heating time within the chamber. As a result, salt is attached on the microspheres after fully dried, indicating the influence of sample feeding rate on the surface morphology of microspheres. Yet, no significant differences between Figure 1a and 1c, which indicates that heating at temperature within the tested range does not influence the surface morphology of the microspheres. Therefore, the proper conditions to fabricate smooth and spherical BSA microspheres are at spray-drying temperature of 100 °C or slightly above with a pump rate of "2".

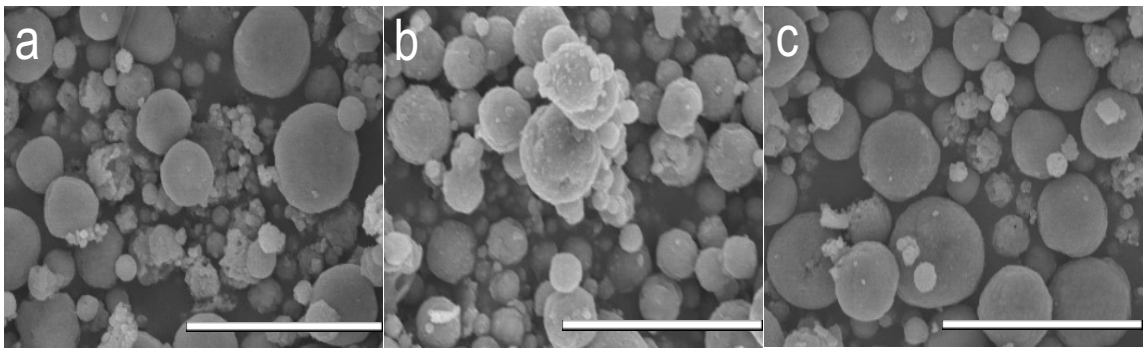


Figure 1. SEM images of autofluorescent microspheres fabricated by spray-drying process under different conditions: (a) temperature 120 °C, pump setting "2", (b) temperature 120 °C, pump setting "3", and (c) temperature 100 °C, pump setting "2". The scale bars shown are 10 μm.

### 4.3.2 FTIR analysis of autofluorescent microspheres

To investigate the structure and composition of the autofluorescent BSA microspheres, FTIR spectra were carried out. As shown in Figure 2, the only newly formed peak in BSA microspheres is around 1722 $cm^{-1}$, which corresponds to the C=O bond and may be attributed to the presence of free –CHO group on the surface of microspheres, since glutaraldehyde composes two CHO-group at both end of the chain and also is excessive in amount. In addition, several common peaks are present in the spectra of both BSA powder and BSA microspheres, with a fingerprint region at 1650 and 1530 $cm^{-1}$, which represents for the amide I and amide II bonds. While, during the cross-linking process, Schiff base should be formed, but it is not observed in FTIR spectrum of BSA microspheres, probably being ascribed to the overlapping of C=N peak (at the wavelength around 1650 $cm^{-1}$) with the strong peak of the amide I. . But we can observe that the absorbance peak at 1650 $cm^{-1}$ of the synthesized microspheres is intenser than that of BSA powder, as comparing the peak around 1530 $cm^{-1}$ representing amide II, which is ascribing to the Schiff base formation after cross-linking. The existence amide bonds and the formation of the C=N bond render the possibility of the π-π* and n-π*electron transition, resulting in the generation of the fluorescence.

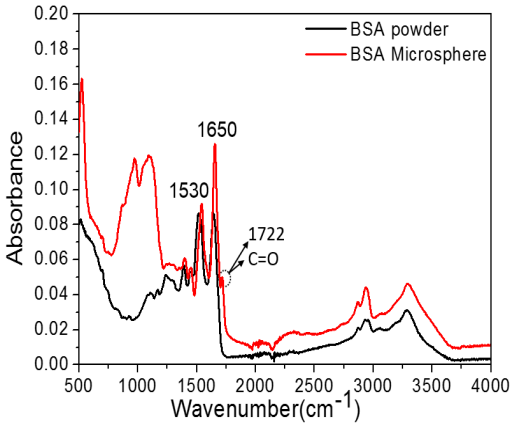


Figure 2**.** FTIR spectra of autofluorescent BSA microspheres (red curve) and BSA powder (black curve) as the control.

### 4.3.3 UV-visible spectra study of autofluorescent microspheres

As the unique green and red fluorescence have been observed after the formation of BSA microspheres using spray-drying and no specific peaks have been observed in FTIR spectra, UV-visible spectra has been carried out to explore the newly synthesized and colorful fluorescent compounds in the fabrication process. Either BSA powder or microspheres have been diluted by $BaSO_4$ as described in the experimental section, and the blank reflectance spectrum of $BaSO_4$ has been conducted as shown in the inset of Figure 3. Spectral analysis of BSA lyophilized powder exhibits a broad reflectance peak centered at the wavelength 280 nm (red curve), which is intrinsic for protein BSA. While, comparing with the UV-visible reflectance spectrum of BSA powder, as-prepared autofluorescent BSA microspheres powder (black curve in Figure 3) presents several peaks: two broad peaks centered around 400 and 480 nm, respectively; two sharp peaks at 300 and 535 nm, respectively, suggesting of four classes of compounds formed during the fabrication process. Based on these, autofluorescent properties of BSA microspheres were led to further investigations.

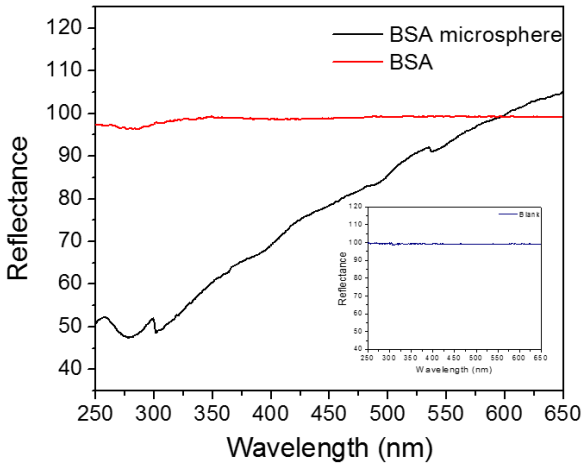


Figure 3. UV-visible reflectance spectra of autofluorescent BSA microspheres and BSA powder, respectively. Black curve is the scan of BSA microspheres and red curve is the scan of commercial BSA lyophilized powder as the control. The inset shows the scan (blue curve) of only BaSO4 as the blank.

### 4.3.4 Images of autofluorescent BSA microspheres

BSA exhibits intrinsic fluorescence with the emission peak around 348 nm when it is excited at 279 nm. However, based on the UV-visible reflectance spectrum in Figure 4, BSA microspheres might present new fluorescence property when excited in a broad wavelength range. To test the hypothesis, confocal laser scanning microscopy (CLSM) has been used as a non-destructive visualization method for individual autofluorescent BSA microspheres. The fluorescence images of the as-prepared autofluorecent microspheres have been collected by Nikon A1R microscope with the excitation lasers wavelengths at ~488 and ~560 nm, respectively, and the emission signals have been captured at the range of GFP (~510 nm, Figure 24a) and Texas Red (~615 nm, Figure 4b), respectively. The fluorescent microspheres under confocal microscope are in the range of 2~3 μm, in good agreements with the size observed in SEM images. In conjunction with the result of UV-visible reflectance spectra (Figure 3), and as control the self-assembled BSA particles obtained through heating process didn't exhibit such unique fluorescence (data not shown), thus fluorescence images of individual microspheres suggest that new classes of fluorescent molecules were synthesized during the microspheres fabrication process.

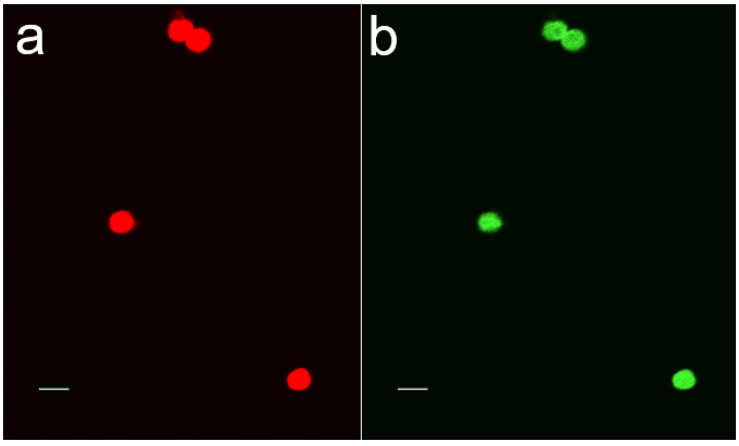


Figure 4**.** Fluorescence images of the BSA autofluorescent microspheres. (a) The fluorescent images (scale bar of 3 μm) of individual BSA microspheres collected by CLSM acquiring at the GFP wavelength range (around 510 nm) with excitation laser of 488 nm. (b) The fluorescent images (scale bar of 3 μm) of individual BSA microspheres collected by CLSM acquiring at the Texas Red wavelength range (around 615 nm) with a 560 nm excitation laser.

### 4.3.5 Fluorescence spectra study of autofluorescent BSA microspheres

Emission spectra of as-prepared autofluorescent BSA microspheres were further collected and recorded with a fluorimeter. Total 30 individual emission scans have been carried out with 10 nm sequential increments of the excitation wavelengths ranging from 290 to 580 nm. According to Figure 5a and 5b, these BSA microspheres can be excited in a broad wavelengths range. When it was excited between 290 and 400 nm, there existed broad blue-green emission peaks (450-510 nm). As the excitation wavelengths increase from 400 to 490 nm, green emission peak at the wavelength of 510 nm and a green to yellow emission shoulder peak centered at 550 nm can be observed. Moreover, the shoulder emission peak at 550 nm became more prominent when excited between 500 and 530 nm. Finally, the emission peak centered around 600 nm appeared when excited between the wavelength of 570 and 580 nm, which is responsible for the observed red fluorescence of the microspheres. These observations presumably indicate the presence of four classes of newly synthesized fluorescent molecules during the microspheres fabrication process, which is in good agreement with the strong autofluorescent images shown in Figure 4.

The fluorescent compounds formed in the fabrication process are extremely complicated due to the poor controllability of the fabrication process. According to some reported studies of the autofluorescence related to glutaraldehyde reaction with peptides or chitosan, [3, 23] probably the secondary amine in the molecule contribute to the fluorogenic mechanism of BSA microspheres. Also, C=C and C=O double bond, existed in the system due to structure of the protein and α, β-unsaturated aldehyde polymer in glutaraldehyde solution, accompanied with C=N double bonds from the Schiff Base after the reaction between glutaraldehyde and amine group in the protein as discussed in the FTIR section, enable the electronic transitions of π-π*

and n-π*, respectively, which is also highly possible to be the potential contributors of the fluorescence observed in the BSA microspheres. Moreover, as the microspheres were obtained by spray-drying process, the temperature and pressure distributions of that process may also contribute to the fluorophores synthesis because temperature-dependent reaction between different functional groups in BSA could occur. More complicatedly, similar to green or red fluorescent proteins, the secondary and/or tertiary structure might significantly influence the formation of fluorescent compounds, where the synergistic effect of several amino acids in close proximity is the origin of the fluorescence. Moreover, the fluorescence of the newly formed compounds may be affected by the charge surrounding the fluorophores in the BSA microspheres. More future efforts are required to identify the accurate chemical structures of the fluorescent compounds formed. Since the autofluorescent BSA microspheres exhibit very good stability with no photobleaching observed when they are set on the bench for several weeks, they are suitable for a wide spectrum of biomedical applications which are demonstrated in subsequent sections.

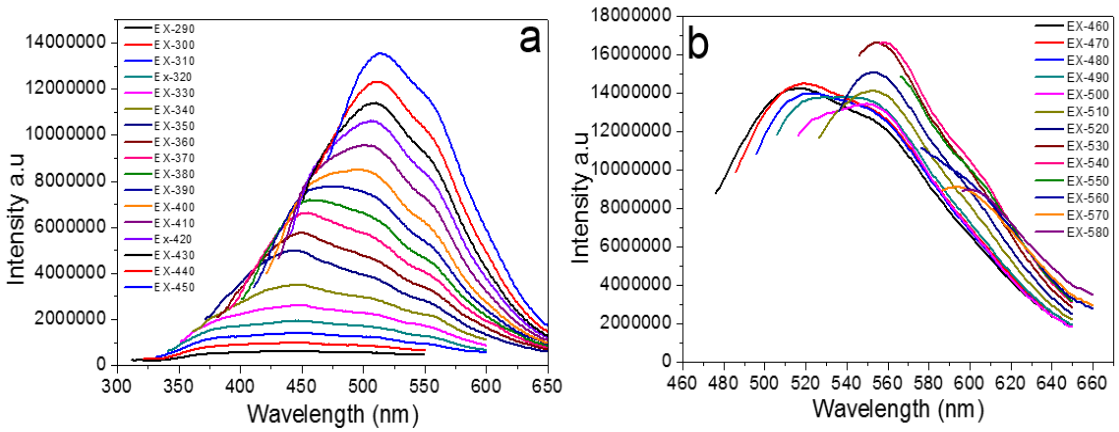


Figure 5. Emission spectra of autofluorescent BSA microspheres at 10 nm sequential increments of excitation wavelength.

### 4.3.6 Cytotoxicity of the as-prepared autofluorescent BSA microspheres

The cytotoxicity of biomaterials is one of the critical factors to be evaluated before any *in vivo* applications.[24] Therefore, *in vitro* cytotoxicity test has been carried out for biocompatibility evaluation of the as-prepared BSA microspheres, using traditional CCK-8 colorimetric assay as described in the experimental section. As glutaraldehyde has a certain level of cytotoxicity to the cells, spray-drying process not only fabricates microspheres with proper morphology, but also eliminates the unreacted glutaraldehyde through vaporization. The cell viability was recorded after 24 hours of incubation with different concentrations of autofluorescent BSA microsphere suspensions (0.01%, 0.05%, 0.1%, 0.5%, and 1%). Statistically 100% of the A549 cancer cells remain alive, as shown in Figure 26. More than 90% of the A549 cancer cells remain alive, as shown in Figure 6. Even when the cells exposing to the microspheres with the concentration as high as 1%, we can obtain that nearly 100% cells are alive.To eliminate the potential interaction between the free aldehyde group in or on the as-prepared BSA microspheres and the serum proteins, FBS-free DMEM was used in the control well, while the BSA microspheres mixed with FBS-free DMEM was applied in the testing wells. These results suggest the good biocompatibility or low cytotoxicity of as-prepared autofluorescent microspheres, providing solid ground for *in vivo* applications.

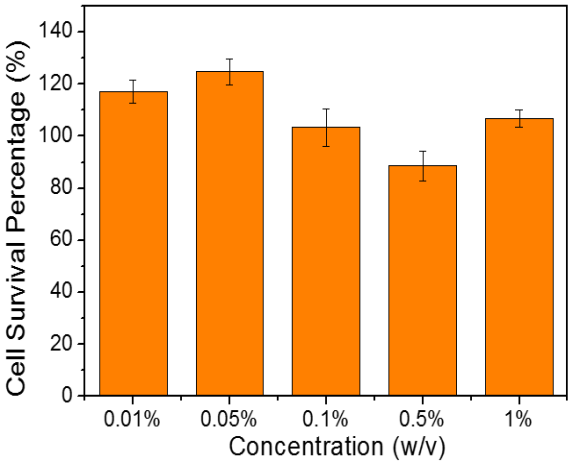

Figure 6. Cell survival percentage after exposure to different concentrations (0.01%, 0.05%, 0.1%, 0.5%, 1%) of the autofluorescent BSA microspheres with 24 hours of incubation

### 4.3.7 Modeling and tracking of *in vivo* imaging and transient biodegradation

Because of the stable autofluorescent property of the BSA microspheres, *in vivo* degradation study was tracked based on fluorescence images non-invasively recorded at different time intervals. 100 μL of 1% autofluorescent BSA microspheres suspension was subcutaneously injected into athymic nude mice as briefly described in the experimental section. The corresponding fluorescent images were *in-situ* tracked at the following time points: initial, 1, 3, 6, 9, 12, 13, 15, and 27 days. As shown in Figure 7, a sequence of images presents the radiant fluorescence intensity corresponding to the transient distribution of the fluorescent compounds. Immediately after subcutaneous injection, intense fluorescence area was observed when images were captured at an emission of 595 nm with the excitation wavelength of 535 nm. The fluorescence of the centre injection site increased after 1 day and then the injection spots decayed along the time until they were totally degraded and digested through circulation system after 27 days. The intensity increases at the first day is partly due to the self-quenching of the fluorophores in a limited area, and then after the degradation, the fluorophores released from the microspheres result in the intense of the center area around the injection spot.

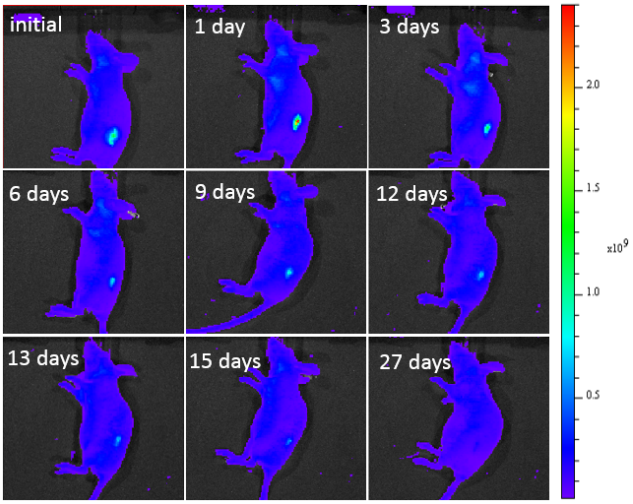


Figure 7**.** Sequential fluorescence images of the mouse after the injection of autofluorescent microspheres.

The temporal and spatial distribution of the fluorophores and the corresponding radiant intensity can be understood and estimated by a diffusive transport process. Small molecules or particle size smaller than 10 nm are able to diffuse and rapid renal clearance.[25] While, the microspheres were subjected to accumulation at the injection site and then firstly degraded, followed by the digestion through blood circulating system. Here a phenomenological model is proposed to fit the observed fluorescence data. It is assumed that the fluorophores liberated from BSA degradation diffuse in an axisymmetric and two-dimensional area. The radius of microspheres is around 1 to 3 μm, which is much larger than the size of the typical nanoparticles. We thus assume that the self-mobility of microspheres within the tissues is negligible. The amount of fluorophores upon injection or the radiant intensity is scaled by the maximum observable intensity, and the fluorophores are released at the center of the circular pattern. The continuous and transient distribution of the concentration or the scaled radiant intensity can therefore be described by the quasi-2D axisymmetric diffusion equation:

$$\frac{\partial c(r,t)}{\partial t} = D_{\text{eff}}\left(\frac{\partial^2 c}{\partial r^2} + \frac{1}{r}\frac{\partial c}{\partial r}\right) + [S_1(t) + S_2(t)][1.0 - H(r - r_0)] - \gamma c \qquad (2)$$

for $0 \le r < \infty,\ t \ge 0$, where c represents the local concentration or scaled radiant intensity, $r$ is radial coordinate, $t$ is time, $D_{\text{eff}}$ is an effective diffusivity of fluorophore molecules liberated from degraded BSA microparticles, the sink term $\gamma c(r,t)$ represents an assumed linear and concentration-dependent absorption within the tissue, where $\gamma$ is the absorption coefficient, $r_0$ is the estimated domain within which the microspheres are deposited upon the injection, $H$ is the Heaviside step function, and $S_1$ and $S_2$ are the transient parts of the source functions appear at short- and intermediate-time scales that determine the enhanced fluorophore intensity due to the relaxation of fluorescent self-quenching effect and the further release of fluorophores due to microsphere degradation, respectively. Both source terms are formulated by a product of Weibull and complementary Heaviside functions. The Weibull function describes the growth and attenuation of the fluorescent signal, while the complementary Heaviside step function determines the approximated initial deposition of the microspheres. The combined temporal and spatial contributions of the source terms can be adjusted to estimate the raise of radiant intensity at both short- and intermediate-time regimes (Figure 28a). The transient Weibull function is expressed as

$$S_i(t) = A_i \left[ \frac{k_i}{\lambda_i} \left( \frac{t}{\lambda_i} \right)^{k_i - 1} \cdot \exp\left( -\left( \frac{t}{\lambda_i} \right)^{k_i} \right) \right], \qquad (3)$$

where i=1, 2 to accommodate two source terms, the constant $A$ adjusts the overall strength of the source, and $k$ and $\lambda$ are the shape factor and scale parameter of the Weibull distribution, respectively. The corresponding boundary conditions of the diffusive system are

$$\partial c / \partial r = 0 \text{ at } r = 0;\ c \to 0 \text{ as } r \to \infty. \qquad (4)$$

The initial condition can be fitted by the following exponential function:

$$c(r,0) = \exp\left(-\alpha r^{\beta}\right) \quad \text{for} \quad 0 \le r < \infty, \qquad (5)$$

where the exponential power functions α and β provide an approximation of the starting radiant intensity. The above differential equation can be numerically solved by the standard RK4 time integration method and finite difference scheme.

Figure 8b shows the comparison of modelling and experimental results in terms of transient intensity versus time at location $r$ = 3.36 mm, approximately three times of the radial distance of the estimated initial deposition at $r_0$ = 1.0 mm. Note that experimentally the radiant intensity is obtained within the domain $0 \leq r \leq 3.36$ mm. Overall the modelling result is consistent with the radiant intensity observed. The effective diffusivity $D_{\text{eff}}$ is approximated as 4.32 $\text{mm}^2$/day, which is about 5% of the diffusivity of a small molecule in water $10^{-9}$ $\text{m}^2$/s. The radiant intensity from the short- to intermediate-time scales is well predicted by the addition of the phenomenological source and sink terms. Both source terms are shown in Figure 8a. The absorbing coefficient $\gamma$ is set to 0.05 $\text{day}^{-1}$, which appears to overestimate the decay of radiant intensity during the long-time process (Figure 8b), implying that the background intensity may still be effective after the absorption in tissue. Overall the underlying diffusive mechanisms are reasonably estimated by the physics-based model.

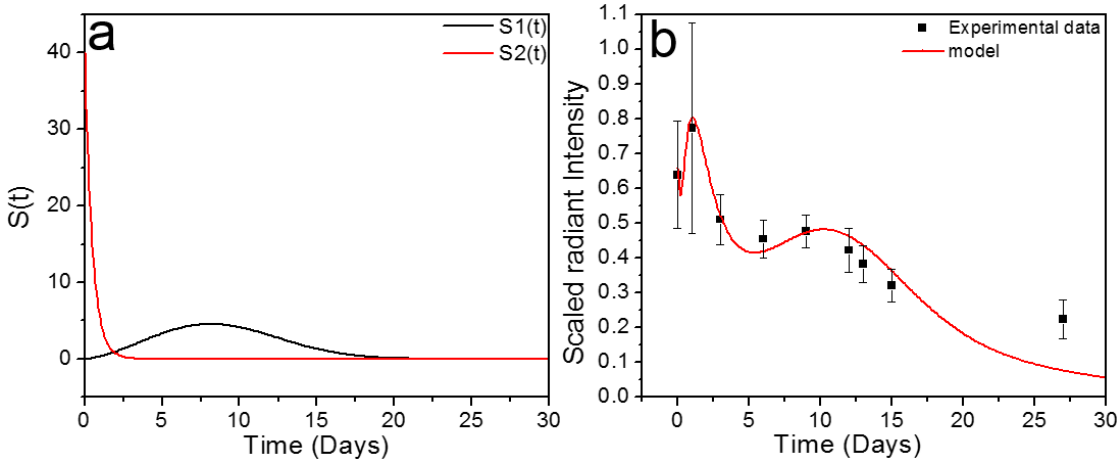


Figure 8. (a) The Weibull functions $S_1$ (red, short time) and $S_2$ (black, intermediate time) with scaled strength $A_1$ = 20, $A_2$= 45, shape factor $K_1$= 1.0, $K_2$= 2.5, and scale parameter $\lambda_1$ = 0.5 day and $\lambda_2$ = 10 day. (b) The comparison of

modelling and experimental results (n=3) on the transient distribution of fluorophore concentration at a location representing the diffusive process near the injection spot. The initial condition is fitted by $c(r,0) = \exp\left(-6\times10^{-3} r^{3.5}\right)$.

### 4.3.8 *In vivo* Biocompatibility study of the as-prepared autofluorescent BSA microspheres

After the autofluorescent microspheres were fully cleared by the blood circulate system, tissue histology was performed for the *in vivo* biocompatibility evaluation. For the skin tissue surrounding the injection spot (Figure 9 a), the tissue slide has a moderate to marked hyperkeratosis and spreading into many of the hair follicles. Mild hyperplasia of the epidermis has been observed in some areas of the hyperkeratosis. There is no inflammation evidence in the epidermis, dermis or subcutaneous tissues or muscle layers. Also, no significant lesions have been found in kidney (Figure 9 b), pancreas (Figure 9c) and liver (Figure 9d). Based on the histology study, it is demonstrated that as-prepared autofluorescent BSA microspheres exhibit good *in vivo* biocompatibility.

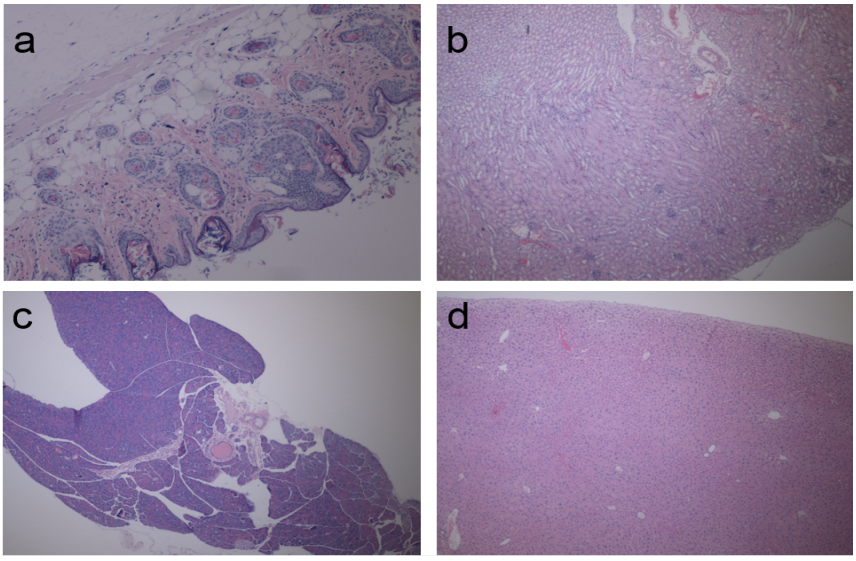


Figure 9. Histological analysis results: (a) Skin tissue image (100 ×), (b) Kidney tissue image (40 ×), (c) Pancreas tissue image (40×, and (d) Liver tissue image (40×).

## *4.4 Conclusion*

Autofluorescent BSA microspheres were prepared through a facile and low-cost route including a high-speed dispersion of BSA in cross-linking solution followed by spray drying. According to the studies of UV-vis spectra and fluorescence emission spectra, the fluorogenic origin of BSA microspheres has been discussed and proposed to the best of our knowledge. The biocompatibility and biodegradability of the as-prepared autofluorescent BSA microspheres were also demonstrated through extensive *in vitro* and *in vivo* studies based on the cytotoxicity test on the A549 cancer cells and tissue histological analysis, respectively. More interestingly, as-prepared microspheres were applied for convenient and non-invasive tracking of the biodegradation of injected autofluorescent BSA microspheres in mouse model based on time-dependent fluorescence images of the mice and the experimental data are in good agreement with the proposed diffusive model. All these studies indicate that the as-developed protein microspheres exhibiting good biocompatibility, biodegradability, and unique autofluorescence hold great promise in a variety of biomedical applications.

**Reference**


1. Volodkin, D. V., von Klitzing, R. and Möhwald, H. (2010) Pure protein microspheres by calcium carbonate templating. Angewandte Chemie, **122,** 9444-9447.
2. Sivadas, N., O'Rourke, D., Tobin, A., Buckley, V., Ramtoola, Z., Kelly, J. G., Hickey, A. J. and Cryan, S.-A. (2008) A comparative study of a range of polymeric microspheres as potential carriers for the inhalation of proteins. International journal of pharmaceutics, **358,** 159-167.
3. Wei, W., Wang, L.-Y., Yuan, L., Wei, Q., Yang, X.-D., Su, Z.-G. and Ma, G.-H. (2007) Preparation and application of novel microspheres possessing autofluorescent properties. Advanced Functional Materials, **17,** 3153.
4. Hanes, J., Chiba, M. and Langer, R. (1995) Polymer microspheres for vaccine delivery. ed. Springer.
5. Suh, J.-K. F. and Matthew, H. W. (2000) Application of chitosan-based polysaccharide biomaterials in cartilage tissue engineering: a review. Biomaterials, **21,** 2589-2598.
6. Liang, H.-F., Hong, M.-H., Ho, R.-M., Chung, C.-K., Lin, Y.-H., Chen, C.-H. and Sung, H.-W. (2004) Novel method using a temperature-sensitive polymer (methylcellulose) to thermally gel aqueous alginate as a pH-sensitive hydrogel. Biomacromolecules, **5,** 1917-1925.
7. Latha, M., Lal, A., Kumary, T., Sreekumar, R. and Jayakrishnan, A. (2000) Progesterone release from glutaraldehyde cross-linked casein microspheres: in vitro studies and in vivo response in rabbits. Contraception, **61,** 329-334.
8. McShane, M. J., Russell, R. J., Pishko, M. V. and Coté, G. L. (2000) Glucose monitoring using implanted fluorescent microspheres. Engineering in Medicine and Biology Magazine, IEEE, **19,** 36-45.

9. Langer, R. and Peppas, N. A. (2003) Advances in biomaterials, drug delivery, and bionanotechnology. AIChE Journal, **49,** 2990-3006.
10. Luchtel, D., Boykin, J., Bernard, S. and Glenny, R. (1998) Histological methods to determine blood flow distribution with fluorescent microspheres. Biotechnic & histochemistry, **73,** 291-309.
11. Fitzgerald, P., Hadgraft, J., Kreuter, J. and Wilson, C. (1987) A γ-scintigraphic evaluation of microparticulate ophthalmic delivery systems: liposomes and nanoparticles. International journal of pharmaceutics, **40,** 81-84.
12. Taylor, J. R., Fang, M. M. and Nie, S. (2000) Probing specific sequences on single DNA molecules with bioconjugated fluorescent nanoparticles. Analytical Chemistry, **72,** 1979-1986.
13. Yu, L. (2001) Amorphous pharmaceutical solids: preparation, characterization and stabilization. Advanced drug delivery reviews, **48,** 27-42.
14. Vehring, R. (2008) Pharmaceutical particle engineering via spray drying. Pharmaceutical research, **25,** 999-1022.
15. Boissiere, C., Grosso, D., Chaumonnot, A., Nicole, L. and Sanchez, C. (2011) Aerosol route to functional nanostructured inorganic and hybrid porous materials. Advanced Materials, **23,** 599-623.
16. Cheow, W. S., Li, S. and Hadinoto, K. (2010) Spray drying formulation of hollow spherical aggregates of silica nanoparticles by experimental design. Chemical Engineering Research and Design, **88,** 673-685.
17. Xu, H., Tan, Z., Abe, H. and NAITO, M. (2011) Microcapsule assembly of single-walled carbon nanotubes from spray-dried hollow microspheres. Journal of the Ceramic Society of Japan, **119,** 180-184.
18. Maas, S. G., Schaldach, G., Littringer, E. M., Mescher, A., Griesser, U. J., Braun, D. E., Walzel, P. E. and Urbanetz, N. A. (2011) The impact of spray drying outlet temperature on the particle morphology of mannitol. Powder Technology, **213,** 27-35.
19. Carné-Sánchez, A., Imaz, I., Cano-Sarabia, M. and Maspoch, D. (2013) A spray-drying strategy for synthesis of nanoscale metal–organic frameworks and their assembly into hollow superstructures. Nature chemistry, **5,** 203-211.
20. Gavini, E., Sanna, V., Juliano, C. and Giunchedi, P. (2003) Compressed biodegradable matrices of spray-dried PLGA microspheres for the modified release of ketoprofen. Journal of microencapsulation, **20,** 193-201.
21. Sun, X., Ma, X., Kumar, C. V. and Lei, Y. (2014) Protein-based sensitive, selective and rapid fluorescence detection of picric acid in aqueous media. Analytical Methods, **6,** 8464-8468.
22. Nimni, M. E., Cheung, D., Strates, B., Kodama, M. and Sheikh, K. (1987) Chemically modified collagen: a natural biomaterial for tissue replacement. Journal of Biomedical Materials Research, **21,** 741-771.
23. Lee, K., Choi, S., Yang, C., Wu, H.-C. and Yu, J. (2013) Autofluorescence generation and elimination: a lesson from glutaraldehyde. Chemical Communications, **49,** 3028-3030.
24. Ding, D., Li, K., Qin, W., Zhan, R., Hu, Y., Liu, J., Tang, B. Z. and Liu, B. (2013) Conjugated Polymer Amplified Far- Red/Near- Infrared Fluorescence from Nanoparticles with Aggregation- Induced Emission Characteristics for Targeted In Vivo Imaging. Advanced healthcare materials, **2,** 500-507.
25. Subia, B. and Kundu, S. (2013) Drug loading and release on tumor cells using silk fibroin–albumin nanoparticles as carriers. Nanotechnology, **24,** 035103.

# Chapter 5
# Integrated Experimental and Modeling Study of Enzymatic Degradation using Novel Autofluorescent BSA Microspheres

**Abstract**

Autofluorescent bovine serum albumin (BSA) hydrogel microspheres were prepared through spray-drying of glutaraldehyde cross-linked BSA nanoparticles, and then applied for proteinase K based degradation study in an aqueous solution. Experimental results and empirical models are presented to characterize the kinetics of BSA hydrogel microsphere degradation as well as the accompanied release of synthesized fluorophore. The BSA gel degradation dynamics is primarily controlled by the concentration of proteinase K within the Tris buffer. The coupling of swelling dynamics and the transient distributions of fluorophore are traced by confocal microscopy. The models are developed based on linear theory of elastic deformation coupled to the enzyme and fluorophore transport. The study has provided fundamental investigation of the degradation and release kinetics of protein-based materials, which can potentially be applied for dynamic and photostable tracking of relevant *in vivo* systems.

## *5.1 Introduction*

Biodegradation and biocompatibility are well known significant functionalities of synthetic biomaterials. [1, 2] Controlled material degradation further allows for sustained release designed for various biomedical applications. The advantages of controlled degradation are to avoid fast clearance and render further access to biological response along a desirable period of time. Specifically in tissue engineering, the materials are often to be degraded after serving as a temporary scaffold for cell therapy or tissue regeneration.[2] Among all materials, natural polymers such as polysaccharides and many other proteins have attracted lots of attentions ascribing to their biocompatibility, *in vivo* affinity to tissues and scaffolds, and controllable degradation properties [3-7]. More specifically, natural polymer based hydrogels have been widely explored in biomedical applications for drug delivery, medical diagnostics, biological tracking, or as personal care products [8-11]. Hydrogel can absorb a large amount of water and exhibit three-dimensional structure. Protein-based hydrogels are important biodegradable and biocompatible materials, primarily due to their intrinsic high affinity to tissues and enzymatic degradation properties. Hydrogels made of bovine serum albumin (BSA) have been extensively studied, attributing to its lower cost, good solubility and stability, and excellent ligand-binding accessibility and intrinsic fluorescence emission properties [12-15]. However, dynamic degradation of protein-based hydrogel matrix and the relevant transport mechanisms are not well understood. In this study, spray-dried BSA microspheres have been fabricated according to our previous study [15], which is applied here for further investigation on enzymatic degradation and the release of fluorophores.

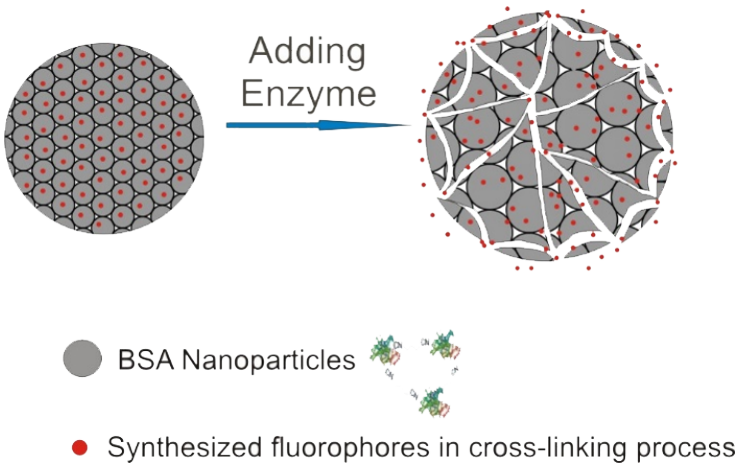


Figure 1: Schematic of enzymatic degradation and the release of photostable fluorophores. Proteinase K is added to the Tris buffer solution upon triggering the degradation process.

Figure 1 illustrates the problem in hand, a dynamic swelling and degrading autofluorescent hydrogel microsphere triggered by proteinase K in Tris buffer solution. The microspheres are about 2 to 4 μm, covalently immobilized on the surface of a petri dish. The enzymatic degradation of BSA gel results in swelling and diminishing of fluorescent intensity. Direct observation by confocal microscopy has shown that the BSA gel swelling is a continuous process, starting upon the addition of enzymes into the solution, continuously swelled, and then slowly degraded until all fluorescent signal diminishes. To characterize the swelling dynamics and simultaneous fluorophore release in detail, we present a side-by-side comparison of experimental results and diffusive-reactive species transport models. The transient fluorescent signals on each sectional plane of the hydrogel spheres were tracked intermittently using confocal laser scanning microscope (CLSM). The enzyme and fluorophore transport equations are coupled with the empirical THB hydrogel swelling model [16, 17]. The collective diffusivity represents a combined shear and bulk elasticity as well as the resistance coefficient for the relative motion between solvent and the gel network. The overall process is likely controlled by three factors: the collective diffusivity for gel swelling, self diffusivity of enzyme molecules

within the gel domain, and the apparent degradation rate constant of the fluorophores for the first-order irreversible reaction.

## *5.2 Experiments*

### 5.2.1 Materials and synthesis of BSA microspheres

BSA, (3-Aminopropyl) trimethoxysilane (APTMS), sodium hydroxide, and tris-hydrochloride were purchased from Sigma, Glutaraldehyde, proteinase k solution (20 mg/mL, RNA grade, Catalog No. 25530049), calcium chloride, and cover glass were purchased from Fisher Scientific. BSA microspheres were fabricated according to our previous study [15]. Briefly, BSA solution firstly added in fast speed glutaraldehyde crosslinking dispersion to form BSA nanoparticles dispersion, followed by spray-drying process, resulting in green and red autofluorescent microspheres. SEM image shows the surface morphology of as-synthesized microspheres (Figure 2A).

### 5.2.2 Tracking enzymatic degradation of BSA microspheres

Prior to imaging, cover glass was first treated by 1 M sodium hydroxide for half an hour, and then it was treated with APTMS vapor overnight, resulting in primary amine groups on the surface of cover glass. This process enabled the covalent anchoring of as-synthesized BSA microspheres, as aldehyde groups on the surface of BSA microspheres, which is indicated by the FTIR result in our previous study [15]. 120 μL spray-dried microspheres dispersion in DI water with a concentration of 0.5 mg/mL were added on the treated cover slides, and waited for 1 hour. Then the cover slides were washed by DI water for several times to remove unbounded microspheres. After that, 200 μL DI water were added in the cover slides overnight, enabling microspheres to swell until equilibration. Proteinase K solution was diluted for different concentrations in Tris buffer at pH 7, with 10 mM $Ca^{2+}$ in the solution. Upon the addition of 200

μL of the diluted proteinase K solution in the cover slides containing bounded microspheres and 200 μL DI water (with $Ca^{2+}$ final concentration at 5 mM), enzymatic degradation of BSA microspheres and the release of fluorophores were tracked by Nikon A1R confocal laser scanning microscope. Transient fluorescent images on each sectional plane were acquired in certain time period immediately after the addition of enzyme solution. Figures 2B and 2C demonstrate the confocal images scanned through the middle section of the spheres. Upon addition of proteinase K, the individual sphere ranges from radius 1 to 3 μm goes through swelling and degradation process till the fluorescent signal diminishes (Fig. 2C).

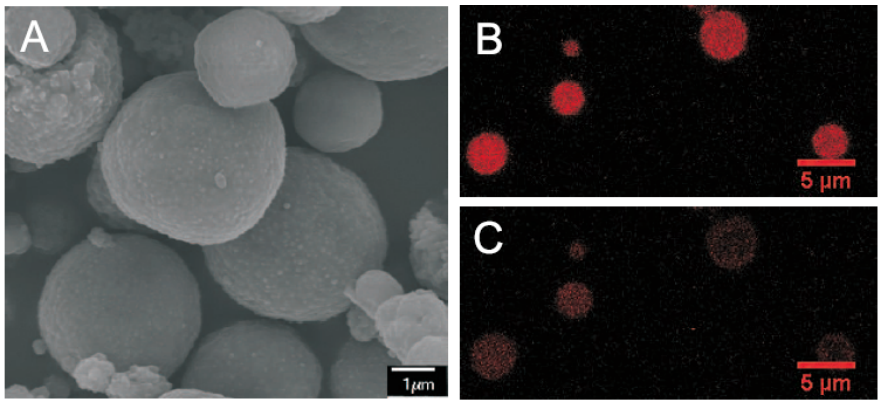


Figure 2: (A) SEM image of the spray-dried microspheres. (B, C) Confocal images of randomly deposited BSA hydrogel microspheres taken at the initial and end stages of the degradation process.

### 5.2.3 Image analysis

Image analysis were performed by using *Image J* software. At each time point, the area values of single microspheres on each z plane were analyzed in order to identify the middle section. The circular region of interests with different radius were selected, and then transient local fluorescence intensities were collected.

## *5.3 Empirical Models*

A few assumptions are made to simplify the analysis. Upon addition of proteinase K, it diffuses immediately and is assumed uniformly distributed in the buffer solution. There exists plenty of proteinase K within the buffer, and thus the depletion of which due to permeation into the hydrogel is negligible. The gel swelling is assumed a diffusive-like elastic deformation process and can be formulated by the THB model [17]. The enzyme diffusivity within the hydrogel and the first-order reaction rate coefficient for BSA degradation are assumed constant over the whole process. Therefore, the enzyme and fluorophore transport equations are coupled to the swelling momentum equation through the gel configuration or local material displacement. The first approximation we proposed here is applicable to the beginning stage of the degradation, and is not for later stage when disintegration appears. The modeling framework is described in detail as follows.

**5.3.1 Swelling of BSA hydrogel**

The THB model that describes the swelling dynamics is developed from the linear elastic theory by assuming that gel swelling is under quasi-equilibrium condition, and the friction due to the relative motion between solvent and the gel network can be treated as a body force. The constitutive model for a linear elastic deformation can be defined as

$$\sigma = G\,(\nabla u + \nabla u^T) + \lambda\delta(\nabla \cdot u)\,, \quad (1)$$

Where $\sigma$ is stress tensor, $u$ is the displacement vector, $G$ is the shear modulus, $\lambda$ is Lame's first parameter, which is associated with bulk modulus of elasticity K = λ+2G/3, and $\delta$ is the Kronecker delta. The general momentum equation for linear elastic deformation thus can be expressed as

$$\rho\frac{\partial^2 u}{\partial t^2} = G\nabla^2 u + (\lambda + G)\nabla(\nabla \cdot u) + F_b, \quad (2)$$

where $\rho$ is mass density, $t$ is time, and Fb is the body force assumed to be the resistance force proportional to the relative moving velocity between solvent and the gel net- work, expressed $F_b = -f(\partial u/\partial t)$, where $f$ is the friction coefficient. The THB model [16, 17] is a quasi-steady approximation of the momentum equation, in which balances the inward resistance and outward osmotic force, expressed as

$$\frac{\partial u}{\partial t} \cong \frac{G}{f}\nabla^3 u + \frac{\left(K+\frac{G}{3}\right)}{f}\nabla(\nabla \cdot u). \quad (3)$$

Assuming that the BSA hydrogel microspheres remain spherical during the swelling process, the above equation reduces to one-dimensional formulation:

$$\frac{\partial u_r}{\partial t} = D_{\text{swell}}\frac{\partial}{\partial r}\left\{\frac{1}{r^2}\frac{\partial(r^2 u_r)}{\partial r}\right\}, \quad (4)$$

where $r$ is the radial variable, $u_r$ is the displacement in radial direction, and $D_{\text{swell}} = (K+4G/3)/f$ is the apparent or collective diffusion coeffcient for the swelling process. The initial condition is defined at the fully swollen state. The radical displacement $u_r$ at time $t$=0 is obtained by assuming uniform osmotic stress within the hydrogel, $\sigma_{rr} = \pi_0$, which leads to

$$u_r(r, 0) = \Delta R_0 \frac{r}{R_{max}}, \quad (5)$$

Where $\Delta R_0 = \pi_0 R_{max}/(3K)$, $R_{\max}$ is the maximum radius of the gel at equilibrium, and $\Delta R_0$ is the total increase of the gel size. The initial size before swelling is $R_0 = R_{\max}$-$R_0$. The corresponding boundary conditions are zero displacement at the center point and vanishing normal stress $\sigma_{rr}$ at $r = R_{\max}$. The analytical solution of the eigenvalue problem given by Tanaka et al. [16, 17] therefore can be expressed as a series form

$$u_r(r', t) = 6\Delta R_0 \sum_{n=1}^{\infty} \frac{(-1)^n}{n\pi}\left\{\frac{\cos(\beta_n r')}{\beta_n r'} - \frac{\sin(\beta_n r')}{(\beta_n r')^2}\right\} \times \exp\left(-D_{swell}\beta_n^2 t\right), \quad (6)$$

where $\beta_n = n\pi/R_{max}$ are the eigenvalues with $n$ = 1, 2,...∞. The symbol prime indicates the Lagrangian approach for the location of tagged material element at $t \rightarrow \infty$, and thus the location of this tagged material within the swelling gel at time $t$ can be defined as

$$r(r',t) = r' - u_r(r',t). \quad (7)$$

The moving boundary is located at $r(R_{max}, t) = R_{max}\text{-}u_r(R_{max}, t)$. The material moving velocity, thus is

$$v(r,t) = -\frac{\partial u(r',t)}{\partial t}. \quad (8)$$

which is used as the Eulerian velocity field in the transport equation given in Section 5.3.2 and 5.3.3.

**5.3.2 Diffusion of Proteinase K**

The diffusion of proteinase K from the PBS buffer solution into the swelling BSA hydrogel is a moving boundary problem. First we consider a simple Fickian diffusion equation with an assumed uniform diffusivity,

$$\frac{\partial E}{\partial t} = D_e \nabla^2 E, \quad (9)$$

where $E$ indicates the enzyme concentration, and $D_e$ is the apparent enzyme diffusivity within the swelling hydrogel. For a spherically symmetric case, the above equation can be simplified to

$$\frac{\partial E(r,t)}{\partial t} = D_e \left( \frac{\partial^2 E}{\partial r^2} + \frac{2}{r}\frac{\partial E}{\partial r} \right), \quad (10)$$

for the gel domain, $0 \leq r \leq R(t)$, and time $t \geq 0$. The outer boundary of the BSA gel is defined by the time-dependent radius $R(t)$, which can be formulated as

$$R(t) = R_{max} - u_r(R_{max}, t). \quad (11)$$

Assuming the enzyme concentration in the buffer solution remains the same, the corresponding initial and boundary conditions for the enzyme transport are

$$E(r,0) = 0 \quad \text{for} \quad 0 \le r \le R_0, \quad (12)$$
$$\partial E/\partial r = 0 \quad \text{at} \quad r = 0,$$
$$E = E_b \quad \text{at} \quad r = R(t),$$

where $E_b$ is the enzyme concentration in the bulk, and $r = R(t)$ is a moving boundary condition. The moving boundary problem can be solved by a coordinate transformation to immobilize the outer boundary. Considering new temporal and spatial variables:

$$\tau = t \quad \text{and} \quad \eta = \frac{r}{R(t)}, \quad (13)$$

where $\tau \geq 0$ and $0 \leq \eta \leq 1$. The transformed diffusion equation can be reformulated as

$$\frac{\partial E}{\partial \tau} = \frac{D_e}{R^2}\frac{\partial^2 E}{\partial \eta^2} + \left(\frac{2D_e}{\eta R^2} + \frac{\eta \dot{R}}{R}\right)\frac{\partial E}{\partial \eta}, \quad (14)$$

where the interfacial moving velocity, $\dot{R}(\tau) = \dot{R}(t) = \partial u(R_{max}, t)/\partial t$, is given by the analytical displacement function (eq. 8). The corresponding initial and boundary conditions now become

$$E(\eta,0) = 0 \quad \text{for} \quad 0 \le \eta \le 1,$$
$$\partial E/\partial \eta = 0 \quad \text{at} \quad \eta = 0, \quad (15)$$
$$E = E_b \quad \text{at} \quad \eta = 1.$$

For given analytical solutions for $R(t)$ and $\dot{R}(t)$ from the swelling dynamics, the transformed enzyme equation can be solved numerically by a standard finite difference method with fixed domain and mesh points.

**5.3.3 Degradation of BSA gel and diminishing fluorescent intensity**

The degradation of BSA hydrogel microsphere can be observed from the autofluorescent BSA and the released fluorophore through confocal microscopy. The diminishing fluorescent intensity implies that BSA degradation is caused by the diffusion of proteinase K into the matrix from the bulk solution. Assuming that the self diffusivity and stress-induced diffusion of BSA network are negligible during the swelling process, the concentration of the autofluorescent BSA is essentially affected by the gel expansion, swelling-induced advection, and the first-order

degradation reaction. The reaction is assumed proportional to the concentrations of proteinase K and the undegraded BSA. Meanwhile, the BSA degradation will set the combined fluorophore peptide free, so that the fluorophore can diffuse outward into the buffer. The apparent fluorescent intensity is contributed by superposing the concentrations of undegraded BSA and the fluorophore, written as

$$I(r,t) = B(r,t) + F(r,t), \quad (16)$$

Where $I$ indicates the fluorescent intensity, $B$ and $F$ represent the concentrations of autofluorescent BSA and free fluorophore, respectively. The BSA transport can be phenomenologically simulated by the advection-reaction equation:

$$\frac{\partial B}{\partial t} + \nabla \cdot (Bv) \approx -\alpha EB, \quad (17)$$

Where $I$ indicates the fluorescent intensity, $B$ and $F$ represent the concentrations of autofluorescent BSA and free fluorophore, respectively. The BSA transport can be phenomenologically simulated by the advection-reaction equation:

$$\frac{\partial B(r,t)}{\partial t} \approx -\frac{B}{r^2}\frac{\partial}{\partial r}(r^2 v_r) - v_r\frac{\partial B}{\partial r} - \alpha EB, \quad (18)$$

for $0 \le r \le R(t)$ and $t \ge 0$. The Eulerian velocity field in radial direction, $v_r$ is the time derivative of the displacement function, expressed as

$$v_r(r,t) = -\frac{\partial u_r(r',t)}{\partial t}. \quad (19)$$

Numerically the Lagrangian materials location $r'$ can be found by computing the root of the following algebraic equation based on the field location $r$ and time $t$,

$$r'(t) - u_r(r',t) - r(t) = 0. \quad (20)$$

The corresponding initial and boundary conditions for the traveling wave-like equation are

$$\begin{aligned} &B(r,0) = B_0 \quad \text{for} \quad 0 \le r \le R_0, \\ &B(r,0) = 0 \quad \text{for} \quad r > R_0, \\ &\text{and} \quad \partial B/\partial r = 0 \quad \text{at} \quad r = 0, \end{aligned} \quad (21)$$

Similar to proteinase K, the diffusion of fluorophore from the hydrogel to the buffer solution can be computed with an additional source term due to the production of fluorophore from BSA degradation, written as

$$\frac{\partial F(r,t)}{\partial t} = D_f\left(\frac{\partial^2 F}{\partial r^2} + \frac{2}{r}\frac{\partial F}{\partial r}\right) + \alpha EB, \quad (22)$$

For the gel domain $0 \le r \le R\ (t)$ and time $t \ge 0$, where $D_f$ represents the apparent fluorophore diffusivity within the hydrogel. The corresponding initial and boundary conditions for the fluorophore transport are

$$\begin{aligned} &F(r,0) = F_b \quad \text{for} \quad 0 \le r \le R_0, \\ &\partial F/\partial r = 0 \quad \text{at} \quad r = 0, \\ &\text{and} \quad F = F_b \quad \text{at} \quad r = R(t), \end{aligned} \quad (23)$$

Where $F_b$ is the background fluorescent intensity observed from experiments. Similarly through coordinate transformation (eq.13), the fluorophore diffusion equation reduces to

$$\frac{\partial F}{\partial \tau} = \frac{D_f}{R^2}\frac{\partial^2 F}{\partial \eta^2} + \left(\frac{2D_f}{\eta R^2} + \frac{\eta \dot{R}}{R}\right)\frac{\partial F}{\partial \eta} + \alpha E(\eta R, t)B(\eta R, t) \quad (24)$$

for $0 \le \eta \le 1$ and $\tau \ge 0$, and the equation is coupled with the gel swelling dynamics through the moving boundary and both enzyme and BSA concentrations. The corresponding initial and boundary conditions are

$$\begin{aligned} &F(\eta,0) = F_b \quad \text{for} \quad 0 \le \eta \le 1, \\ &\partial F/\partial \eta = 0 \quad \text{at} \quad \eta = 0, \\ &\text{and} \quad F = F_b \quad \text{at} \quad \eta = 1. \end{aligned} \quad (25)$$

In summary, the three species transport equations along with the THB gel swelling model and the complementary initial and boundary conditions are proposed to resolve the enzyme reaction kinetics, which leads to degradation of autofluorescent BSA hydrogel microspheres.

## *5.4 Results and Discussions*

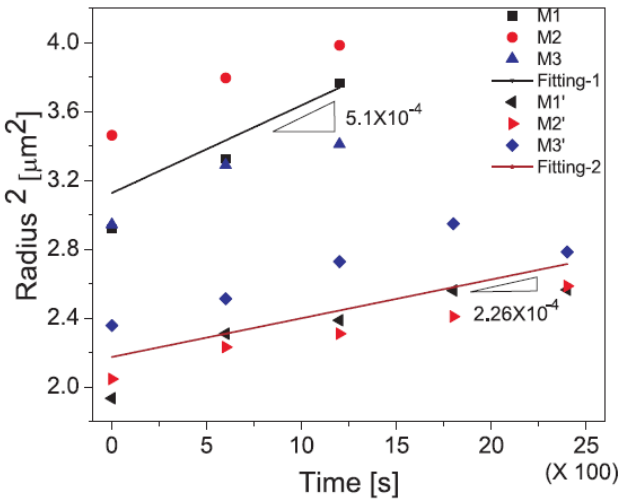


Figure 3. Square of the apparent radius versus time under low ([E]=0.05 mg/mL) and high ([E]=0.5 mg/mL) enzyme concentrations. The calcium concentration [$Ca^{2+}$]=5.0 mM. M1-M2-M3 and M1'-M2'-M3' are the selected microspheres under high- and low-enzyme conditions, respectively, and the lines of Fitting-1 and Fitting-2 indicate the mean values of $D_{swell}$ approximately $5.1\times10^{-4}$ and \$$2.26\times10^{-4}$ respectively.

Experimental tests were conducted based on two enzyme conditions: 0.5 and 0.05 mg/mL proteinase K in Tris buffer with 5 mM [$Ca^{2+}$]. As reported, [$Ca^{2+}$] can significantly increase the activity and stability of proteinase K. Thus, calcium ion was added to enable degradation of the as-synthesized microspheres within one hour to facilitate the monitoring of degradation using confocal microscope. The collective diffusivity $D_{swell}$ is estimated by the slope of the radius square versus time, $R^2(t)/t$, which was tracked for each swelling BSA hydrogel microsphere. The estimated $D_{swell}$ almost remains the same throughout the swelling dynamics, which is phenomenologically approximated by a constant collective diffusivity near the initial stage of the swelling (without defragmentation). Figure 3 shows the extracted experimental data from the swelling and possibly softening microspheres due to enzymatic degradation. The uniform osmotic pressure is used as an initial condition, and the transient dynamics is controlled by the collective diffusivity, which represents the overall effect of bulk modulus, shear modulus, and the friction coefficient. Within the time range of interest, not far from the initial stage of degradation,

$D_{swell}$ is about a constant and the diffusive type deformation well describes the dynamics as in the linear elastic regime. The collective diffusivity appears to be about two times higher as the enzyme concentration increases from 0.05 to 0.5 mg/mL. Here we neglect the small variation of $D_{swell}$ for various microspheres and select a mean value for the theoretical analysis. The modeling parameters include: (i) BSA hydrogel, $D_{swell} \approx 5.1 \times 10^{-4} \mu m^2/s$ (high enzyme) and $D_{swell} \approx 2.26 \times 10^{-4} \mu m^2/s$ (low enzyme), extracted from Figure 3, (ii) proteinase K and fluorophore, both $D_e$ and $D_f$ are assumed 100 times of $D_{swell}$ for their corresponding high and low enzyme cases, and this guess is at least three orders of magnitude lower than the small molecules with similar size in an aqueous solution, and (iii) degradation rate constant $\alpha = 10^{-3}\ s^{-1}$ and $5 \times 10^{-4}\ s^{-1}$ for the high and low enzyme cases, respectively, are adjusted numerically from sensitivity tests to match the observed fluorescent data as a best-effort approximation.

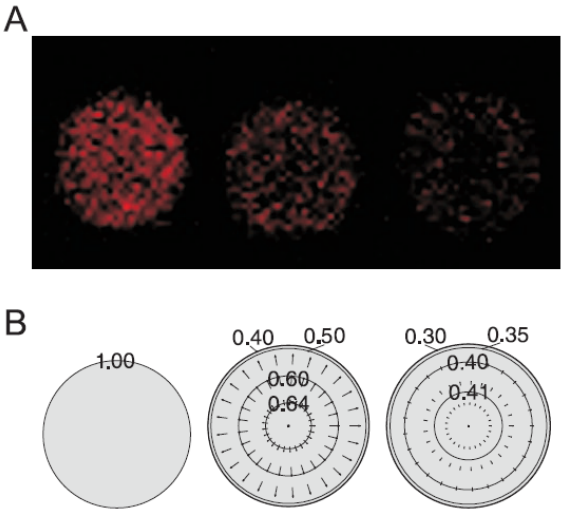


Figure 4. (A) Sequential confocal images of the swelling BSA hydrogels taken at 0, 20, and 40 minutes for [E]=0.05 mg/mL and $[Ca^{2+}]$=5 mM. (B) The corresponding modeling results, showing the deformation dynamics with velocity vectors and the scaled fluorophore concentration contours within the gel.

Figure 4 shows side-by-side comparison of sequential confocal images with the modeling results during the swelling and degradation process. Each fluorescent intensity map is obtained from

only the middle section of the selected microsphere (Figure 4A). The computed velocity field in each map represents the localized swelling dynamics at different material points, which is superposed by scaled fluorophore concentration contours (Figure 4B). The spherically symmetric model has successfully captured several important features of the dynamic process: (i) diffusion-like elastic expansion of the hydrogel, (ii) the BSA degradation reaction kinetics, and (iii) the overall florescent intensity contributed by the remaining (undegraded) BSA and free fluorophore molecules. The overall expansion in terms of linear dimension is limited to about 25% during the swelling process. Further degradation for both high and low enzyme cases causes fragmentation of the gels, which is not included in the theoretical model. The higher concentration gradient appears near the edge of the spheres (Figure 4B). The concentration gradient drives the removal or depletion of the fluorophores and decays as the gel progressively swells and degrades.

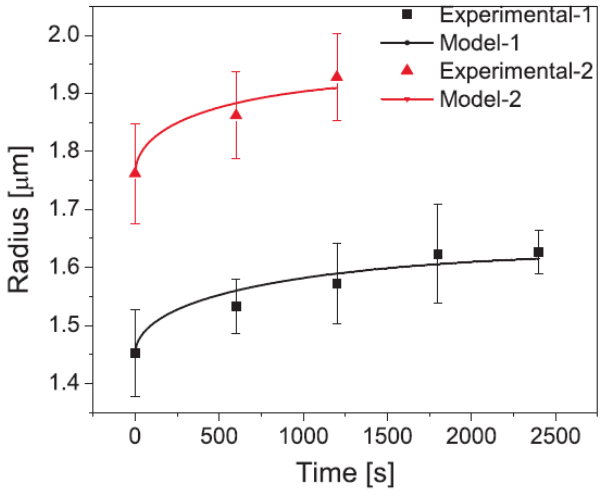


Figure 5. The two data sets are corresponding to high (Experimental- and Model-) and low (Experimental- and Model-2) enzyme conditions, respectively. The continuous curves are modeling results.

Figure 5 shows the transient radius of the gels compared with the modeling results. The data points are obtained by tracking the material points initially located at the outer boundary of the gels. As the BSA hydrogel degrades continuously, the maximum radius $R_{max}$ at the almost fully

swollen state is determined by setting *Image J* circularity value at 0.3 to 1.0. Overall the transient experimental results agree very well with the modeling results (continuous curves) using the input of the mean collective diffusivity. Because the dynamics is directly observed from the confocal experiment, it is reasonable to extract $D_{swell}$ first from the configuration, and then estimate the reaction constant and other diffusivities by matching the computational results with the distribution of fluorescent intensity.

Figure 6 compares the scaled transient fluorescent intensity corresponding to relatively low (Figure. 6A) and high (Figure. 6B) enzyme concentration distributions. A uniform concentration and fluorescent intensity are assumed for the initial BSA content within the microspheres. The background intensity is set to $F_b$=0.1 and remains the same throughout the process. The swelling dynamics and the moving boundary are obvious and qualitatively comparable with modeling results. The enzyme concentration in the BSA microsphere achieves its maximum within 10 to 50 seconds for all testing cases, which is much faster than the characteristic time scale for the gel swelling process. This implies that the BSA degradation is not diffusion-limited by the enzyme transport, but by the degradation reaction kinetics. The diffusion of fluorophore is also fast compared with swelling and degradation, and thus the local fluorophore concentration remains quite uniform within the gel during the process. Therefore, the change of local fluorescent intensity is mainly due to the degradation of BSA gel. Overall the empirical model has captured the transient phenomena including gel swelling dynamics and BSA degradation in terms of the fluorescent intensity, except that near the center part of the hydrogel, where the significantly weakened intensity may be due to the crystalized salt content that is optically opaque. The salt content may come from the spray-dried process.

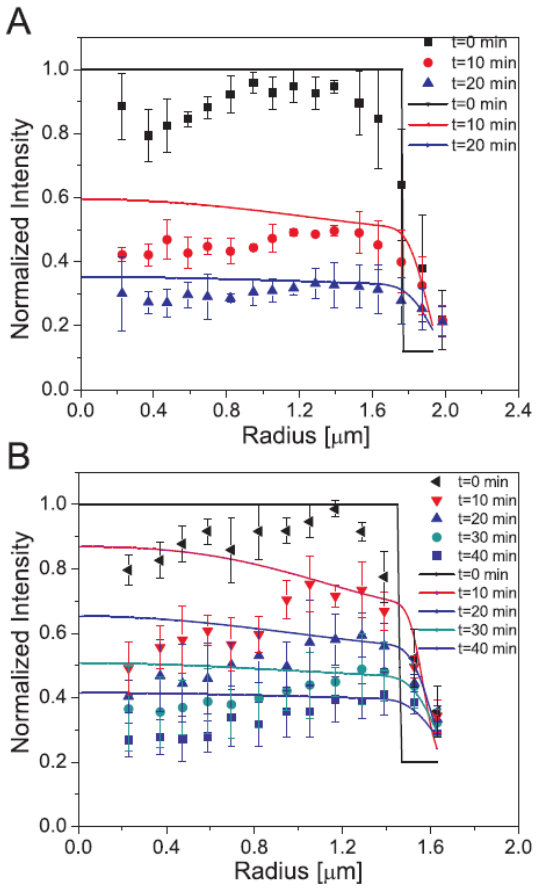


Figure 6. The transient local fluorescent intensity versus time for test cases with relatively high (A) and low (B) enzyme concentrations. Experimental data (symbol) are side-by-side compared with the corresponding modeling results (solid lines).

In summary, during the process the spray-dried BSA hydrogel microspheres are enzymatically degraded by proteinase K in an aqueous solution, and the role of proteinase K is quantified using the phenomenological transport model, which has revealed the key features of the swelling dynamics and BSA degradation kinetics via the release of the fluorophore. This study can potentially be applied for dynamic and photostable tracking in many protein-based scaffolds, and for the study of *in vivo* fate upon enzymatic degradation in cells or tissues.

## *5.5 Conclusion*

A side-by-side comparison of experimental and modeling results is presented to characterize the enzymatic degradation and fluorophore release kinetics of autofluorecent BSA hydrogel microspheres. The investigation provides a better understanding of protein-based hydrogel matrix, and can potentially be applied for various biomedical applications such as fluorescent imaging and controlled drug delivery.

**Reference**


1. R. Langer and J.P. Vacanti, Tissue engineering, *Science*, 1993, **260**, 920-926.
2. M.P. Lutolf and J.A. Hubbell, Synthetic biomaterials as instructive extracellular microenvironments for morphogenesis in tissue engineering, *Nat. Biotechnol.*, 2005, **23**, 47-55.
3. J.-K.F. Suh and H.W.T. Matthew, Application of chitosan-based polysaccharide biomaterials in cartilage tissue engineering: a review, *Biomaterials*, 2000, **21**, 2589-2598.
4. H.-F. Liang, M.-H. Hong, R.-M. Ho, C.-K. Chung, Y.-H. Lin, C.-H. Chen, and H.-W. Sung, Novel method using a temperature-sensitive polymer (methylcellulose) to thermally gel aqueous alginate as a pH-sensitive hydrogel, *Biomacromolecules*, 2004, **5**, 1917-1925.
5. M.S. Latha, A.V. Lal, T.V. Kumary, R. Sreekumar, and A. Jayakrishnan, Progesterone release from glutaraldehyde cross-linked casein microspheres: in vitro studies and *in vivo* response in rabbits, *Contraception*, 2000, **61**, 329-334.
6. R. Langer and N.A. Peppas, Advances in biomaterials, drug delivery, and bionanotechnology, *AIChE J.*, 2003, **49**, 2990-3006.
7. N.A. Peppas, J.Z. Hilt, A. Khademhosseini, and R. Langer, Hydrogels in biology and medicine: from molecular principles to bionanotechnology, *Adv. Mater.*, 2006, **18**, 1345-1360.
8. D.V. Volodkin, R. von Klitzing, and H. Mhwald, Pure protein microspheres by calcium carbonate templating, *Angew. Chem. Int. Ed.*, 2010, **49**, 9258-9261.
9. N. Sivadas, D. O'Rourke, A. Tobin, V. Buckley, Z. Ramtoola, J.G. Kelly, A.J. Hickey, and S.-A. Cryan, A comparative study of a range of polymeric microspheres as potential carriers for the inhalation of proteins, *Int. J. Pharmaceut.*, 2008, **358**, 159-167.
10. W. Wei, L.-Y. Wang, L. Yuan, Q. Wei, X.-D. Yang, Z.-G. Su, and G.-H. Ma, Preparation and application of novel microspheres possessing auto°uorescent properties, *Adv. Funct. Mater.*, 2007, **17**, 3153-3158.
11. J. Hanes, M. Chiba, and R. Langer, Polymer microspheres for vaccine delivery, *Vaccine Design*, 15 Springer, 1995. 384-412.
12. W. Qin, D. Ding, J. Liu, W.Z. Yuan, Y. Hu, B. Liu, B.Z. Tang, Biocompatible nanoparticles with aggregation-induced emission characteristics as far-red/near-infrared °uorescent bioprobes for in vitro and in vivo imaging applications, *Adv. Funct. Mater.*, 2012, **22**, 771- 779.
13. I.K. Deshapriya, B.S. Stromer, A. Pattammattel, C.S. Kim, R. Iglesias-Bartolome, L. Gonzalez-Fajardo, V. Patel, J.S. Gutkind, X. Lu, and C.V. Kumar, Fluorescent, bioactive protein nanoparticles (prodots) for rapid, improved cellular uptake, *Bioconjugate Chem.*, 2015, **26**, 396-404.
14. J. Chen, Q. Dong, X. Ma, T.-H. Fan, Y. Lei, Repetitive biomimetic self-healing of Ca2+- induced nanocomposite protein hydrogels, *Scienti¯c Reports*, 2016, **6**, 30804.
15. X. Ma, T. Wang, D. Song, D. Hargrove, Q. Dong, Z. Luo, J. Chen, X. Lu, Y. Luo, T.-H. Fan,Y. Lei, Protein microspheres with unique green and red auto°uorescence for non-invasively tracking and modeling their in vivo biodegradation, *ACS Biomater. Sci. Eng.*, 2016, **2**, 954- 962.

16. T. Tanaka, L.O. Hocker, and G.B. Benedek, Spectrum of light scattered from a viscoelastic gel, *J. Chem. Phys.*, 1973, **59**, 5151-5159.
17. T. Tanaka, and D.J. Fillmore, Kinetics of swellingof gels, *J. Chem. Phys.*, 1979, **70(03)**, 1214-1218. 16

# Chapter 6
# Side Project- Autofluorescent Nanoparticles for the Detection of Malaria-infection Indicator


**Abstract**

Malaria plagues seriously in some tropical areas of the world, partly due to the lack of low-cost, sensitive diagnostic tools accessible. A simple way for fast monitoring malaria infection is to detect the elevated level of heme in the blood serum. Albumins are widely used in bioengineering due to their low-cost, good biocompatibility, and biodegradability. Herein we report that glutaraldehyde cross-linked bovine serum albumin (BSA) forms a suspension of novel fluorescent nanoparticles with an average size of ~40 nm, exhibiting strong green autofluorescence. Autofluorescent nanoparticles were then developed as a novel optical probe for heme detection. Its application for ultrasensitive heme/hemin detection was demonstrated as the fluorescence intensity of the protein nanoparticles were quenched significantly upon the titration of hemin. The ultrasensitive sensing performance is ascribed to Photo-induced Electron Transfer (PET) as well as specific interaction between hemin and the fluorescent protein nanoparticles. The present study provides insights into the design of a cheap, simple and highly sensitive heme/hemin fluorescence biosensor which holds great potential for rapid and sensitive malaria diagnosis.

## *6.1 Introduction*

Heme, a component of the hemoglobin in the blood, is an iron porphyrin involving in a number of enzymatic redox reactions.[1] Its concentration has been used as an indicator of the infection of malaria disease.[2] Current diagnosis methods for malaria include both the direct diagnosis under microscopy to visualize the malaria parasites on the stained blood film and the indirect diagnosis by detecting the elevated heme level in blood due to malaria infection.[2] It has been reported that the interaction between BSA and cationic porphyrin could occur at one or more specific and nonspecific porphyrin-binding sites on BSA (e.g., tryptophan and tyrosine residues), in conjunction with the contribution of tertiary structure of the BSA,[1,3,4] which endows BSA as an ideal sensing material for heme. However, there is lack of reporter to probe such interaction.

In this research, BSA nanoparticles with an average size of ~40 nm were synthesized through GA-crosslinking under dispersion. The as-prepared BSA nanoparticles exhibit unique green autofluorescence over a broad range of excitation. The photophysical properties were investigated through both UV-visible and fluorescence spectra. Dynamic Light Scattering (DLS) and Field Emission Scanning Electron Microscopy (FESEM) were used to investigate their size distribution and surface morphology, respectively. We demonstrate the application of the as-prepared autofluorescent BSA nanoparticles as the probes for heme detection. Since the free form of heme is not commercially available, hemin (heme with a chloride ligand) was employed for the proof-of-concept detection using the autofluorescent BSA nanoparticles.

## *6.2 Experimental*

### 6.2.1 Fabrication of autofluorescent BSA nanoparticles

150 mg/L BSA solution in 10 mM pH 7.4 PBS buffer saline was prepared first as stock solution. The glutaraldehyde/n-butanol dispersion solution was prepared as follows: 50% glutaraldehyde

was diluted ten-fold using 10 mM pH 7.4 PBS buffer and then mixed with n-butanol at a volume ratio of 19 to 1. Then 1 mL 150 mg/mL BSA solution was added dropwise, in ~8 minutes, into 20 mL glutaraldehyde/n-butanol dispersion solution under high dispersing speed using IKA Disperser and thus resulted in the formation of BSA nanoparticles suspension. The as-prepared BSA nanoparticle suspension was then stored in the refrigerator at 4 °C overnight.

### 6.2.2 Characterization

In the UV-visible spectra study, BSA nanoparticle suspension was loaded in a 3 mL quartz cuvette. The UV-vis spectra were collected using a Varian Cary 50 Scan UV-visible Spectrophotometer. 10 mM pH 7.4 PBS buffer was used as control. To study the photophysical properties, the emission fluorescence spectra of BSA nanoparticle suspension were measured using Varian Cary Eclipse Fluorescence Spectrophotometer under different excitation wavelengths. BSA nanoparticle suspension was employed to investigate the size distribution using Dynamic Light Scattering (DLS) at a fixed angle of 90 degree at room temperature. Surface morphology of the prepared nanoparticles was studied using JEOL 6335 Field Emission Scanning Electron Microscopy (FESEM) operating at an accelerating voltage of 10 KV and 12 μA. Pure DI water was used for dialysis to remove the salt in the SEM sample preparation. Prior to imaging, samples were sonicated, loaded, and fixed on a stub using a double-sided carbon tape for drying. Further, the samples were sputter-coated with Au/Pd alloy for 45 s in vacuum at a current intensity of 10 mA for a better contrast.

### 6.2.3 Autofluorescent BSA nanoparticles for heme detection

The fluorescence quenching experiments were performed similar to a procedure reported elsewhere.[4] Briefly, 2 mL BSA nanoparticles suspension was added into 3 mL cuvette, and then 1 mM hemin stock solution (prepared in 2 mM NaOH aqueous solution in order to dissolve

the hemin) was titrated into the BSA nanoparticle suspension with a final concentration ranging from 500 nM to 50 μM. Fluorescence spectra were obtained by Varain Cary Eclipse Fluorescence Spectrophotometer upon excitation at 530 nm with the emission spectra recorded between 540 and 650 nm. Quenching efficiency is calculated as $(I_0\text{-}I)/I_0$, where $I_0$ is the initial fluorescence intensity of BSA nanoparticles suspension at the emission peak of 550 nm in the absence of hemin, and $I$ is the fluorescence intensity of nanoparticles suspension with the titration of hemin. For fluorescence lifetime measurement, the nanoparticle suspension with different concentrations of hemin was excited by a pulsed supercontinuum laser (Solea, PicoQuant) at 530 nm with a repetition rate of 2.5 MHz and a pulse width of ~40 ps. The emission of the samples was collected by an avalanche photodiode (PicoQuant) with a 560 nm bandpass spectral filter. The fluorescence decay was recorded by a time-dependent single photon counting module (Picoharp 300, PicoQuant). For each sample, the measurements were repeated for at least three times.

## *6.3 Results and Discussions*

### 6.3.1 Characterization of autofluorescent nanoparticles

As known, BSA solution exhibits intrinsic absorbance peak at 279 nm (data not shown). Herein, UV-vis spectra were conducted to investigate newly formed fluorescent compounds in the fabrication process. According to the UV-vis spectra results of BSA nanoparticles, showing in the Figure 1, three obvious broad peaks appear in the BSA nanoparticles spectra, comparing with that of pristine BSA solution (data not shown). They are centered at ~475 nm, ~530 nm and ~400 nm respectively. Three classes of fluorescent compounds were presumably formed corresponding to the result of UV-vis spectra.

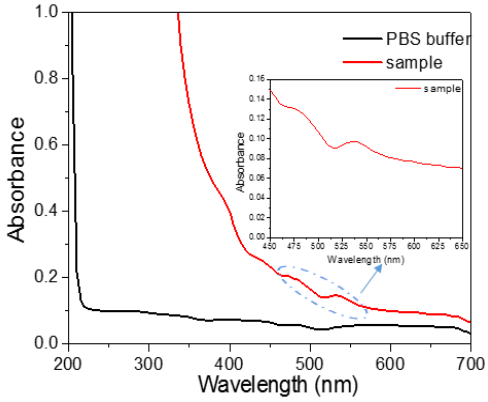


Figure. 1 UV-visible spectra of the as-prepared BSA nanoparticle suspension and the PBS buffer (control), respectively. Inset shows the enlarged UV-vis spectrum of BSA nanoparticle suspension in the range of 450 to 650 nm.

To further study the optical properties of as-synthesized BSA nanoparticles dispersion, fluorescence emission scans were performed. Based on the result of UV-vis spectra, the sample was excited from 400 nm to 550 nm with 10 nm intervals as the emission spectra were collected in the range of 10 nm longer than the excitation wavelength to 700 nm. In the Figure 2, it exhibits strong green fluorescence emission peak with the excitation wavelengths between 400-540 nm, existing slight peak shift from 500 nm to 560 nm.

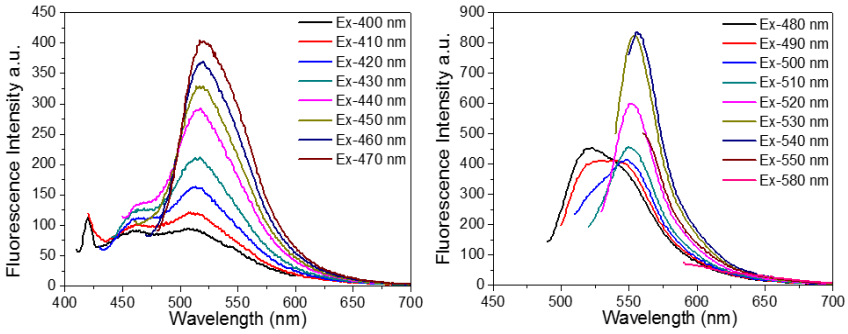


Figure 2 Fluorescence emission spectra scans of the autofluorecent BSA nanoparticles.

### 6.3.2 Autofluorescent BSA nanoparticles for heme detection

To investigate the applicability of the as-prepared autofluorescent BSA nanoparticles in sensing trace amounts of hemin, fluorescence quenching titrations were conducted with the incremental addition of hemin into the autofluorescent BSA nanoparticle suspension. The corresponding

result is presented in Figure 3a, indicating that the emission (λ=530 nm) of the BSA nanoparticles excited at λ=530 nm gradually decreased with the increase of hemin concentration (from 500 nM to 50 μM, relevant to the biological heme level) and displayed a concentration-dependent behavior. The fluorescence intensity is quenched nearly 60% when the hemin level reaches 50 μM in the system. The corresponding calibration curve is presented in Figure 3b. As a comparison, the titration of the control solution (same as hemin stock solution except that there is no hemin) into autofluorescent BSA nanoparticle suspension does not result in fluorescence quenching (data not shown). This observation, in conjunction with Figure 3a, indicates that the quenching of BSA nanoparticles is attributed to the presence of hemin.

To characterize the quenching behavior of the autofluorescent nanoparticles, normalized fluorescence intensity ($I_0/I$) and quenching constant (*Ksv*) are employed in the Stern-Volmer equation [5]

$$I_0/I = K_{SV}[A] + 1 \qquad (1)$$

where $I_0$ is the initial fluorescence intensity without titration of the quencher (hemin), $I$ is the fluorescence intensity with the titration of the quencher (hemin), [$A$] is the molar concentration of the quencher (hemin), and *Ksv* is the quenching constant ($M^{-1}$). Figure 3c presents the Stern-Volmer plot of $I_0/I$ for the autofluorescence of BSA nanoparticles at λ=550 nm versus the hemin concentrations in the system. The Stern-Volmer plot shows good linearity ($R^2$=0.991) through the entire hemin concentration range and the calculated quenching constant is *Ksv* = $2.66\times10^4$ $M^{-1}$ with a detection limit as low as 500 nM. The large *Ksv* value and good detection limit demonstrate that the autofluorescent BSA nanoparticles is highly sensitive to hemin, which might be attributed to the reduced LUMO energy of hemin once complexed with BSA.[6]

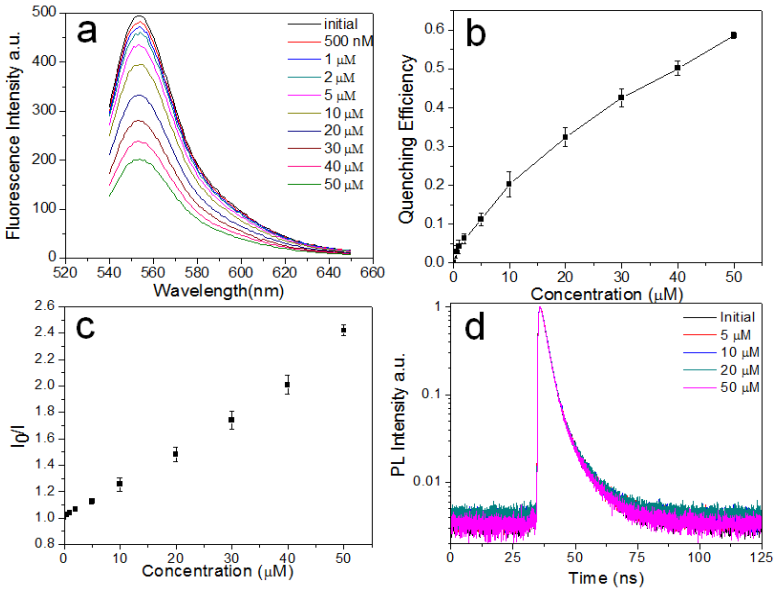


Figure 3 a) Concentration-dependent quenching titration of the autofluorescent BSA nanoparticles suspension upon the injection of different hemin (μM) concentrations; b) A calibration plot of the quenching efficiency vs. hemin concentration; c) The Stern-Volmer plot of autofluorescent BSA nanoparticles (at the emission peak of 550 nm) upon hemin titration; and d) The normalized time-dependent decay curves for autofluorescent BSA nanoparticles with the titration of hemin at a final concentration of 0, 5, 10, 20, and 50 μM, respectively.

To explore the quenching mechanism of autofluorescent BSA nanoparticles upon the titration of hemin, fluorescence lifetime study is carried out. Figure 3d shows the normalized time-dependent fluorescence intensity decay curves of autofluorescent BSA nanoparticles with different hemin concentrations. The fluorescence lifetime is curve-fitted by an exponential decay function, expressed as

$$I(t) = I(0)\exp(-t/\tau) + C \qquad (2)$$

where *I(0)* is the initial fluorescence intensity, $I(t)$ is the fluorescence intensity at time $t$, and $\tau$ is the characteristic fluorescence lifetime.

The decay curves in Figure 3d overlap with each other, indicating that the hemin concentration in the tested range has no influence on the fluorescence decay of autofluorescent BSA nanoparticles, even though the fluorescent intensity is greatly decreased by the titration of hemin (Figure 3a).

This indicates that a static quenching mechanism is responsible for hemin detection where hemin interact with the autofluorescent BSA nanoparticles in the ground state and form a non-fluorescent complex. [12] From Stern-Volmer equation:

$$I_0/I = k_q\tau_0[A] + 1 = K_{SV}[A] + 1 \qquad (3)$$

where $k_q$ is bimolecular quenching constant and $\tau_0$ is fluorescence lifetime, one could find that $k_q$ = $8\times10^{12}$ $M^{-1}s^{-1}$, which is larger than the value of $10^{10}$ $M^{-1}s^{-1}$ for conventional diffusion quenching. This further confirms the static quenching mechanism of the autofluorescent BSA nanoparticles upon the titration of hemin.

This study provides insights into the design of a cheap, simple and highly sensitive heme/hemin fluorescence biosensor which holds great potential for rapid and sensitive malaria diagnosis.

**Reference**


1. Xiao, C.-Q.; Jiang, F.-L.; Zhou, B.; Li, R.; Liu, Y., Interaction between a cationic porphyrin and bovine serum albumin studied by surface plasmon resonance, fluorescence spectroscopy and cyclic voltammetry. *Photochemical & Photobiological Sciences* 2011**, 10 (7)**, 1110-1117.
2. Briand, V. A.; Thilakarathne, V.; Kasi, R. M.; Kumar, C. V., Novel surface plasmon resonance sensor for the detection of heme at biological levels via highly selective recognition by apo-hemoglobin. *Talanta* **2012,** *99*, 113-118.
3. Chatterjee, S.; Srivastava, T., Spectral investigations of the interaction of some porphyrins with bovine serum albumin. *Journal of Porphyrins and Phthalocyanines* 2000, **4 (02)**, 147-157.
4. Sun, X.; Ma, X.; Kumar, C. V.; Lei, Y., Protein-based sensitive, selective and rapid fluorescence detection of picric acid in aqueous media. *Analytical Methods* 2014, **6 (21)**, 8464-8468.
5. Gogoi, B.; Sarma, N. S., Enhanced fluorescence quenching of hemin detected by a novel polymer of curcumin. RSC Advances 2013, 3 (21), 7747-7750.
6. Sun, X.; Liu, Y.; Shaw, G.; Carrier, A.; Dey, S.; Zhao, J.; Lei, Y., Fundamental study of electrospun pyrene–polyethersulfone nanofibers using mixed solvents for sensitive and selective explosives detection in aqueous solution. ACS applied materials & interfaces 2015, **7 (24)**, 13189-13197.
7. Sun, X.; Wang, Y.; Lei, Y., Fluorescence based explosive detection: from mechanisms to sensory materials. Chemical Society Reviews 2015, **44 (22)**, 8019-806.

# Chapter 7
# Summary and Prospects

## *7.1 Summary*

Biocompatible and biodegradable natural polymer based materials with fluorescence properties, standing at the cutting edge, are broadly employed for various biomedical applications, including bio-imaging, tissue engineering, drug delivery and biosensing, etc.. Chapter 1 briefly introduces the synthesis methods of various fluorescent natural polymer based matrixes, mainly focusing on polysaccharides and proteins based or containing materials. In general, preparation of these fluorescent materials is either via physical or chemical interaction, or both. To gain optical properties for bio-imaging applications, optical contrasts are physically or covalently incorporated in the polymer building blocks, or autofluorescence is induced into the materials during the cross-linking process. The bio-imaging related applications were reviewed in separated two sections: *in vivo* and cell imaging. This dissertation aims at developing novel autofluorescent protein-based materials for bio-imaging assisted degradation kinetics study.

In this dissertation, protein-based autofluorescent hydrogels in three sizes (bulk, nanoparticles and microspheres) were fabricated and well characterized by a series of advanced techniques. They were then applied for bio-imaging applications. Moreover, systematic *in vivo* and *in vitro* degradation kinetics of the synthesized materials were investigated by the integration of bio-imaging experiments and mathematical modeling, resulting in complementary kinetics model with parameters representing physical conditions. In addition, as-synthesized autofluorescent nanoparticles were also applied for fluorescence-based heme detection, demonstrating the widely potential biomedical applications of the synthesized materials. Overall, the work provides valuable insights into the rational design and synthesis of autofluorescent polymeric materials, which could be applied in a broad range of biomedical applications.

## *7.2 Prospects*

Although fluorescent polymeric materials have demonstrated their applicability in bio-imaging related biomedical studies, there are several challenges which need to be addressed in order to further expand their applications. For fluorescence-based *in vivo* imaging, the penetration depth of light and the achievable resolution are the major factors to limit the broader applications of fluorescent polymeric materials, because of the strong absorption of the visible light by tissue compounds and by biological chromophores (e.g., hemoglobin), the tissue damage by the light in UV range and the strong autofluorescence of tissues. Thus, fluorescence-based *in vivo* imaging is mainly applicable for the dyes in NIR range, not only attributing to its good penetration, but also low damage to the tissues. Furthermore, bio-imaging can be realized either qualitatively or quantitatively. Qualitative *in vivo* bio-imaging or imaging related applications, such as tracking drug delivery efficiency, tumor targeting, and photo-induced therapy etc., have been reported through intravenous, intraperitoneal or intramuscular injection of various fluorescent polymeric materials, because there is no need to extract accurate optical intensities from the acquired images. However, quantitative bio-imaging applications include imaging-assisted real-time biodegradation study, and real-time release and resorption monitoring of molecules of interests, which require the accuracy of the obtained fluorescence intensities along the change of time. Furthermore, near infrared signals can be captured, but the fluorescence intensity extracted from the imaging is not equivalent to the real value due to the light scatterings and absorptions, especially for the cases with deep injection of the fluorescent materials. That is the reason why subcutaneous injection is applied in most of aforementioned bio-imaging studies. Even though bio-imaging of subcutaneously injected fluorescent polymeric materials can avoid inaccuracy with a good success, the fate of the implants in deeper tissues is still unclear and difficult to be

illustrated based on their counterpart's subcutaneous behavior due to the different structure and composition of tissues in different layers. In addition, the obtained *in vivo* fluorescence imaging is typically in two dimensional configuration, yet the real scenario of *in vivo* imaging is in three dimensions. Thus, real *in vivo* performance cannot be accurately tracked and predicted unless three-dimensional fluorescent images can be reordered, which not only require more advanced instruments, but also sacrifice the accuracy of the recorded images due to the complexity of tissues. Therefore, bimodal imaging technique, which relies on two different signals, is promising. In this way, not only optical contrast is embedded, but also imaging contrast for other imaging techniques (e.g., MRI or CT). Thus it allows for the integration and complementation of the obtained results.

Besides fluorescence imaging techniques, materials used in bio-imaging related studies are another factor which should be considered in the design of fluorescent polymeric materials. In most of studies in literature, optical contrasts (e.g., fluorophores) are integrated into the polymeric matrixes via either covalent or physical linking, thus endowing the fluorescence. The use of those optical contrasts may result in potential issues in bio-medical applications, including photo-bleaching, poor-biocompatibility, and leakage, which could not only reduce the optical signal intensity, but also induce inaccuracy in the quantitative analysis of the data. Recently, several groups including our group reported that natural polymer based building blocks can induce unique and superior stable autofluorescence during the cross-linking process, without the need of additional fluorophores. Such autofluorescent polymeric materials possess unparalleled advantages compared with the ones with embedded fluorescent dyes. Their application in bio-imaging related studies shows early success. Yet, the formation mechanism of such autofluorescence is still not fully understood due to the structural complexity of the natural

polymers. More efforts should be spent on illustrating the underlying principles in the formation of strong and stable autofluorescence, which may open a new avenue in the design of fluorescent polymeric materials. I believe that with the development of simulation methods and the establishment of more and more accurate materials models to reveal the structure-property-function relationship, a computation method to simulate the material properties including such autofluorecence functionality of various materials or composites after cross-linking process is expected to play a critical role in the screening/selection of specific materials in the future design of autofluorescent polymeric materials.

# Appendix

## Journal Publications

1. **X.Y. Ma**, Y. Lei, Facile synthesized carbon nanoparticles for sensitive and selective ferric ion detection. 2017, Under preparation
2. **X.Y. Ma**, J. Q. Li, T-H. Fan, Y. Lei Experimental and theoretical study of enzymatic degradation kinetics using BSA auto-fluorescent microspheres. Under review
3. **X.Y. Ma**, X. C. Sun, J. Chen, Y. Lei, Natural or natural-synthetic hybrid polymer based fluorescent polymeric materials for bio-imaging related applications. Applied Biochemistry and Biotechnology. 2017, Accepted. (Invited Article)
4. **X.Y. Ma**, X.C. Sun, D. Hargrove, J. Chen, D. H. Song, Q. C. Dong, X. L. Lu, T-H. Fan, Y. Lei, A biocompatible and biodegradable protein hydrogel with green and red autofluorescence: preparation, characterization and in vivo biodegradation tracking and modeling, Scientific Reports (Nature) 2016, 6.
5. **X.Y. Ma**, T.R. Wang, D. H. Song, D. Hargrove, Q. C. Dong, Z. Luo, J. Chen X. L. Lu, Y. C. Luo, T-H Fan, Y. Lei, Protein microspheres with unique green and red autofluorescence for noninvasively tracking and modeling their in vivo biodegradation. ACS Biomaterials Science & Engineering 2016, 2.
6. **X.Y. Ma**, D. Hargrove, Q. C. Dong, D. H. Song, J. Chen, S. Y. Wang, X. L. Lu, Y. K. Cho, T-H. Fan, Y. Lei, Novel green and red autofluorescent protein nanoparticles for cell imaging and in vivo biodegradation imaging and modeling, RSC advance 2016, 6.
7. K. Connelly, Y. P. Wu, **X. Y. Ma**, Y. Lei, Transmittance and reflectance studies of thermotropic material for a novel building integrated concentrating photovoltaic (BICPV) 'smart window' system. 2017, Under review.
8. F. Cao, Q. C. Dong, C. L. Li, J. Chen, **X. Y. Ma**, Y. K. Huang, D. H. Song, C. H. Ji, Y. Lei, An ultrasensitive and selective electrochemical sensor for detection pain reliever/Fever reducer drug acetaminophen based on electrospun CeBiOx nanofibers modified screen-printed electrode. 2017, Under review.
9. J. Chen, Q.C. Dong, Y. K. Huang, **X.Y. Ma**, Y. Lei, Rapid self-healing protein hydrogels with autofluorescent Property. 2017, Under review.
10. J. Chen, Y. K. Huang, **X. Y. Ma**, Y. Lei Functional self-healing materials and their potential applications in biomedical engineering. Advanced Composite & Hybrid Materials. 2017, Accepted. (Invited article)
11. S. C. Zhang, X.C. Sun, J. Chen, **X.Y. Ma**, Y.P. Wu, Y. Lei Fluorescent carbon nanoparticles for sensitive and selective detection of palladium. Science Advanced Today 2017 Accepted. (Invited Article)
12. J. Bao, C. J. Hou, D.Q. huo, Q. C. Dong, **X.Y. Ma**, X. C. Sun, M. Yang, K. H. A. E. Galil, W. Chen, Y. Lei Sensitive and selective electrochemical biosensor based on ELP-OPH/BSA/TiO2NFs/AuNPs for direct determination of p-nitrophenyl substituted organophosphate pesticides. Journal of Electrochemical Society. 2017, 164
13. X. C. Sun, J. K. He, Y. T. Meng, L. C. Zhang, S. C. Zhang, **X.Y. Ma**, S. Dey, J. Zhao, Y. Lei, Microwave-assisted ultrafast and facile synthesis of fluorescent carbon nanoparticles from single precursor: preparation, characterization and its application for highly selective detection of explosive picric acid. Journal of Materials Chemistry A. 2016,4.
14. X.C. Sun, **X.Y. Ma**, C. V. Kumar, Y. Lei Protein-based sensitive, selective and rapid fluorescence detection of picric acid in aqueous media. Analytical Methods. 2014, 6.

15. S. Mopidevi, J. Chen, **X.Y. Ma**, K.H.A.E.G Galil, Y. Lei, PEG-fluorescein-GOx hydrogel for glucose biosensing. ScienceJet 2015. 4.
16. J. Bao, C.J. Hou, Q.C. Dong, **X.Y. Ma**, J. Chen, D. Q. Huo, M. yang, K. J. A. E. Galil, W. Chen, Y. Lei. ELP-OPH/BSA/TiO2 nanofibers/c-MWCNTs based biosensor for sensitive and selective determination of p-nitrophenyl substituted organophosphate pesticides in aqueous system. Biosensors and Bioelectronics, 2016, 85.
17. T. Wang, **X.Y. Ma**, Y. Lei, Y.C. Luo. Solid lipid nanoparticles coated with cross-linked polymeric double layer for oral delivery of curcumin. Accepted Colloids and Surfaces B: Biointerfaces, 2016, 148.
18. J. Chen, **X.Y. Ma**, Q. C. Dong, D. H. Song, D. Hargrove, S. R. Vora, A. W. K. Ma, X. L. Lu, Y. Lei. Self-healing of thermal-induced, biocompatible and biodegradable protein hydrogel. RSC advance, 2016, 61
19. J Chen, Q. C. Dong, **X.Y. Ma**, T-H Fan, Y. Lei, Self-healing of Ca2+ induced nanocomposite protein hydrogel. Scientific Reports (Nature), 2016, 6.

## Conference Presentation

1. **Xiaoyu Ma**, Y. Lei, Autofluorescent protein nanoparticles based biosensor for ultrasensitive heme/hemin detection, oral presentation, The 4th International Conference and Exhibition on Biosensors & Bioelectronics. 2015
2. **Xiaoyu Ma**, Y Lei, A Biocompatible and Biodegradable Protein Hydrogel with Green and Red Autofluorescence: Preparation, Characterization and *In Vivo* Biodegradation Tracking and Modeling, 42nd 2016 Northeast Bioengineering Conference. 2016
3. **Xiaoyu Ma,** J. Chen, Yu Lei, In vivo degradation tracking and modeling of three sizes configuration of autofluorescent protein hydrogels, ACS annual conference. 2016
4. J. Chen, **Xiaoyu Ma,** Yu Lei, Self-healing of thermal-induced, biocompatible and biodegradable protein hydrogel. 252nd ACS annual conference, 2016
5. **Xiaoyu Ma,** Yu Lei, Comparative Study of in vivo degradation tracking and modeling using autofluorescent protein microspheres and nanoparticles suspension. BMES annual conference, 2016
6. J. Chen, **Xiaoyu Ma,** Yu Lei, Self-healing of thermal-induced protein hydrogel. BMES annual conference, 2016
7. **Xiaoyu Ma,** Jun Chen, Yu Lei, Swayandipta Dey, Jing Zhao, Autofluorescent Nanoparticles for the Detection of Malaria-Infection Indicator. IEEE Sensors. 2016
8. S. Zhang, X, Sun, **Xiaoyu Ma**, Yu Lei, Fluorescent carbon nanoparticles for sensitive and selective detection of palladium. IEEE Sensors. 2016